PSFC/RR-12-2 DOE/ET-54512-377

Rotation Generation and Transport in Tokamak Plasmas

Podpaly, Y.A.

April, 2012

Plasma Science and Fusion Center
Massachusetts Institute of Technology
Cambridge MA 02139 USA

This work was supported by the U.S. Department of Energy, Grant No. DE-FC02-99ER54512 and by the Fusion Energy Sciences Program, administered by Oak Ridge Institute for Science and Education under a contract between the U.S. Department of Energy and the Oak Ridge Associated Universities.

Rotation Generation and Transport in Tokamak Plasmas

by

Yuri Anatoly Podpaly
S.B. Physics, S.B. Nuclear Science and Engineering
Massachusetts Institute of Technology(2007)

Submitted to the Department of Nuclear Science and Engineering
in partial fulfillment of the requirements for the degree of
Doctor of Philosophy in Nuclear Science and Engineering
at the
MASSACHUSETTS INSTITUTE OF TECHNOLOGY
June 2012

Author .....
Department of Nuclear Science and Engineering
April 30, 2012

Certified by .....
Dr. John E. Rice
Principal Research Scientist
Thesis Supervisor

Certified by .....
Prof. Jeffrey P. Freidberg
Professor of Nuclear Science and Engineering
Thesis Reader

Certified by .....
Prof. Ronald R. Parker
Professor of Nuclear Science and Engineering
Thesis Reader

Accepted by .....
Prof. Mujid S. Kazimi
TEPCO Professor of Nuclear Engineering
Chair, Department Committee on Graduate Students

Rotation Generation and Transport in Tokamak Plasmas

by

Yuri Anatoly Podpaly

Submitted to the Department of Nuclear Science and Engineering
on April 30, 2012, in partial fulfillment of the
requirements for the degree of
Doctor of Philosophy in Nuclear Science and Engineering

Abstract

Plasma toroidal rotation is a factor important for plasma stability and transport, but it is still a fairly poorly understood area of physics. This thesis focuses on three aspects of rotation: momentum transport, Ohmic rotation reversals, and LHCD induced rotation. Momentum transport is approached in a semi-empirical method through the development of the "Toy Model." The "Toy Model" assumes that the toroidal momentum is transported via diffusive and convective profiles, and, using assumptions about the diffusive and convective terms, it can generate the profiles of the residual stress or source as a function of space and time. Several resultant source profile calculations are shown for SSEP sweeps, rotation reversals, H-modes, and I-modes. Generally, it is observed that the convective profiles do not greatly improve the fits to the data, and that source profiles have peaks around the steep core rotation gradient region of the plasma. Rotation reversals, spontaneous reversals of the rotation direction during the Ohmic phase, are also described in this work. It is seen that they are related to the Linear Ohmic Confinement (LOC) to Saturated Ohmic Confinement (SOC) regime changeover. This relation is supported through linear gyrokinetic simulations that show that the co- to counter- reversal coincides with a change from marginally electron to ion diamagnetic direction most unstable modes which is believed to play a role in the LOC to SOC explanation as well. Lower Hybrid Current Drive (LHCD) induced rotation is also described, including the first experimental observations of bi-directional rotation on a single tokamak. These observations help to explain differences in rotation seen among the various devices running lower hybrid. The LHCD rotation reverses direction as a function of plasma current, and this occurs in a similar parameter space as the Ohmic rotation reversal; it also has turbulence changes that are reminiscent of the Ohmic reversal as well. This suggests that LHCD is, in fact, causing the plasma to transition from the ITG dominated regime to the TEM dominated regime, which explains the rotation differences. These experiments and models provide new tools to understand rotation transport and generation in tokamaks.

Thesis Supervisor: Dr. John E. Rice

Title: Principal Research Scientist

Thesis Supervisor: Prof. Jeffrey P. Freidberg
Title: Professor of Nuclear Science and Engineering

Thesis Supervisor: Prof. Ronald R. Parker
Title: Professor of Nuclear Science and Engineering

Acknowledgments

There is an enormous number of people who have provided me with invaluable assistance during the previous years at MIT, and I would like to mention a few of them below.

First and foremost, I would like to thank my advisor, John Rice. His wisdom, quirks, and sage advice have done more to move my research both as an undergraduate and graduate student than I believed possible. His connections and calm under any circumstances have helped to offset my own diffidence and allow work to progress and refocus at difficult times. None of the presented work would have been possible without his guidance, and, for that and much more, I am deeply grateful.

I would also like to thank my thesis committee: readers Prof. Jeff Freidberg and Prof. Ron Parker, and committee chair Prof. Dennis Whyte. Professor Freidberg both took the time to read through this work and also acted as my academic adviser over the last several years. Professor Parker not only read this work but was also deeply involved in the lower hybrid current drive research which forms a large section of this thesis. He was also instrumental in securing the run time on Alcator C-Mod needed to gather my thesis data. Prof. Dennis Whyte has been a superb teacher, and I am particularly thankful for his leadership of the Vulcan design project.

I would like to highlight the spectroscopy group at the Alcator C-Mod project and the various collaborators involved in it. Dr. Luis Felipe Delgado-Aparacio joined and quickly made himself an indispensable part of this team. Dr. Matt Reinke, without whom this work would be impossible, has contributed countless coding hours and scientific advice since the inception of the HiReX Sr project. Chi Gao has helped shoulder the maintenance of the HiReX Sr spectrometer and has taken over many of the spectroscopy projects as well, and I would like to thank him for that assistance. Former spectroscopy member and now fellow graduate student John Walk has been a great help both in spectroscopy and now with the Thomson group.

There is an enormous array of scientists who have helped with my work. Dr. Manfred Bitter and Dr. Ken Hill deserve particular mention for their setting up

of the HiReX Sr project and continued support and advice with regard to not only science but career decisions. Dr. David Mikkelsen was instrumental in setting up the GYRO and TRANSP codes which have been used in my research extensively. Dr. Darin Ernst has provided numerous hours of gyrokinetic simulation support and interpretation, developed the fiTS code, developed the GS2 support codes, and co-maintains the LOKI supercomputing cluster. I would also like to thank Professor Patrick Diamond and Professor Nathaniel Fisch for their advice on various theoretical intricacies with the physics of LHCD. Dr. Earl Marmar has supported my diagnostics work and has helped during difficult times, for which I am thankful.

I would like to point out, as well, several graduate students who have been indispensable in my graduate career. My fellow class collaborator, Magnetic Fusion Energy Formulary co-author, officemate, and qualifying exam study partner, Zachary Hartwig, has been one of the strongest forces driving me to improve my work and explore beyond the boundaries of my own research, work, and beliefs both inside and outside of the lab. Christian Haakonsen has been a constant grounding force of reasonableness and advice, and I would like to thank him for that. Former officemate Dr. Orso Meneghini was a great source of advice with regards to classes and lower hybrid modeling. Of course, my former roommate, Dr. Aaron Bader, has provided a great deal of advice, both inside and outside of fusion research. Dr. Nathan Howard, also, deserves special thanks for assisting me with the GYRO simulations in this work and providing many of the codes used in this work.

Special recognition is also due to my co-workers at Lawrence Livermore National Laboratory. Dr. Peter Beiersdorfer trained me on the Electron Beam Ion Trap, directed my work there, and taught me a great deal about scientific work in general. His influence has changed the course of my career in many ways, and I am deeply grateful to him. Dr. Greg Brown, Dr. Joel Clementson, Dr. Dan Thorne, Donna Vercelli, and Miriam Fraenkel were great co-workers and sources of advice and help. Thank you for making my stay at LLNL so hospitable.

It would be too space consuming to thank everyone who has helped me in detail, but I would like to list a few of the many people who have been helpful to my work.

There were Prof. Bruno Coppi, Prof. Felix Parra-Diaz, Prof. Ian Hutchinson, Prof. Miklos Porkolab, and Prof. Anne White ; scientists Dr. Igor Bespamyatnov, Dr. Paul Bonoli, Dr. Brock Bose, Dr. Istvan Cziegler, Dr. Peter Catto, Dr. Catherine Fiore, Dr. Robert Granetz, Dr. Martin Greenwald, Dr. Amanda Hubbard, Dr. Jerry Hughes, Dr. Alexander Ince-Cushman, Dr. Jim Irby, Dr. Jinseok Ko, Dr. Brian LaBombard, Dr. Yijun Lin, Dr. Bruce Lipschultz, Dr. Ken Marr, Dr. Bill Rowan, Dr. Jason Sears, Dr. Steve Scott, Dr. Syuin'ichi Shiraiwa, Dr. Tuomas Tala, Dr. Jim Terry, Dr. Greg Wallace, Dr. Steve Wolfe, and Dr. Steve Wukitch. The technicians and engineers who made the device function and put up with my endless questions Bill Beck, David Bellofato, Lee Berkowitz, Gary Dekow, Ed Fitzgerald, Tom Fredian, David Gwinn, Mark Iverson, Atma Kanojia, Felix Kriesel, Paul Lienard, Mark London, Andy Pfiefer, Ron Rosati, Mike Rowell, Brandon Savage, Henry Savelli, Josh Stillerman, David Terry, and Tom Toland. I would also like to thank the personnel who have helped me navigate the MIT PSFC and MIT in general: Heather Barry, Alisa Cabral, Valerie Censabella, Jessica Coco, Clare Egan, Lee Keating, Marcia Mora, Elizabeth Parmelee, Paul Rivenberg, Jason Thomas, and Leslie West. And, of course, I am indebted to my fellow graduate students Harold Barnard, Seung Gyou Baek, Dan Brunner, Mark Chilenski, Michael Churchill, Joel Cohen, Evan Davis, Arturo Dominguez, Paul Ennever, Ian Faust, Mike Garrett, Theodore Golfinopoulos, Cornwall Lau, Ken Liao, Jungpyo Lee, Yunxing Ma, Mario Manuel, Bob Mumgaard, Roman Ochoukov, Geoff Olynyk, Josh Payne, Rezy Pradipta, Nareg Sinenian, Naoto Tsujii, and Kevin Woller.

I would also like to express my deepest gratitude to J.M., M.G., P.S., S.B., and, of course, L.M. for their support over the last several years. Last, but certainly not least, I would like to thank my family for their consistent assistance, advice, and much more. Thank you R.P., A.P., J.P., T.P., E.S, A.B., E.S., M.S., and I.S.

This work was supported by the Fusion Energy Sciences Program, administered by Oak Ridge Institute for Science and Education under a contract between the U.S. Department of Energy and the Oak Ridge Associated Universities and the Department of Energy under Contract No. DE-FC02-99ER54512. Computer simulations using GS2

and GYRO were carried out on the MIT PSFC parallel AMD Opteron/Infiniband cluster Loki. Many of the calculations were performed using TRANSP on the PPPL Unix cluster, and the author acknowledges assistance in performing these from the PPPL TRANSP development group.

Contents

THIS PAGE INTENTIONALLY LEFT BLANK

List of Figures

List of Tables

THIS PAGE INTENTIONALLY LEFT BLANK

Chapter 1

Introduction

1.1 Preface

One of the most pressing concerns in international politics over the past few decades is providing sufficient energy for the world's growing population. The present power generation facilities utilize coal, oil, fission, and a variety of more rare sources such as hydroelectric, wind, and solar. Coal, oil, and natural gas power plants have serious issues with pollution, and their fuels are often located in regions with major social, ecological, and/or political difficulties leading to political problems with their procurement. The renewable energy sources have not yet proved themselves capable of taking over the baseline power requirements, and there are serious concerns about their expense and applicability. Fission is one of the most controversial power sources due to its connection with disasters at Three Mile Island, Chernobyl, and, more recently, Fukushima Daiichi, and due to the generation of long lived radioactive waste from its power cycle. Despite being relatively clean and efficient, fission has developed a negative reputation in the United States and several other countries, severely limiting its applicability.

Overall, the state of power generation causes serious concerns. The world's energy consumption continues to rise, and the ability to generate power from standard energy sources is not matching projected future demand. This situation is not sustainable without the optimization of current energy sources or the development of new sources.

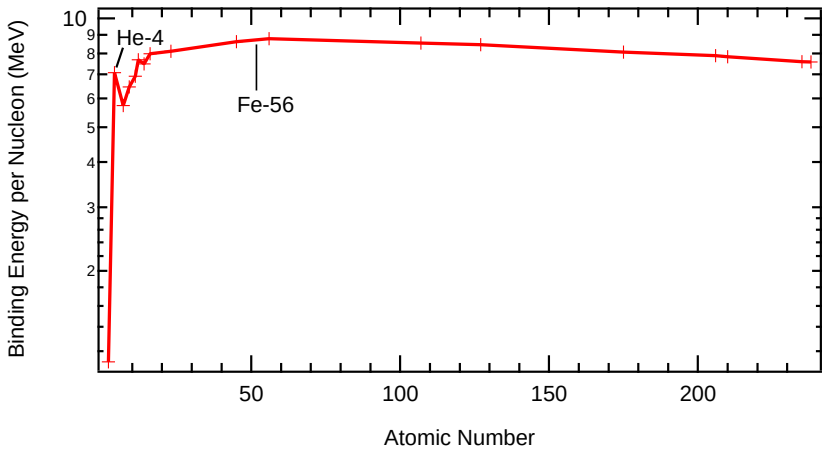

Figure 1-1: Nuclear binding energy curve. Elements on the higher mass side of the curve are subject to fission, while the lower mass side is subject to fusion.

Some of the optimization that has been under consideration is the development of clean coal, more efficient solar cells, large scale wind farms, and burner-breeder nuclear fission power plants. Among the potential new power supplies, the most promising mechanism is nuclear fusion.

Fusion aims to generate power from combining small nuclei into larger ones releasing energy in the process. In contrast, fission generates energy by splitting heavy isotopes into lighter ones. Both sources are feasible because they operate on different sides of the nuclear binding energy curve shown in Figure 1-1. Heavy elements can undergo fission releasing energy to create more tightly bound light elements, and light elements can undergo fusion to create more tightly bound heavier elements. The most tightly bound nucleus is Iron-56, so as long as the elements are above or below this pivot point they can undergo nuclear reactions to release energy.

The fusion cross section is much smaller than the Coulomb scattering cross section at all energies. In order to create a fusion reactor, therefore, a high-energy thermalized population of ions is required. The temperatures of these thermalized fusion relevant ion populations sets the reactants to be a $\sim 10^8$ K plasma. No physical material is capable of confining an object of that temperature without cooling the reaction or melting the material, so magnetic and/or electric fields are required to confine the plasma. This research path led to the development of the tokamak [7], a

toroidally shaped device which uses strong magnetic fields to confine highly ionized plasma. Most of the devices currently proposed for fusion reactors are tokamaks, so the most applicable fusion work is on them and similar devices (such as stellarators, spheromaks, or reversed field pinches).

Tokamaks have a variety of outstanding questions regarding both their technical and physical properties. These include basic plasma physics, materials issues, generating energy from the fusion reaction, and proliferation concerns. The work described in this thesis is primarily about the plasma physics of a toroidal fusion reactor. One of the issues that has been receiving a great deal of attention recently in plasma physics is the generation and control of the rotation profile. Rotation is important for fusion reactors because it has been seen to suppress resistive wall modes and rotation shear can decrease turbulence improving plasma performance [8, 9]. These effects mean that both understanding and controlling how rotation is driven and transported in the plasma is important for fusion devices and can lead to significant improvements in plasma operation. Furthermore, plasma rotation is still not a well understood topic from the theoretical point of view, and new observations and tests of theoretical predictions can be important for the improvement of that field. The following work has been performed at the Alcator C-Mod device (see Appendix A for details) at the MIT Plasma Science and Fusion Center.

1.2 Outline

The outline of the rest of this thesis will be as follows. First, a brief introduction to rotation theory will be presented in Chapter 2. Then, in Chapter 3, the diagnostic set-up used will be discussed. In Chapter 4, research about rotation reversals and their underlying physics will be shown. Chapter 5 will be about Lower Hybrid Current Drive rotation observations and some proposed explanations for them. Chapter 6 discusses rotation profile modeling and its implications to various rotation theories. Chapter 7 includes some conclusions and future work to be performed on the presented issues.

1.3 Units

The units used in this thesis have been chosen to match the most commonly used unit system in the topic from which the values were selected. If at all possible, the System Internationale (S.I. or MKS) will be used as a standard. A notable exception to this rule is the historical standard of using electron-Volts (eV) for temperature in place of degrees Kelvin. Furthermore, many of the theories described in the background section of this work are developed in the C.G.S unit system and for consistency are not changed. A comprehensive set of unit definitions and equations usable in this thesis and elsewhere is in [10].

Chapter 2

Background

Plasma rotation research has generally had two approaches in the past. The first approach was studying the plasma with a known momentum source through the use of external neutral beams, notably at DIII-D [11, 12]. The other approach has been to study the issue from the intrinsic rotation standpoint: understanding the plasma rotation with no external sources. From a theoretical standpoint, plasma rotation research in the past has generally focused on neoclassical predictions for tokamak plasmas. It was found that these predictions were not accurate from experimental measurements, and these findings motivated more detailed including turbulence, but they also led to development of less rigorous models that would allow generating insights from rotation results without as detailed calculations. This section describes various detailed rotation theories and contains a description of the simplified model of momentum transport and its modifications in the present work. This section is intended to provide background and to motivate the research performed in this thesis.

2.1 Importance of Rotation in Plasmas

Rotation research has been of major interest due to its importance for L-H mode transitions, plasma stability, and suppression of turbulence in the plasma. Furthermore, rotation transport is still an ongoing question theoretically, so providing more comprehensive data of how the angular momentum in a tokamak is generated and

transported is an important task.

One of the most important aspects of plasma rotation is its effect on the transition of a plasma into H-mode. The ITER tokamak, as well as most reactor designs currently proposed, is expected to run H-mode plasmas [13, 14, 15]. During an H-mode transition, there are marked toroidal spin-ups of the plasma with observed changes in the poloidal rotation and radial electric field [16, 17]. It has been seen, furthermore, that the power threshold for transitioning from L- to H-modes can depend on the toroidal rotation in the target plasma [18, 19], which further emphasizes the importance of understanding the rotation in the plasma.

It has also been seen that rotation shear has a strong effect on the turbulence in the plasma [20]. This turbulence suppression is what is believed to be the driver of the Internal Transport Barrier (ITB) and Edge Transport Barrier (ETB), localized areas of reduced transport [21]. It has been observed that electric field shear is correlated with the ITB formation and may explain the transport in the barrier [22]. Therefore, understanding rotation is beneficial from the perspective of understanding energy transport and transport barriers in a tokamak.

The third effect of toroidal rotation is the stabilization of the resistive wall mode [23, 24]. It has been calculated that at an Alfvén Mach number of 0.02 (or even less) the ITER resistive wall mode will be stabilized, and this will avoid the need for external stabilization coils. Removing these coils is cost effective, therefore predicting the driven rotation velocities is extremely important.

Finally, the proper implementation of rotation transport in a gyrokinetic plasma simulation is still undergoing improvements. The simulations are still not fully implemented, and there is work progressing to account properly for the conservation of angular momentum [25]. The GS2 code is being improved with a new collision operator, which should properly conserve momentum in the gyrokinetic equations. Improving the ability of the simulations to explain the rotation should, through the coupled nature of gyrokinetic equations, improve the general capabilities of the codes to explain transport behavior in the plasma. This is another reason to improve the general quantity of benchmarkable rotation cases for these codes that the codes can

attempt to explain.

Overall, understanding rotation transport is still a work in progress from a theoretical standpoint and has various important technical impacts. This motivates the need for empirical and semi-empirical observations of rotation transport and generation in a plasma, which is studied in this work. It is also important to provide supporting data for the theoretical modeling and empirical extrapolations of rotation in plasmas.

2.2 Theories of Momentum Transport and Generation

There has been a wide array of momentum transport and generation theories. These theories often deal with momentum transport as a whole and sometimes with a specific aspect of rotation, such as the spin-up associated with H-modes. Brief descriptions of several of the prominent theories are listed below. Note that in most of these equation C.G.S units are used because they are preferred by the original authors.

2.2.1 Neoclassical Theory

Perhaps the most widely used description for rotation in a tokamak arose from neoclassical theory, which stems from the seminal paper by Hirshman and Sigmar [26], which derives a matrix calculation for various plasma parameters from first principles. Neoclassical poloidal and toroidal rotation are calculated in detail in [27]. The primary results of these neoclassical calculations are listed in the equations below. The poloidal rotation results assumes that the impurity density is significantly below the main ion density and the ion thermal velocity is significantly above the impurity thermal velocity. The poloidal rotation values for the ion and impurity species (where the subscript i is for ions and I represents impurities) are

$$V_\theta^i = \frac{1}{2} v_{T_i} \rho_i \left(K_1 \frac{1}{L_{T_i}} \right) \frac{B B_t}{< B^2 >} \sim \frac{\rho_i}{a} v_{Ti} \tag{2.1}$$

$$V_\theta^I = \frac{1}{2} v_{T_i} \rho_i \left[\left(K_i + \frac{3K_2}{2} \right) \frac{1}{L_{T_i}} - \frac{1}{L_{p_i}} + \frac{Z_i}{Z_I} \frac{T_I}{T_i} \frac{1}{L_{p_I}} \right] \frac{BB_t}{< B^2 >} \sim \frac{\rho_e}{a} v_{Ti} \tag{2.2}$$

where $L_T^{-1} \equiv \partial \ln T_i / \partial r$, $L_n^{-1} \equiv \partial \ln n / \partial r$, $L_p^{-1} \equiv \partial \ln p_i / \partial r$, $v_{T_i} \equiv \sqrt{2T_i/m_i}$, and $\rho_i \equiv m_i v_{T_i} / Z_i e B$. The terms K_1 and K_2 are coefficients that can be derived for the Pfirsch-Schluter and banana regimes, and they depend on collisionality, aspect ratio, $\alpha = n_I Z_I^2 / n_i Z_i^2$, the mass of the ions and impurities, and the thermal velocities of the ions and impurities. The toroidal rotation is solved for two cases: small α and $\alpha \sim 1$. In a hot plasma core in the banana and banana-plateau regime, α will not necessarily be small so the toroidal rotation frequencies are found to be

$$\omega_i = \frac{cE_r}{RB_p} - \frac{1}{2} \frac{v_{T_i}}{R} \rho_{ip} \left(L_{00}^{ii} \frac{1}{L_n} + (L_{00}^{ii} - L_{01}^{ii}) \frac{1}{L_{T_i}} \right) \tag{2.3}$$

$$\omega_I = \frac{cE_r}{RB_p} \tag{2.4}$$

where ω is the toroidal rotation frequency, and L_{00}^{ii} and L_{01}^{ii} are constants of order unity that depend on plasma parameters and are plotted in detail in [27]. These calculations are fairly complicated, which makes in depth neoclassical calculations cumbersome, and they are normally performed by codes such as NCLASS [28]. In general, poloidal rotation is small while toroidal rotation is large if $E_r/B_p \sim v_{Ti}$.

The equations above can be simplified and solved on axis for the ion and impurity species in the plasma. These equations are shown below.

$$V_{||}^I = -\frac{\tau_{ii} Z_i e E_{||}}{m_i} \frac{Z_I - Z_i}{Z_I} \frac{\sqrt{2} + 13\alpha/4}{(1+\alpha)(\sqrt{2}+\alpha)} \frac{n_i m_i}{n_i m_i + n_I m_I} + \frac{n_e m_e}{n_i m_i + n_I m_I} \frac{\sigma_{\text{Spitzer}}}{n_e e} E_{||} \tag{2.5}$$

$$V_{||}^i = \frac{\tau_{ii} Z_i e E_{||}}{m_i} \frac{Z_I - Z_i}{Z_I} \frac{\sqrt{2} + 13\alpha/4}{(1+\alpha)(\sqrt{2}+\alpha)} \frac{n_I m_I}{n_i m_i + n_I m_I} + \frac{n_e m_e}{n_i m_i + n_I m_I} \frac{\sigma_{\text{Spitzer}}}{n_e e} E_{||} \tag{2.6}$$

where $\sigma_{\text{Spitzer}} = (\sqrt{2} + 13Z_i/4)n_e e^2 \tau_{ee}/Z_i m_e(\sqrt{2} + Z_i)$, and $E_{||}$ is the toroidal electric field.

An example of the calculated neoclassical impurity rotation time trace during an example L-mode discharge (with two magnetic geometry transitions) is shown below in figure 2-1. This calculation only holds at the axis of the plasma, and the experimental data are overplotted from this same discharge to show the comparison of the calculation to actual experimental data. Overall, it is seen that neoclassical theory is not capable of properly explaining the rotation observed in the plasma. This disagreement has been studied in more significant detail in [29, 30].

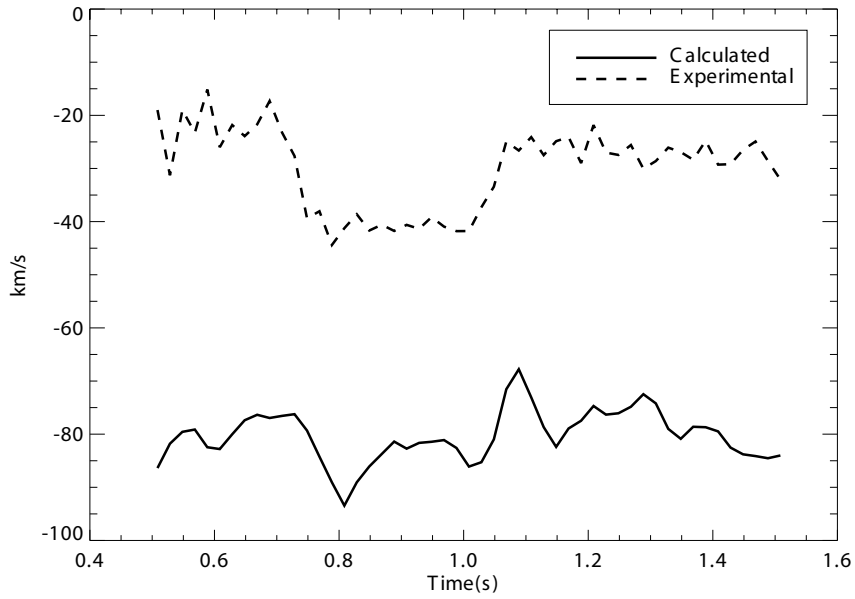

Figure 2-1: Neoclassical calculation of the core impurity rotation during an L-mode discharge with two magnetic geometry transitions (at t=0.7 s and t=1.0 s).

2.2.2 Revisited Neoclassical Theory ('Sub'neoclassical theory)

The revisited neoclassical theory [31] seeks to correct some limitations in the neoclassical theory by removing the assumptions that all macroscopic scale lengths (for example qR, r, and L_n) are of the same order, that inertia is negligible, and that finite Larmor radius effects are not important. In neoclassical theory, the ratio of the ion

perpendicular transport to the ion parallel transport, Λ_1, is generally taken to be 0. In the revisited theory, the ratio is taken to be

$$\Lambda_1 = \frac{q^2R^2}{\chi_{||,i}/N}\frac{\partial T_i}{eBr\partial r} = 0.255\frac{1}{\Omega_i\tau_i}\frac{q^2R^2}{rL_{T,i}} \tag{2.7}$$

where N is the plasma density, Ω_i is the ion cyclotron frequency, and $\chi_{||,i}$ and τ_i are the parallel ion diffusivity and collision time as defined by Braginskii,. In L-mode, it is found that the ratio is of order 0.1 for characteristic plasmas. For H-modes or in other transport barrier regions, this number can be significantly higher, meaning that the assumptions in neoclassical theory have to be modified. This theory assumes high collisionality (which is not always justified in a tokamak core) and the following scaling relations.

$$(L_\psi/r) \sim r/(qR) \sim \hat{v}_j$$

$$(a_i/L_\psi) \sim (m_e/m_i)^{1/2}$$

where L_ψ is the characteristic scale length in the plasma (such as L_T or L_N). Using these assumptions and fairly involved calculations about the finite Larmor radius corrections, this model generates several equations for the transport of particles, momentum, and energy in the plasma.

$$\begin{aligned}\frac{\partial N}{\partial t} = {} & \frac{\partial}{\partial r}\left(\frac{m_e}{e^2\tau_e}\frac{P}{B^2}\left[2+0.5\eta+(2.68+1.55\eta)q^2\right]r\frac{\partial \ln N}{\partial r} - r\frac{B_\theta}{B^2}N\frac{U}{2\pi r}\right) - \\ & - \frac{1}{r}\frac{\partial}{\partial r}\Big(\frac{m_e}{e^2\tau_e}\frac{P}{B^2}\frac{1}{Q^2+S^2}\Big[0.57Q^2+\left((2.03\eta-9.50)\frac{T}{eB}\frac{\partial \ln N}{\partial r}+1.15\frac{E_r}{B}\right)Q+ \\ & + 3.38\frac{T}{eB}\frac{\partial \ln T}{\partial r}\left((1.5\eta-1)\frac{T}{eB}\frac{\partial N}{\partial r}+2\frac{E_r}{B}\right)\Big]q^2r\frac{\partial \ln T}{\partial r}\Big)\end{aligned} \tag{2.8}$$

$$\frac{2R^2}{5r}\frac{\partial}{\partial t}\frac{B_\theta U_{||,i}}{B_\phi}+\frac{3r}{5}\frac{\eta_{0,i}/m_i N}{q^2R^2}\left(\frac{BU_{\theta,i}}{B_\phi}-k\frac{T_i}{eB}\frac{\partial \ln T_i}{\partial r}\right)$$
$$=\Big[\frac{T_i}{eB}\left(\frac{9}{4}\frac{\partial \ln N}{\partial r}+\frac{1}{8}\frac{\partial \ln T_i}{\partial r}\right)\frac{B_\theta U_{||,i}}{B_\phi}-\left(\frac{1}{4}\frac{\partial \ln N}{\partial r}+\frac{1}{8}\frac{\partial \ln T_i}{\partial r}\right)\frac{E_r}{B}+2\frac{T_i}{eB}\frac{\partial}{\partial r}\frac{B_\theta U_{||,i}}{B_\phi}+$$
$$\frac{E_r^2}{B^2}+\left(\frac{T_i}{eB}\right)^2\left(2\frac{\partial \ln N}{\partial r}+\frac{1}{2}\frac{\partial \ln T_i}{\partial r}\right)\left(-\frac{1}{4}\frac{\partial \ln N}{\partial r}+\frac{3}{8}\frac{\partial \ln T_i}{\partial r}\right)\Big]\frac{S}{Q^2+S^2}\frac{T_i}{eB}\frac{\partial \ln T_i}{\partial r}-$$
$$-\frac{1}{P_i}\frac{T_i}{eB}\frac{\partial}{\partial r}\times\left(P_i\left[\frac{T_i}{eB}\left(\frac{\partial \ln N}{\partial r}-2\frac{\partial \ln T_i}{\partial r}\right)+5\frac{E_r}{B}-4\frac{B_\theta U_{||,i}}{B_\phi}\right]\frac{S}{Q^2+S^2}\frac{T_i}{eB}\frac{\partial \ln T_i}{\partial r}\right) \tag{2.9}$$

$$3N\frac{\partial T}{\partial t}=\frac{1}{r}\frac{\partial}{\partial r}\left(\left[1+\frac{1.60q^2}{1+(Q^2)(S^2)}\right]r\chi_{\perp,i}\frac{\partial T_i}{\partial r}\right) \tag{2.10}$$

where $S=2(\chi_{||,i}/rN)B_\theta^2/B^2$, $Q=4(U_{\theta,i}B_\phi/B)-5\left[(T/eB)\partial(\ln(NT^{1/2}))/\partial r\right]$, η is the resistivity, P is the pressure, and U is the plasma flow. These equations lead to a radial electric field relation

$$E_r=B_\phi\left[\frac{B_\theta U_{||,i}}{B}+\frac{T_i}{eB_\phi}\left(\frac{\partial \ln P_i}{\partial r}+2.1\frac{\partial \ln T_i}{\partial r}\right)\right] \tag{2.11}$$

In sub-neoclassical theory, the radial electric field has a direct relation defined in Equation 2.11. It is worth noting that the electric field in neoclassical theory, however, requires a higher order calculation or can be derived from the rotation velocity.

Overall, these equations can lead to relations that appear to explain the transition from L-H modes and highly sheared profiles in the plasma which is discussed in more detail in the referenced paper. These equations can reduce to the neoclassical forms under certain assumptions, and they can reproduce magnitude of the flows but not the time scales [32]. The time scale differences are likely due to turbulence in the plasma. Despite the improvements, the model is still extremely cumbersome and does not agree with all experimental results.

2.2.3 Shaing Theory

This theory [33] seeks to explain the toroidal flow reversal during an H-mode through the use of neoclassical quasilinear theory. In the Shaing model, the drift kinetic equation 2.12 is solved to first order.

$$\frac{\partial f}{\partial t} + \left(v_{||}\hat{n} + \mathbf{v}_d\right) \cdot \nabla f + \frac{e}{M}\frac{\partial \Phi}{\partial t}\frac{\partial f}{\partial \epsilon} = C(f) \tag{2.12}$$

where f is the particle distribution function, $v_{||}$ is the parallel particle speed, $\mathbf{B}$ is the magnetic field, $\hat{n} = \mathbf{B}/B$, $\mathbf{v}_d$ is the drift velocity, Φ is the electrostatic potential, ϵ is the particle energy, and $C(f)$ is the Coulomb collision operator. By applying quasilinear theory ($\tilde{\Phi} = \sum_{m,n,\omega} \Phi_{m,n,\omega} \exp i(\omega t + (m\theta - n\zeta + \eta_{mn}))$, where m and n are the poloidal and toroidal mode numbers, ω is the mode angular frequency, and η_{mn} is the phase shift), taking the Krook collision operator ($C = -\nu f$) and implementing a series of simplifications, the following relation is found

$$\Gamma_\phi = -\chi_\phi \frac{\partial}{\partial \psi}\left(\frac{NMIU_{||}}{B}\right) - \chi_\phi L_\psi \left(\frac{NMIU_{||}}{B}\right) \tag{2.13}$$

where $I = RB_t$, N is the density, $U_{||}$ is the parallel velocity, χ_ϕ is the momentum diffusivity, ψ is the poloidal flux function, and

$$L_\psi = \left(\left[\omega + (mU_p - nU_t) - \frac{2}{5}\left(\frac{5}{2} - x_0^2\right)\left(\frac{mq_p}{p} - \frac{nq_t}{p}\right)\right] \times (mT\mathbf{B} \times \nabla\psi \cdot \nabla\theta / M\Omega B)^{-1}\right) \tag{2.14}$$

where T is the temperature, m is the poloidal mode number, n is the toroidal mode number, $x_0 = \omega_{mn}^E/(v_t \cdot |m - nq|\hat{n} \cdot \nabla\theta)$, ω_{mn}^E is the Doppler shifted mode frequency, and q is, as normal, the safety factor.

Equation 2.13 has a diffusive term and a term proportional to the velocity, the convective pinch. Assuming that $\omega_{mn} \approx \omega_{*i} = -(mT\mathbf{B} \times \nabla\theta/M\Omega B) \times (p'/p)$, $x_0^2 < 1$, $\omega + (mU_p - nU_t) \approx 0$, and $|q_t/p| \ll |q_p/p|$, the term L_ψ reduces to $-5/2(T'/T)$. The convective pinch is then found to be $v_\phi = -5/2(T'/T)\chi_\phi$, but if the density gradient is much larger than the temperature gradient the convective pinch can become an

outward velocity. Overall, this model finds that the toroidal rotation profile in a plasma with no external sources is

$$\frac{\partial U_{||}}{\partial \psi} - \frac{5}{2}\frac{T'}{T}U_{||} = 0 \tag{2.15}$$

In summary, the Shaing model provides a simple equation to predict the toroidal rotation in an Ohmic plasma. Shaing also conjectures that his model can explain the L-H mode transition velocity, through ITG mode suppression or symmetry breaking causing the pinch velocity to change sign. This model has been compared to experimental profiles in [30] and matched the plasma rotation in an ELM-free (intermittent) H-mode but not in an EDA (steady) H-mode. While the Shaing model has been able to reproduce some of the experimental data, it is still not a perfect model, as seen by its inability to match steady H-mode data.

2.2.4 Accretion Theory

The accretion model was proposed by B. Coppi [34, 35] to explain rotation changes in an H-mode transition via an edge particle mode. The model is another quasilinear theory and considers electrostatic modes of form $\hat{\phi} = \tilde{\phi}(x_0)\exp(-i\omega t + ik_y y + ik_{||}z)$ localized around a surface (x=x_0) in the plasma. This model generates a dispersion relation

$$\overline{\omega}\,(1 - i\epsilon_k) \approx k_y v_{*e} - \frac{cT_e}{eB}\frac{\overline{\omega} - i\nu_D}{\overline{\omega}^2}k_{||}k_y\left[\frac{dv_{||}}{dx} + \frac{k_{||}}{\overline{\omega}}\frac{1}{m_i n}\frac{dp_i}{dx}\right] \tag{2.16}$$

where γ is the mode growth rate, ω is the mode frequency, $\overline{\omega} \equiv \omega - k_{||}v_{||}(x_0)$ is the Doppler shifted frequency, $k_{||}$ is the wavenumber along the magnetic field line, k_y is the wave number perpendicular to the magnetic field line, ϵ_k represents small non-linear effects that can drive the mode unstable, and v_{*e} is the diamagnetic velocity. This dispersion relation can reduce to the ITG dispersion relation under the assumption that $d\ln T_i/d\ln n_i > \omega^2/(k_{||}v_{thi})$. It is argued that ITG turbulence is suppressed during the H-mode and turbulence is strongly driven in the edge of the plasma by steep density gradients. A radial flux of angular momentum is deduced in the plasma

of the form

$$\Gamma_k \approx -\frac{2\gamma_k}{\overline{\omega}_k^2} < |\hat{v}_{Ex}|^2 > \left[m_i n_i \frac{dv_{||}}{dx} + 2\frac{k_{||}}{\overline{\omega}_k}\frac{dp_i}{dx} \right] \tag{2.17}$$

where $\hat{v}_{Ex}$ is the E×B flow of the perturbation. In Equation 2.17, it is seen that there is a diffusive term and an inflow proportional to the pressure gradient. This pressure gradient driven inflow is suggested to generate the H-mode rotation change.

This theory explains the rotation during an H-mode by having a radial inflow of momentum and the conservation mechanism being an edge mode generating an opposite toroidal flux toward the tokamak wall. The turbulent modes in the plasma are primarily involved in the radial influx of the angular momentum, and as the pressure gradient increases the pinch increases as well. Overall, accretion theory proposes a diffusive and convective form of the angular momentum flux in an H-mode explained by the quasilinear theory. This model, however, is difficult to confirm experimentally due to its reliance on proper identification of the turbulent modes in a plasma.

2.2.5 Summary of Theoretical Models

Overall, the various theoretical models are complicated and require fairly involved calculations in all but the most simple plasma cases. Furthermore, the models have not been able to reproduce experimental rotation results. It is widely considered that many of the difficulties predicting rotation in plasmas stem from anomalous turbulence caused transport. These turbulent fluxes cause an increase in the momentum flux in a not fully understood mechanism. In order to be able to predict and make claims about plasma behavior semi-empirical models must be used.

2.3 Simplified Model of Rotation

The simplified model of momentum transport was introduced by W.D. Lee [36], and it represents the transport of rotation in a similar description as density and temperature

transport. Rotation is considered to have a diffusive, χ_ϕ, and convective transport term (sometimes called a pinch), V, where the diffusive term flattens the rotation profile and is proportional to ∇v, while the convective term can create peaked profiles and is proportional to v. The remainder of the rotation profile is considered to depend on either a source term, S, or the residual stress, $\overleftrightarrow{\Pi}$ [37], which represents the coupling of rotation to other profile effects (the tensor symbol is dropped for simplicity in the rest of this work). The full equation describing the transport of momentum is then

$$\frac{\partial P}{\partial t} + \nabla \cdot \Gamma = S \tag{2.18}$$

where $P = nmv$ and Γ is the radial flux of momentum. Using the diffusive, convective, and residual stress representation of momentum, Γ is then

$$\Gamma = -\chi_\phi \nabla P - VP + \Pi \tag{2.19}$$

Equation 2.18 is analytically tractable under certain approximations making it convenient to solve. This is generally done by assuming that the diffusion is constant in space and time, convection is a function of radius $V = v_c(r/a)$, S=0, Π=0, and density remains fixed as a function of time. Using these approximations, the equation can be transformed into the following form

$$\frac{\partial v}{\partial t} - \chi_\phi \left[\frac{\partial^2}{\partial r^2} v + \left(\frac{1}{r} + \frac{v_c r}{a \chi_\phi} \right) \frac{\partial v}{\partial r} + \frac{2 v_c}{a \chi_\phi} v \right] = 0 \tag{2.20}$$

Equation 2.20 has solutions of the form

$$v(r,t) = \sum_{n=0}^{\infty} C_n \frac{1}{r} e^{-t/\tau_n} e^{-v_c r^2/(4a\chi_\phi)} M_{\frac{\lambda_n \chi_\phi a + v_c}{2 v_c}} (v_c r^2/(4a\chi_\phi)) \tag{2.21}$$

In this solution, M is a Whittaker function, λ_n is the n-th zero of the Whittaker function, and $\tau_n = a^2/(\lambda_n \chi_\phi)$. Using experimental data, it is possible to fit various plasma transitions with this model, and, thus, derive the momentum diffusion and convective velocity terms, which has been performed in W.D. Lee's thesis [38].

2.4 Improved Simple Model of Momentum Transport or "Toy Model"

The simple model of momentum transport is able to simulate momentum changes in the plasma under a large number of simplifying conditions. This model was able to reproduce the changes seen in well-behaved EDA H-mode transitions. These conditions were implemented in the model in a large part because the data quality was unable to support more sophisticated models: there were only three positions with measured rotation velocity in the plasma. With the creation of HiReX Sr (see Section 3.1.1) and its resultant spatially and temporally resolved profiles, it became possible to use the profiles of $v_\phi(r,t)$ to remove many of the restrictions inherent in the simple model of momentum transport.

Specifically in the Improved Simple Model of momentum transport, it is allowed for the diffusive and convective terms to vary with both space and time. The simplified model of momentum then becomes

$$\frac{\partial P}{\partial t} = -\nabla \cdot \Gamma + S \tag{2.22}$$

$$= -\nabla \cdot (-\chi \nabla P - v_c P + \Pi) + S \tag{2.23}$$

$$= -\nabla \cdot (-\chi \nabla P - v_c P) + (S - \nabla \cdot \Pi) \tag{2.24}$$

leading to a final expression for the momentum confinement of

$$\frac{\partial P}{\partial t} - \left[\chi P'' + P'\left(\chi' + \frac{\chi}{r} + v_c\right) + P\left(v_c' + \frac{v_c}{r}\right)\right] = \alpha \tag{2.25}$$

where $\alpha = S - \nabla \cdot \Pi$ is often referred to as the source term in this work and the prime represents a radial derivative. An external source, S, is often difficult, if not impossible, to resolve from a self-generated source $\nabla \cdot \Pi$.

In Equation 2.25, the velocity term is measured by the HiReX Sr spectrometer, the plasma density is measured by the Thomson system (see Section 3.1.4), and the

radii of the measurements in the plasma are inferred from EFIT reconstructions [39]. The terms in this equation that are not known are the momentum diffusion term, the momentum convection term, and the source/residual stress term. It has been seen from previous work [40, 41, 42] that the momentum and energy diffusion terms are generally of similar order. The relationship of momentum diffusion and energy diffusion is generally quantified by a term from thermal fluids research: the Prandtl number, $P_r = \chi_\phi/\chi_i$. The thermal diffusivity can be calculated using the TRANSP code, and, in this work, it is generally taken that $P_r = 1$. The convective transfer term has been calculated from theory, and there are also less rigorous methods of calculation. In general, the convection is related to the momentum diffusivity via some direct equation depending on the plasma profiles.

In summary, taking experimental values for rotation and density and calculated values for diffusivity (P_r=1, χ_i calculated by TRANSP) and convection (as described in the next section), Equation 2.25 is fully solvable for α, the source term. This allows one to attempt to infer the behavior of the residual stress/source term from a purely experimental standpoint. It does require some assumptions on the separability of the residual stress and external source term but nevertheless can provide major insight into the plasma rotation behavior. This equation is not a theoretical description but should rather be considered a "Toy Model" for the rotation.

This model makes no attempt at explaining the underlying theory of the generation of momentum flux from first principles and should purely be considered an experimental approach to the issue. There are, in fact, major concerns about the convective term's Galilean invariance since it is proportional to a term that depends on the reference frame of the observer [43]. Furthermore, the model calculates the residual stress as a force density in the plasma, which is effectively a slab model.

2.4.1 Forms of the Convective Velocity

There are numerous forms of the convective velocity that are derived from first principles and some that are simply used as fitting parameters from empirical observations. The various forms of the convective velocity will be discussed below.

1. **None**. The first test for the convective velocity is, in fact, setting it to zero. As such, this tests what the source profile would look like with pure diffusion and also checks if diffusion is enough to explain the observations. The form of Equation 2.25 becomes purely diffusive and is shown in Equation 2.26.

$$\frac{\partial P}{\partial t} - \left[\chi P'' + P'\left(\chi' + \frac{\chi}{r}\right)\right] = \alpha \tag{2.26}$$

   It is known that diffusion is incapable of solely explaining rotation profiles due to peaked steady state rotation on axis in various plasma states; these peaked profiles, in fact, were the cause for the introduction of the convective velocity. The freedom of the shape of the source profile allows using this model despite the limitations of the diffusive term.

2. **W.D. Lee form**. One of the simplest forms of the convective velocity that has been explored was first suggested by W.D. Lee's thesis work. In this form, $v_c = v \cdot r/a$, where v is a constant and a is the minor radius of the plasma. This form of the convective velocity allows solving the momentum transport equation in an analytical form if the residual stress is not included. The W.D. Lee convective velocity is not derived from basic principles, but given its applicability to H-mode profiles in Alcator C-Mod, it provides a solid comparison.

3. **Peeters form**. The Peeters form [44] is a first principles derivation of the convective velocity from gyrofluid equations in the ITG regime. The equation derived for this pinch is shown below

$$\frac{v_r}{\chi} = \frac{1}{L_n} - \frac{4}{R\tau} \tag{2.27}$$

   where $\tau = T_e/T_i$.

4. **Yoon form**. The Yoon form [45] of the convective velocity is also derived from first principles. It is derived in the ITG regime near the critical temperature

gradient in a torus. The pinch is found to be

$$\frac{v_r^\omega}{\chi^\omega} = \frac{1}{L_n} - \left(\frac{5}{2} - \alpha_c\right)\frac{1}{L_{T_i}} - \frac{8}{5}\alpha_c\frac{1}{R} \tag{2.28}$$

$$\alpha_c = \frac{\frac{3}{2}(\eta_i - 1)}{\left(\eta_i\left(1 - \frac{4}{3}L_{T_i}/R\right)\right)} \tag{2.29}$$

where L_n and L_T are the density and temperature gradient scale lengths. The term η_i is the ratio of the density scale length to the temperature scale length $\partial_r \ln T/\partial_r \ln n$. In the flat density regime, α_c reduces to $(3/2)/(1-(4/3)L_{T_i}/R)$.

5. **No Residual Stress** The final calculation for convection is not a calculation, *per se*. If a rotation profile is available, it is possible to scale the convective term, as a function of space and time, to minimize the deviation of the calculated velocity to the experimental velocity. This can provide insight into which of the proposed convective terms is closest to the correct shape but, given the likely presence of the residual stress, should not be considered canon.

It is notable that all of the derivations of the pinch velocity are performed in the ITG regime, which, admittedly, is the most common turbulence mode in most tokamaks. It is possible to have a tokamak in the trapped electron mode (TEM) dominated regime, however. No derivations for analytic forms of the TEM pinch have been identified, but there is an observed momentum pinch during the TEM [46]. The pinch is fairly similar to the pinch in the ITG case, so it can either be approximated with the forms presented here or tested as a constant value.

2.4.2 Forms of the Residual Stress

The form of the residual stress is not critical for a majority of this work, which aims to deduce the shape of the residual stress, subject to various conditions. It is, nevertheless, a useful exercise to compare the results found here against derived forms of the residual stress to provide tests of theory.

A variety of these derivations have been created over time, and some examples are listed below.

1. **P.H. Diamond**. The form of the residual stress derived by P.H. Diamond's group from first principles [47, 48]. It assumes a monotonic q-profile and is derived in an ITG microinstability dominated plasma. This form is particularly simple and has dependencies that are explained in many devices, such as the dependence of the rotation on the gradient of the ion temperature. This form is calculated to be

$$\Pi^{res} = -\rho_* \frac{L_s}{2c_s} \chi_i \left(\frac{\nabla T}{T} \right)^2 v_{th,i}^2 \tag{2.30}$$

where c_s is the sound speed, χ_i is the ion thermal diffusivity, $v_{th,i}$ is the ion thermal speed, ρ_* is the normalized Larmor radius, and $L_s = R_0 q^2 / r(\partial q / \partial r)$ is the shear scale length. This form of the residual stress also allows an approximate prediction for the velocity, which is calculated to be

$$\frac{\langle v \rangle}{v_{th,i}} = \frac{1}{2} \rho_* \frac{\chi_i}{\chi_\phi} \frac{L_s}{L_T} \left(\frac{T_i}{T_e} \right)^{1/2} \tag{2.31}$$

where χ_ϕ is the momentum diffusivity.

2. **Yoshida Model**

In [49], M.Yoshida proposed a residual stress form which is proportional to the ion pressure gradient. The form is shown below

$$\Pi_{res} = \alpha_k \chi_\phi \nabla P_i \tag{2.32}$$

where α_k is a constant, which was taken to fit experimental rotation data. In JT-60U, it was found to range from 1.0×10^{-7} to 3.0×10^{-7} m^{-1} s, in a variety of L and H-mode plasmas. The convective and diffusive terms were characterized using scaling relations found from beam perturbation experiments on JT-60U

[50]. It is notable that C-Mod's densities are generally high enough that, from the scaling relations in [50], χ_ϕ/χ_i would be of order one, as is used in this thesis.

2.5 Summary

The background of momentum transport and generation has been presented in this chapter. This background chapter goes over a large overview of basic predictions about transport in a tokamak. Specifically, the neoclassical theory of momentum is introduced along with some of its predictions about the plasma transport. It is seen that neoclassical theory is incapable of predicting the rotation in a tokamak correctly. Other theories of rotation are briefly presented as well. Revisited neoclassical theory has been seen to have an extremely complicated relation for the density, momentum, and energy transport, but it is capable of predicting the magnitude of the flows in plasmas. The Shaing model explains rotation in an L-H transition, but it has only been successful at predicting rotation during intermittent H-modes. Accretion theory explains the rotation changes in a plasma and predicts a momentum flow into the core from an H-mode transition, but is not as applicable for quantitative analysis.

Most of the models are extremely complicated and difficult to use to make momentum predictions. This leads to the Simplified Model of Rotation, which was presented in this section, along with the more advanced "Toy Model." These semi-empirical models are used extensively in this work, and their advantages and limitations are presented here. Most importantly, it is shown that these models are not theoretical tools but are rather tools for experimentalists to make quantitative and qualitative observations about the rotation transport and generation in plasmas. The various forms of the diffusive and convective terms along with their theoretical underpinnings are presented in this section as well. Finally, an overview of the theory for the terms not explained by diffusive and convective transport is shown.

The experimental work in this thesis will attempt to explain rotation data in various regimes of operation using the "Toy Model." In this model, it is assumed that

rotation profiles, momentum diffusion, and momentum convection are known from experimental data and theoretical predictions, and the remainder of the rotation is explained via the use of a residual stress/source. The end result, as shown in Chapter 6, is that the model does well explaining the profiles in an SSEP case, and fairly well in rotation reversals, H-modes, and I-modes, but major amounts of the physics in the latter cases have to explained through the use of the residual stress/source term.

Chapter 3

Experimental Set-up

The vast majority of this work has required the accurate measurement of the Alcator C-Mod rotation profiles. While rotation is the primary measurement, a large set of diagnostics is required for proper analysis to be successful. In this section, short descriptions will be provided of the primary diagnostics and analysis tools used, as well as a more detailed description of the imaging x-ray spectrometer on C-Mod.

3.1 Diagnostics

3.1.1 HiReX Sr

The HIgh REsolution X-ray spectrometer with Spatial resolution (HiReX Sr) has been the primary work horse of rotation and ion temperature measurement at Alcator C-Mod. HiReX Sr is described in detail in [51] and [52]. A summary of the function of this device is provided below. HiReX Sr is the prototype spherically bent imaging X-ray spectrometer of a design by M. Bitter and K. Hill [53, 1] and currently used on a variety of other devices (for example LHD and KSTAR [54, 55]).

X-ray spectrometers use dispersive elements, crystals or gratings, for spectral resolution. Crystals disperse X-rays through Bragg reflection ($n\lambda = 2d\sin\theta$), but flat crystals can only function with an extended X-ray source through the use of a slit to avoid degeneracy of different energy X-rays fulfilling the Bragg condition at different

angles on the crystals. Alternatively a cylindrically bent crystal can be used to avoid this degeneracy, and these systems have been used extensively but they do not have spatially resolving capabilities. Spherically bent crystals both avoid the necessity of a slit and have the capability spatial resolution.

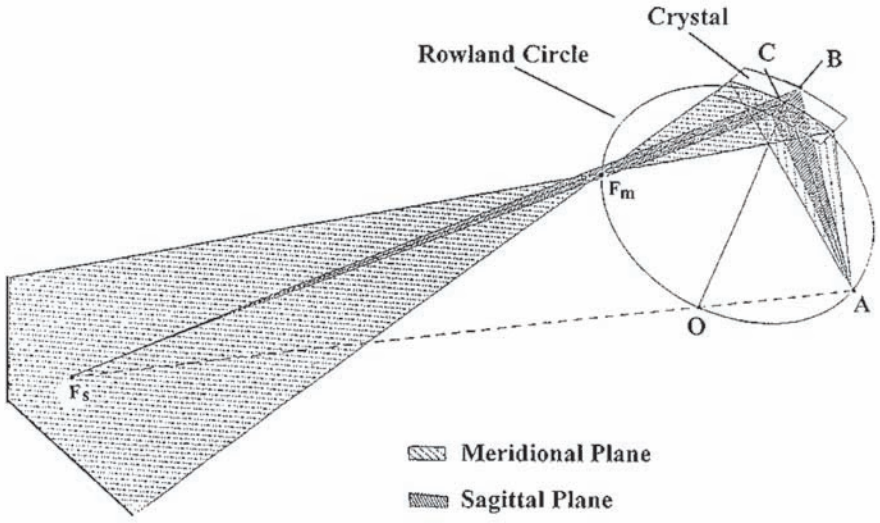

Figure 3-1: Geometry of the X-ray reflection from a spherically bent crystal. Figure from [1]

HiReX Sr uses spherically bent crystals as dispersive elements to allow for both spatial and spectral resolution. The spherical geometry of the crystal causes the X-rays to be focused in both the saggital (vertical) plane, leading to spatial resolution, and meriodonal (horizontal) plane, leading to spectral resolution. The crystal parameters are listed in Table 3.1. HiReX Sr uses four Pilatus II[1] x-ray cameras (487×195 pixels each of which is an x-ray detector of size 172×172 μm^2) to image the two-dimensional shape of helium-like and hydrogen-like argon lines from the plasma with temporal resolution up to 2.7 ms. A picture and engineering figure of the device are shown in Figure 3-2.

Similar to many other crystal X-ray spectrometers, HiReX Sr functions by measuring the Doppler shift and Doppler broadening of emission lines to find the plasma velocity and ion temperature, respectively. HiReX Sr is able to image several emission

[1]See Dectris http://www.dectris.com/sites/pilatus100k.html for details

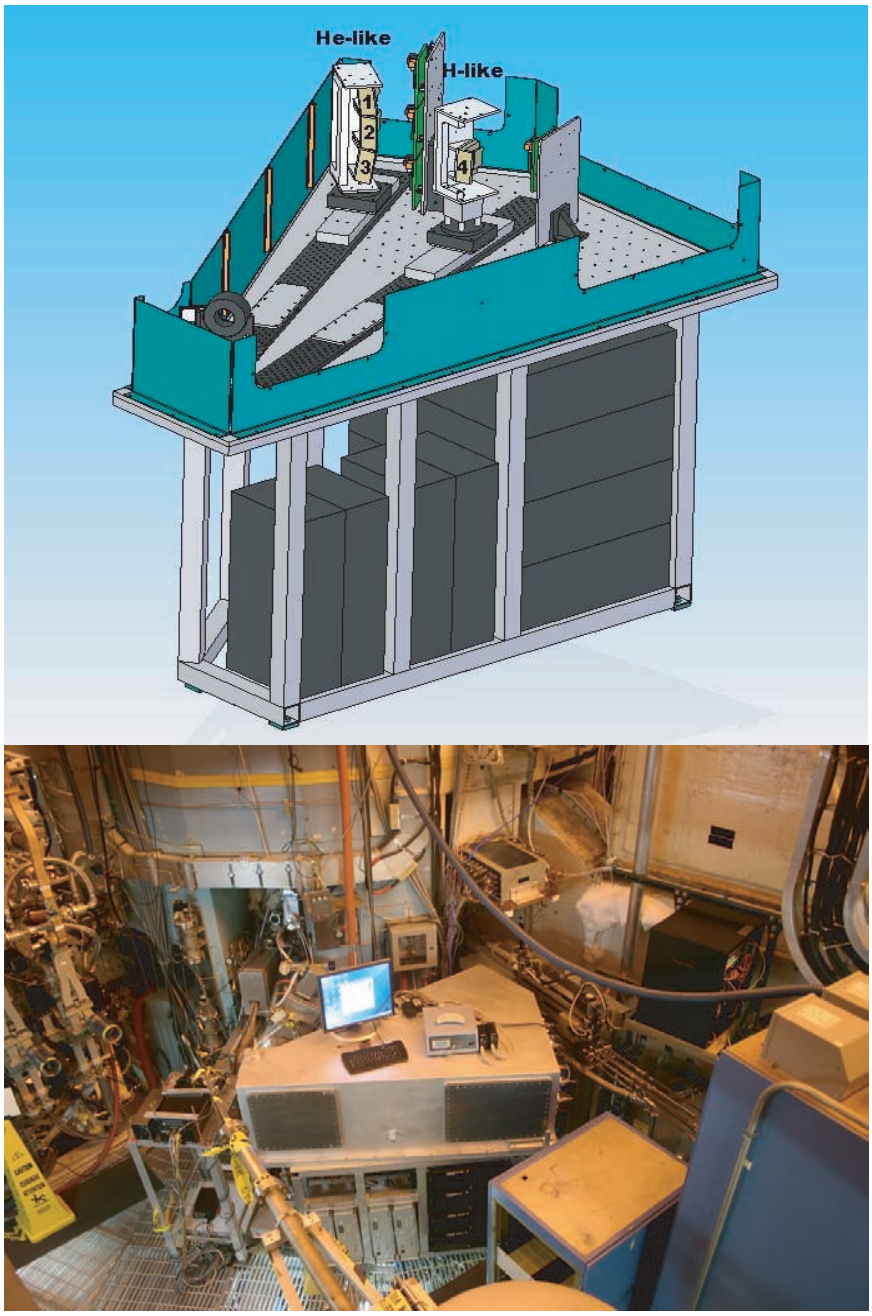

Figure 3-2: Engineering drawing of the inside of the HiReX Sr spectrometer and picture of the spectrometer in the C-Mod cell. The four Pilatus-II modules are numbered from 1-4.

Table 3.1: HiReX Sr crystal parameter values. Both intended and experimental values of the HiReX Sr crystals are presented.

Crystal	Parameter	Value
He-like	Shape	Rectangular
	Size	6.4 cm × 2.7 cm
	2d	4.56225 Å
	Intended Radius of Curvature	144.3 cm
	Measured Radius of Curvature	144.79 cm
	Target Wavelength	3.9494 Å
H-like	Shape	Circular
	Size	R=2.5 cm
	2d	4.56225 Å
	Intended Radius of Curvature	138.5 cm
	Measured Radius of Curvature	139.43 cm
	Target Wavelength	3.7311 Å

lines from hydrogen-like and helium-like argon atoms, but generally only the w, z, Lyman-α 1, and molybdenum (2p-4d in Mo^{32+} lines are used), the previous nomenclature for the lines is taken from [56]. An example spectra of the device is shown in Figure 3-3, and the line description is listed in detail in Tables 3.2 and 3.3.

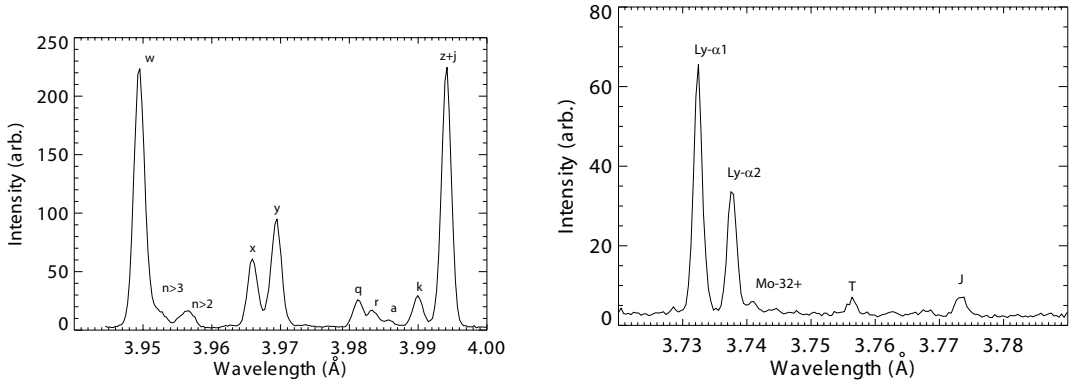

Figure 3-3: Example core averaged spectra from an H-mode discharge with helium-like (left) and hydrogen-like (right) argon lines. Prominent lines are labeled in the figures. Note that the ratios of the w and z lines do not match their theoretical predictions because of vignetting issues discussed in Section 3.1.1

The data taken by HiReX Sr are seen as lines of sight of the emissivity from its targeted argon transitions. Each radial position is, therefore, a line integrated measurement of the emissivity (referred to as brightness) along the line of sight. In

Table 3.2: List of normally visible lines on the HiReX Sr spectrometer helium-like system. Data from [5]

Name	Transition	Wavelength
w	$1s^2\ ^1S_0 - 1s2p\ ^1P_1$	3.94912 Å
n≥3	Several	
n≥4	Several	
x	$1s^2\ ^1S_0 - 1s2p\ ^3P_2$	3.96581 Å
y	$1s^2\ ^1S_0 - 1s2p\ ^3P_2$	3.96934 Å
q	$1s^22s\ ^2S_{1/2} - 1s2p2s\ ^2P_{3/2}$	3.98134 Å
r	$1s^22s\ ^2S_{1/2} - 1s2p2s\ ^1P_{1/2}$	3.98355 Å
a	$1s^22p\ ^2P_{3/2} - 1s2p^2\ ^2P_{3/2}$	3.98567 Å
k	$1s^22p\ ^2P_{1/2} - 1s2p^2\ ^2D_{3/2}$	3.98999 Å
j	$1s^22p\ ^2P_{3/2} - 1s2p^2\ ^2D_{5/2}$	3.99392 Å
z	$1s^2\ ^1S_0 - 1s2s\ ^3S_1$	3.99417 Å

Table 3.3: List of normally visible lines on the HiReX Sr spectrometer hydrogen-like system. Data from [6]

Name	Transition	Wavelength
Lyman α 1	$1s\ ^1S_{1/2} - 2p\ ^2P_{3/2}$	3.731142 Å
Lyman α 2	$1s\ ^1S_{1/2} - 2p\ ^2P_{1/2}$	3.736514 Å
T	$1s2s\ ^1S_0 - 2s2p\ ^1P_1$	3.75526 Å
Q	$1s2s\ ^3S_1 - 2s2p\ ^3P_2$	3.76106 Å
J	$1s2p\ ^1P_1 - 2p^2\ ^1D_2$	3.77179 Å

order to get local measurements of emissivity, plasma rotation, and ion temperature, the line integrated values have to be inverted via a form of Abel inversion. This inversion is described in detail in [51], and the basic outline of the method follows. The emissivity of the lines is assumed to be constant on a flux surface. The shape of the flux surfaces is known from the EFIT reconstructions, and then Equations 3.1-3.3 can be used to deduce the local emissivity, rotation, and temperature.

$$M_{0,j} = \int dl \cdot \epsilon_0(l) \tag{3.1}$$

$$M_{1,j} = \frac{\lambda_0}{c} \int dl \left[\hat{l} \cdot \vec{v}(l)\right] \epsilon_0(l) \tag{3.2}$$

$$M_{2,j} = \int dl \left[\frac{\lambda_0^2}{c^2}(\hat{l} \cdot \vec{v}(l))^2 + w(l)^2\right] \tag{3.3}$$

where l is the path, $\hat{l}$ is a unit vector along the path, ϵ_0 is the emissivity, and $w(l) = \lambda_0^2 k_b T_i(l)/mc^2$. The codes designed to perform these inversions have undergone major revisions to allow multiple analyses based on timing bins and superior error analysis, which has greatly improved the use of HiReX Sr in a variety of experiments.

HiReX Sr Known Concerns

There are some known issues with the HiReX Sr system. These issues are listed here along with their current and/or proposed solutions.

1. **Temperature Variations of Line Position**

   The most important issue that has been discovered with the HiReX Sr spectrometer is a temperature dependent drift of the wavelength positions of the various lines. This drift causes the anomalous appearance of a velocity shift on an inter-shot time span. The velocity shift was observed in 2008, and it was calibrated out of the system through the use of locked modes that brake the rotation to $v_\phi = 0$ within the $q = 2$ surface [57]. While effective, this method suffers from two major drawbacks: consuming plasma discharges which are lim-

ited during an experiment and relying on locked modes whose rotation zeroing is not fully understood.

Resolution of this issue was approached in two ways: understanding the wavelength variation of the emission lines on the crystal and developing an in-situ calibration method for HiReX Sr.

The first issue, variation of the emission line positions, was deduced to be caused by the temperature variations of the crystal [2]. As the crystal changes temperature, the 2d spacing of the crystal changes, and, thus, there is a slight variation of the location of the lines on the detector plane. The linear spacing of the crystal changes as $\Delta d = d \cdot \alpha_{eff} \cdot \Delta T$; the crystal is quartz with an effective expansion coefficient of $\alpha_{eff} = 9.51021 \times 10^{-6}/^{\circ}\mathrm{C}$. Converting to an effective 2d spacing the equation becomes $2d = 2d|_0 \, (1 + \alpha_{eff} \Delta T)$, where $2d|_0$ is the nominal 2d spacing of the crystal. Experimental measurements were taken of the line positions on HiReX as a function of temperature (temperature was raised through external heaters on the HiReX Sr housing and was measured using thermocouples near the crystal); the results of this measurement are shown in 3-4. Inferred crystal effective expansion coefficients from these data are: $6.797 \times 10^{-6}/^{\circ}\mathrm{C}$, $1.067 \times 10^{-5}/^{\circ}\mathrm{C}$, and $1.057 \times 10^{-5}/^{\circ}\mathrm{C}$. This is within 50% of the known value of the expansion coefficient; considering the somewhat crude method of controlling and measuring the temperature of the crystal, this measurement implies that the variation of the emission line is due to the alteration of the 2d spacing of the crystals.

In order to correct for the line drift, either the temperature of the spectrometer can be controlled or an in-situ calibration mechanism can be used. Controlling the temperature was attempted via the installation of thermal shielding. An improvement of the Alcator C-Mod cell conditioning unit also suppressed the large thermal excursions during the day. Nevertheless, day long variations in temperature were not fully controlled. The ideal mechanism for dealing with the line shift would be the implementation of a calibration mechanism in be-

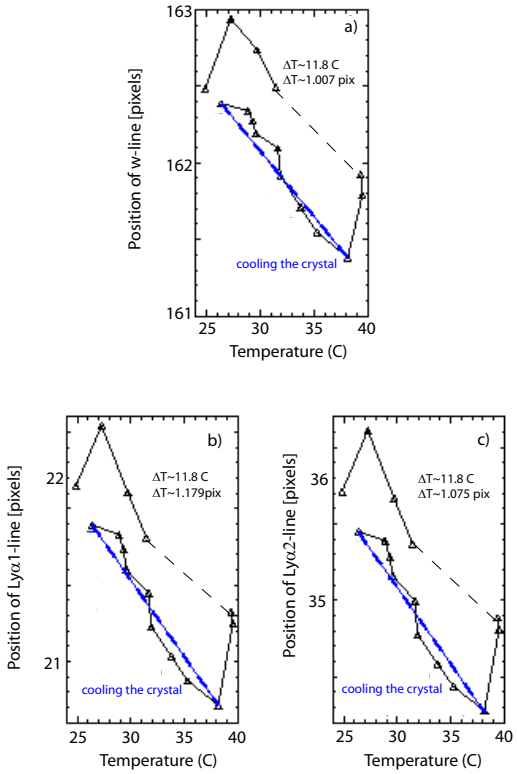

Figure 3-4: Experimental observations of the positions of the argon impurity lines moving as a function of the temperature inside the HiReX Sr spectrometer. The dashed line is shown to connect the actual heating path and highlight the hysteresis in the heating effect. Original figure is from [2].

tween shots at Alcator C-Mod. Two methods were analyzed for achieving this calibration: filter calibration and material fluorescence.

The filter calibration method intends to use strong transmission edges in material filters in an X-ray continuum during plasma discharges to identify known wavelengths on all discharges. This is the proposed calibration method for the ITER X-ray crystal imaging system [58]. Several filter implementations were attempted at Alcator C-Mod using neodymium fluoride and palladium filters. Neodymium has an L-III edge at 1.9972 Å(6.2 keV), which in second order will appear as an edge at 3.994 Å, on top of the z-line in the helium-like spectra. It was found, however, that no edges were seen from the plasma due to the extremely high energies required to excite bremsstrahlung at 1.9972 Å and the crystal second order reflectivity falling off. Palladium has an L-III edge (approximately at 3.9071 Å), slightly outside of the wavelength range of the HiReX Sr systems. It was decided to modify the system to test if it is possible to see the filter transitions at any energy position. No continuum transmissions were seen in this method either. The reason for this was likely the difficulty of aligning an off-normal operation system and the lack of photons in this continuum region. In order for these filter calibrations to work as desired, the filter transition would have to lie on top of one of the emission lines in first order. Unfortunately, the atomic physics of these transitions makes this find unlikely and has not yet been successful at C-Mod.

The second calibration method attempted is the use of a fluorescent plane of material (this method is similar to the flat field calibration method described later in this chapter). A grid of KCl salt is placed between the crystal and the plasma. By using an x-ray tube beyond the crystal (referred to as reflection mode) or the plasma itself (referred to as transmission mode), the potassium K-α 1 and K-α 2 lines are excited and reflect off the crystal. These two lines are within the hydrogen-like spectra and should allow calibrating the detector. This method was attempted on the bench using a copper anode x-ray source, but it

was found that the fluorescence yield was too low to see the necessary X-rays. For use in transmission mode (KCl grid between source and crystal), the grid has to be extremely thin because the 3 keV X-rays are strongly absorbed in the grid itself: at a grid thickness of 10 microns, 60% of the X-rays are reabsorbed.

Two KCl plates were created by evaporating a solution of water and KCl on a mylar film, leading to KCl thicknesses of 5 μm and 10 μm. The mylar film has an x-ray transmission of $\sim$90%, so most of the x-rays from the plasma reach the salt. The film is then positioned between the HiReX Sr crystals and beryllium window. A photograph of this arrangment is shown in Figure 3-5. Despite the argon X-rays making it through the filter when it is installed, no potassium Kα lines were observed.

A third calibration attempt was made using a KCl plate which should expose the top layer of the KCl to plasma radiation. The top layer would then fluoresce and expose the crystal. As long as this fluorescent layer is in the "cone" of the K-α projection from detector to the crystal, it will appear on the crystal. A picture of this arrangement is shown in Figure 3-6. There were no observations of the characteristic fluorescence when exposed to the plasma (1.5 MW bolometric output power), so it appears that the fluorescence yield reflected from the crystal is too low to use as a calibration.

Overall, no in-situ calibration mechanisms have yet been found to work successfully. Despite the concerns about uncertainty of where the rotation profile is zeroed in a locked mode, there is currently no superior mechanism for calibrating the HiReX Sr spectrometer. In the absence of a locked mode calibration, there are two methods for calibrating the HiReX Sr spectrometer: using the HiReX Jr spectrometer (see Section 3.1.2), which is absolutely calibrated, to find the velocity on-axis or finding the location and rotation frequency of the sawtooth precursor mode. These alternate methods are usable within a certain regime of drift in the HiReX Sr frequency and are discussed in more detail in Appendix C.

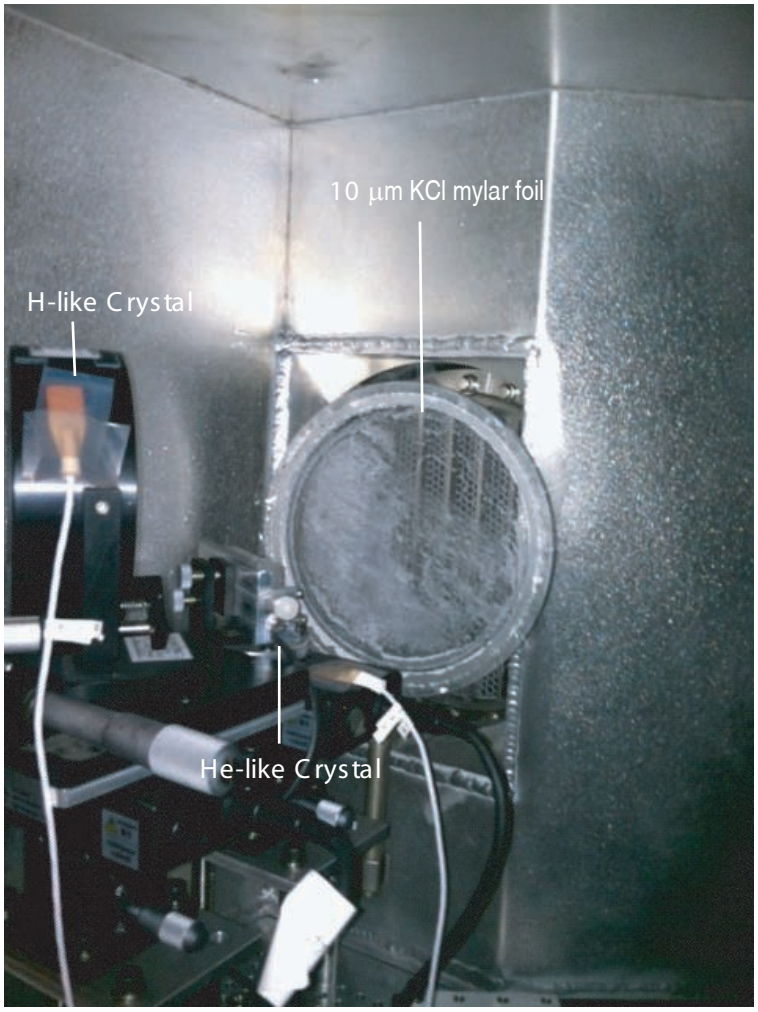

Figure 3-5: Picture of KCl holder installed in the HiReX Sr spectrometer.

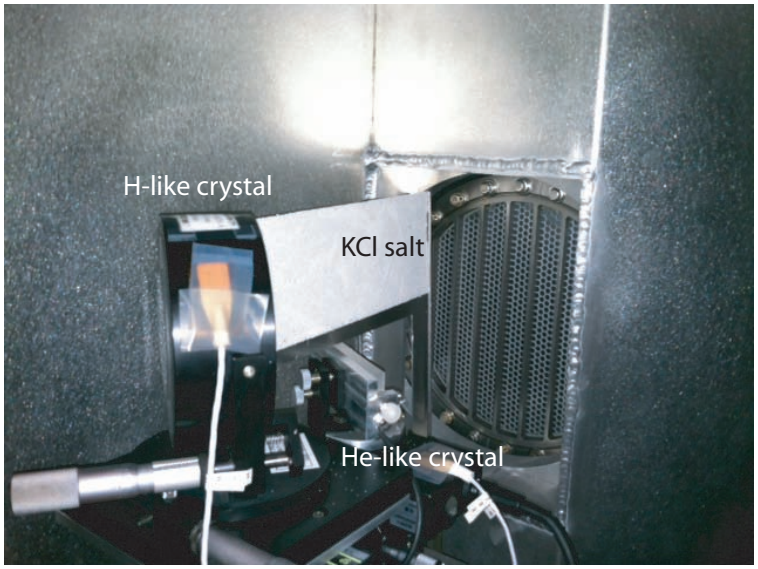

Figure 3-6: Picture of reflection mode KCl holder installed in the HiReX Sr spectrometer.

There is also one final concern with locked modes: whether the locked mode is actually at zero velocity or if there are some rotation changes in the plasma during a locked mode. The ideal mechanism for testing this theory is having an in-situ absolute wavelength calibration and comparing the locked mode zero to the absolute calibration. Since this method is not available at C-Mod, some experiments were performed by varying the current to identify rotation changes during locked modes. Example profiles of locked mode rotation are shown in Figure 3-7. The calibration was performed using the 800 kA discharge as a base case and then the other locked modes are tested against it. Note that there can be variations from zero velocity in the locked mode discharge, since the calibration fits the best fit ellipse to the locked mode phase. Small internal variations in the discharges will still appear as velocity shifts, which is seen in the 800 kA discharge. In Figure 3-7, there are systematic shifts seen in the locked modes, but they are generally within the 5 km/s, and these will be dominated by the rotation changes seen in the plasma. The off-axis peaks in rotation are concerning artifacts that may confound precise rotation results in low rotation plasmas. This effect is mitigated, however, by analyzing highly

rotating plasmas where the shape caused by the calibration is negligible or by looking at changes in rotation, which is what is primarily done in this thesis.

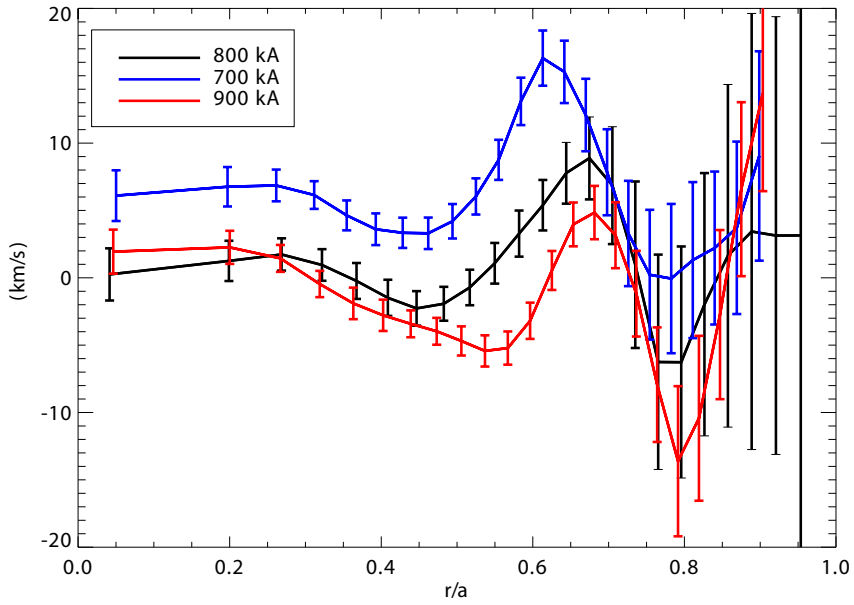

Figure 3-7: Locked mode rotation profiles at three different plasma currents.

2. **Vignetting of lines of sight**

The HiReX Sr spectrometer has a limited window through which X-rays can pass to get to the crystal and, thus, to the detectors. These limiting apertures occur at the 10 inch beryllium window leading to the "racetrack" and the slot into the actual device through the B-port flange. A SolidEdge image of this arrangement is shown in Figure 3-8. If a virtual ray from the detector to the crystal reflects and does not enter the plasma, that position on the detector is considered vignetted. Since different places on the spherical crystal reflect to different locations in the plasma, an emission line can be vignetted on one end and clear on another. This effect can cause spurious rotation or temperature measurements on individual lines if the vignetting is not observed and corrected for properly.

It was found that the size of the slot through B-port was too small to allow both the w and the z lines from argon into the vessel; it is theoretically possible to have both lines clear, but small misalignments could cause one or the other

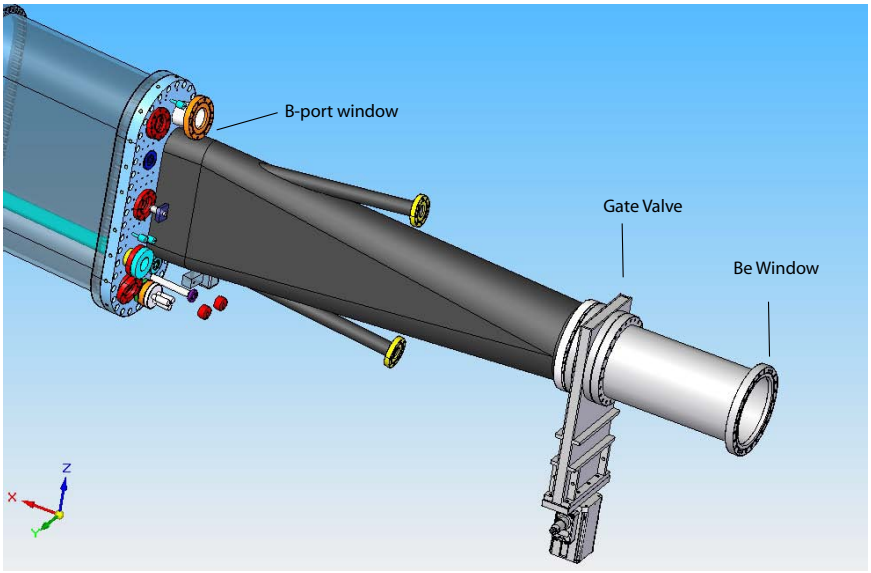

Figure 3-8: Engineering drawing of the racetrack leading to HiReX Sr. The location of the B-port limiting aperture and the Be window are marked.

of the lines to become vignetted. A program that traces the ray positions was used to project all of the lines of sight from the detector onto the plane of the flange. The result of this run is shown in Figure 3-9. The blue points are the projection of lines of sight onto the B-port flange. Note that a large segment of rays lies outside of the green line signifying the slot through the flange. These outlying parts are often located in the colder sections of the plasma and are, therefore, not generating X-rays of the observed wavelength.

In order to align the spectrometer, a laser alignment process was developed. A precision two axis laser is placed inside of the HiReX housing, and positioned on the approximate location of the various lines and on the edges of the crystal. If the laser is able to enter the C-Mod vessel, then the detector position is unvignetted. In general, it is possible to get at least 2-3 lines (often the z, x, and y lines) into the vessel with no vignetting. It is sometimes fortuitously possible to get all four lines with no vignetting as well. During the most recent campaigns, the w line has been run only slightly vignetted.

Recently, physics results from the HiReX Sr device have focused on data from the z-line. This line was chosen due to simpler atomic physics in its modeling, a

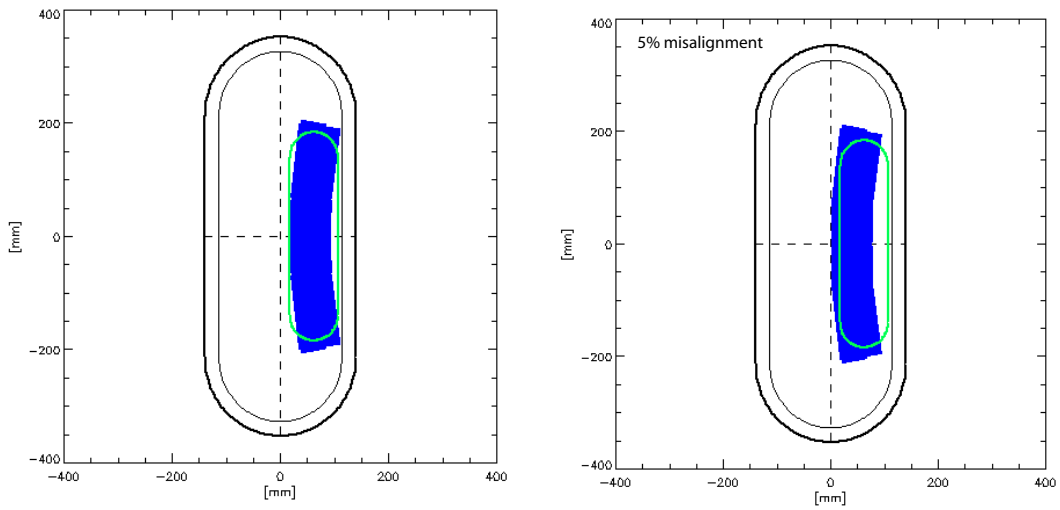

Figure 3-9: (Left) Ray trace of the HiReX Sr lines of sight onto the B-port flange when the spectrometer is perfectly aligned. (Right) Ray trace of the HiReX Sr lines of sight onto the B-port flange with a 5% misalignment. Blue dots correspond to the lines of sight, and the green outline is the slot through B-port.

broader emission spectra, and no high-n satellites. Avoiding vignetting on one line is not a difficult problem and has been achieved for the z-line since 2008.

3. **Flat Field Calibration**

The Pilatus II detectors that are part of the HiReX Sr spectrometers consist of 487×195 pixels. Each pixel is capable of detecting X-rays, but the sensitivity of the pixels can vary. The system is calibrated during construction at the factory for X-ray energies ranging from 3.7 keV through 9.9 keV [59]. It was found that at argon helium-like and hydrogen-like emission energies (3.1-3.3 keV), these calibrations were not always effective, and this effect could create fictitious spatial variations in the profiles from HiReX. This is mostly an issue for spatially up-down asymmetric brightness measurements.

A procedure to recalibrate the detectors was developed. A KCl plate was placed in front of the detector modules and was fluoresced via the use of a copper anode x-ray source at 8 keV and 1.5 mA; this set-up is shown in Figure 3-10. Potassium and chlorine have Kα emissions at 3.3 and 2.6 keV, respectively [60]. Fluorescence is an isotropic process, so the x-ray fluence should decrease

Figure 3-10: Two photographs of the KCl arrangement for the flat field calibration. A Cu anode x-ray tube (not shown) is used to cause nearly isotropic fluorescence from the KCl plate.

approximately with the square of the distance, and there will be a fairly uniform cosine dependence on the detector. Since the primary goal of this calibration is removing the pixel to pixel variations, large (submodule) length scale variations are acceptable. It was found that the flat field decay was of order 10% over a submodule scale length, so it was acceptable to use this method.

It would be ideal to use a dedicated facility in order to calibrate the Pilatus II modules. Specifically, a design with monochromatic KCl fluorescence at a large distance with more intense x-ray source would be ideal. Due to the absence of such a facility at Alcator C-Mod and the fragility of the Pilatus II modules making their transport non-ideal, this superior calibration was not attempted; thus, the error on the flat-field calibration is higher than physically achievable.

3.1.2 HiReX Jr

The HiReX Jr spectrometer [61] is the predecessor of the HiReX Sr spectrometer. It is a one channel core viewing spectrometer constructed to measure ion temperature, electron temperature, and ion rotation at the core of the plasma. HiReX Jr uses a von Hamos [62] geometry cylindrically bent crystal as a dispersive element to measure H-like argon emission in the C-Mod plasma. Prior to the development of the HiReX Sr spectrometer, it was the primary rotation diagnostic on Alcator. The detector used for HiReX Jr is a 20% ethane and 80% krypton filled single proportional counter and delay line, where an X-ray ionizes the gas causing a charge on the wire. This detector is susceptible to noise pickup from RF systems, making it non-ideal for a variety of experiments on Alcator.

Despite the development of HiReX Sr, HiReX Jr has still been operated for a variety of reasons. It has an absolute calibration, has not been observed to drift in velocity space over time, and a completely tangential view observing the rotation directly (unlike HiReX Sr which has a 7° angle view toward the toroidal rotation direction). This allows calibrating HiReX Sr against HiReX Jr when no applicable locked mode can be found.

3.1.3 Beam Based Diagnostics

Alcator C-Mod has a diagnostic neutral beam installed on the device for support of the Charge Exchange and Motional Stark Effect diagnostics [63]. It is rated to 50 kV and 6 A of hydrogen beam with a current density of 70 mA/cm^2. The beam interacts with background impurities in the plasma producing a well-localized, known time emission, often at convenient emission energies. For example, the core charge exchange system measures ion temperature at Alcator C-Mod by analyzing emission from the 5292 Å line from the n=7-8 transition in C^{5+}. This emission is in the visible range so it can use light fibers for transmission, therefore the detection mechanism is much simpler than that for X-rays or UV. The localization, time dependence, and convenient emission spectra makes charge exchange a commonly used diagnostic method on a variety of machines [64].

An important diagnostic for the measurement of rotation in the edge of the plasma is the edge Charge Exchange Recombination System (often called CHRS, CXRS, or CHERS) [65]. This system uses the emission from boron impurities in the plasma as excited by the diagnostic neutral beam. The emission is from B^{4+} n=7-6 4944.67 Å emission, from recombined intrinsic B^{5+}. This system can measure poloidal and toroidal rotation in the edge, as well as ion temperature and boron concentration. It is often used to infer the radial electric field in the edge, particularly during H-modes and I-modes.

3.1.4 Non-rotation Diagnostics

Despite the rotation diagnostics being the most often used in this work, there is an enormous array of plasma diagnostics that is required for both getting data from the plasma and for the operation of the tokamak. These diagnostics include magnetics, Electron Cyclotron Emission, Thomson, Motional Stark Effect, and phase contrast imaging. Four particularly important diagnostics in this work are given short descriptions below.

Thomson Scattering

The Thomson scattering systems have been in existence for many years on a variety of machines. Thomson scattering [66] uses a series of pulsed Nd:YAG lasers which fire during the discharge. The photons scatter off free electrons in the plasma and their intensity and spread can provide information about the electron density (n_e) and temperature (T_e). Given the importance of profiles of these quantities, Thomson is a diagnostic that sees wide use in nearly all C-Mod discharges. The Thomson system is required for profiles and profile scale length measurements, and the data from this device are used in nearly every section of this thesis.

Bolometry

Alcator C-Mod has a spatially spanning foil and diode system to measure the total energy being emitted from the plasma [67]. Bolometry is used to measure the total radiated power from the plasma. This is important to account properly for the power handling of the materials in the plasma environment. The devices function by having small foils of material (or more recently silicon photodiodes) that are precisely calibrated and see lines of sight through the plasma. The foils/photodiodes precisely measure the amount of energy that is deposited on them, and, thus, show how much energy was emitted in a wide electromagnetic range. In this work, bolometer emissivity data are most often used as an input to the TRANSP (see Section 3.2.1) code, where it is required for proper accounting of the power in the plasma and, thus, temperature, transport, and resistivity.

Motional Stark Effect

The Motional Stark Effect (MSE) system is designed to measure the pitch of the magnetic field in the plasma and to infer the q-profile. Measured q-profiles are highly sought after data due to their ability to improve the EFIT reconstructions that are important to nearly every single diagnostic that measures profiles in a tokamak environment. It is also important for the physics that q-profiles are expected to affect,

such as turbulence and sawtooth instabilities.

The MSE system only functions with the presence of the diagnostic neutral beam. The beam emits neutral ions at a high velocity into the plasma, which then experience an effective electric field via the $\mathbf{v} \times \mathbf{B}$ force. The electric field causes the energy levels in the atom to split based on their polarization with respect to the electric field and thus creates multiple transitions where there used to be one. The energy spread in these emission lines can be used to calculate the electric field experienced via the equation $\Delta E_n = 3nkE/(Ze/4\pi\epsilon_0 a_0^2)R_y$, where ΔE_n is the energy spread, n is the principal quantum number, k is an integer from 0 to $\pm$(n-1), a_0 is the Bohr radius, and R_y is the Rydberg energy.

Phase Contrast Interferometry

Phase contrast interferometry (PCI) is one of the major diagnostics for measuring turbulence in a plasma. PCI splits a laser beam into two beams which are then recombined after one of the branches passes through the plasma. The plasma shifts the phase of the beam as follows

$$\delta\phi = -\frac{\omega}{2cn_c}\int n_e dl \tag{3.4}$$

where n_c is the plasma cutoff density, ω is the laser frequency, n_e is the plasma density, and l is the path length. Combining the beams of the laser on top of each other and out of phase, it is possible to measure purely the density fluctuations in the plasma by analyzing the interference spectrum. The PCI system on C-Mod has several chords going through the core region of the plasma. These chords and interference spectra allow the system to quantify turbulence in k and ω space providing extremely important data on the type of turbulence in the plasma core.

3.2 Analysis Tools

A variety of codes has been used in this work and deserves special mention. They are theoretical simulations rather than diagnostic tools, but, given their wide scale use, it is more applicable to discuss them in this section.

3.2.1 TRANSP

The TRANSP code is a time-dependent tokamak transport code developed at PPPL. This code is a remote-run power balance code which deduces plasma transport and particle, momentum, and energy fluxes. The TRANSP code has built-in modules for calculating neutral beam deposition, RF and Lower Hybrid wave physics, and neoclassical transport. There is no one reference for the simulation code, but the various models and equations used are described in more detail in [68, 69, 70], and an example of the use of the TRANSP code for TFTR is shown in [71].

3.2.2 GS2

GS2 [72, 73] is a gyrokinetic modeling code for low frequency turbulence in a tokamak. This code is run on the LOKI supercomputing cluster at the MIT PSFC. GS2 is a fast parallelizable code which can take inputs from a variety of codes in order to generate quickly instability spectra. It can notably take a TRANSP input file to generate the full magnetic geometry for the simulation. It is also possible to create GS2 runs without using TRANSP by inputting plasma parameters and profiles manually.

GS2 solves Vlasov's equation and Maxwell's equation in a guiding center approximation, averaging over the gyro-radius. These equations assume a slowly changing equilibrium and $\rho/L \sim \delta f/f$. In this work, it is run mostly as a local, linear simulation, ignoring non-linear coupling. The linear simulations calculate the most unstable mode over a wide range of plasma radii.

3.2.3 GYRO

The GYRO code is another gyrokinetic modeling code. It is managed by General Atomics and was designed to be a non-linear simulation. It can also take TRANSP input files similar to GS2, and it is more effective at non-linear and global simulations. GYRO has recently been changed to allow the use of rotation profiles for E×B shear turbulence modification. Generally, GYRO is a widely used and benchmarked simulation with a wide variety of base cases [74].

The GYRO code is a more time consuming code to run than the GS2 code. Nevertheless, various simulations are performed because of its wide use and simple mechanism for setting up non-linear global runs. Furthermore, GYRO and GS2 can be compared to benchmark the codes against each other and note the similarities and differences between the codes. Generally, linear simulations are performed in this work.

3.3 Summary

The various diagnostic and widely available analysis tools used in this work have been presented. The primary focus of this research has been the rotation profile generating diagnostic, HiReX Sr. Therefore, the various upgrades of and concerns about HiReX Sr have been presented. Alternate devices and codes are also presented in this section, with short overviews highlighting their impact on the work presented in this thesis. Overall, these tools and diagnostics make an Alcator C-Mod plasma a well characterized environment, which allows making in depth analyses of the rotation and transport during various discharges.

Chapter 4

Rotation Reversals

Rotation reversals were first identified [75, 76, 77, 78] on the TCV device in Switzerland. The reversal phenomenon is that an L-mode plasma can spontaneously reverse rotation direction when the density, magnetic field, current, or plasma shape is changed slightly. The most of the plasma profiles remain unchanged except for the rotation magnitude, magnitude of the density, and slight variations in the electron and ion temperature profiles. These rotation reversals have been studied in detail at Alcator C-Mod [3, 79].

4.1 Rotation Reversal Basics

It was found that rotation reversals in a plasma can occur through changes in electron density, magnetic field, and plasma current [3], though density is the most commonly used parameter for experiments. As seen in Figure 4-1, when the density transitions above a critical value, the rotation spontaneously changes direction. This transition occurs with a hysteresis dependence and, thus, appears to be a bifurcation in the plasma itself (akin to the H-mode transition).

The location of rotation reversal in density and current space is shown in Figure 4-2. The best fit equation to the data is $n_e B^{0.6}/I_p = 2.8$ or $n_e q_{95} = 3.5$ (at B=5.4T), where density is measured in 10^{20} m^{-3}, magnetic field in Tesla, and current in MA. These equations are reminiscent of the equations describing the Linear Ohmic Con-

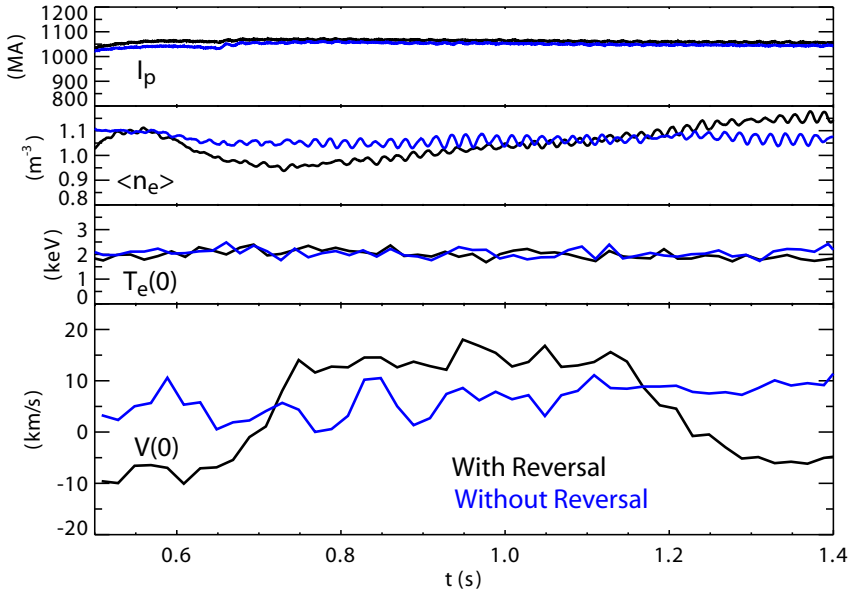

Figure 4-1: Two plasma traces of current, averaged density, core temperature, and core velocity taken at 5.4 T, one showing two rotation reversals (black) and the other showing no rotation reversals (blue). The only difference between these two discharges is the density trace. The early rise of density occurs right after the end of the current rise and may still be in the current relaxation phase of the discharge, confounding results.

finement (LOC or Neo-Alcator Scaling [80]) to Saturated Ohmic Confinement (SOC or the ITER-89 scaling [7]) changeover. It is actually seen that when the rotation reverses direction, the energy confinement in the plasma changes as well, as seen in Figure 4-3. It is conjectured that the rotation reversal is, in fact, the most telling sign of the LOC to SOC transition.

The rotation profiles of these transitions are shown in Figure 4-4. It is observed that the rotation primarily changes within the core of the plasma and remains fixed at the edge. This edge location is near the $q = 3/2$ surface in the plasma, and it is seen to vary at different currents, which moves the position of the $q = 3/2$ surface.

Overall, reversals provide an interesting case of rotation changes with no external momentum input. Given the seeming correlation of the rotation reversal with the energy confinement time transition, the rotation reversal is extremely important to understand from a reactor operation standpoint where the energy confinement is critical. Furthermore, the pinning near the $q = 3/2$ surface is a particularly strange

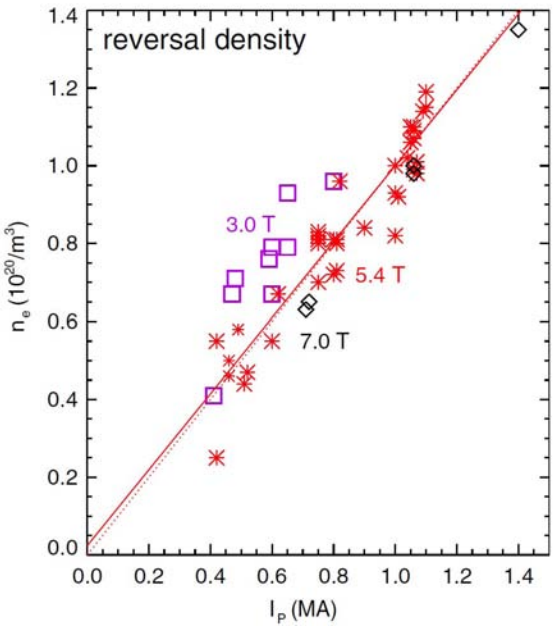

Figure 4-2: Rotation reversal position as a function of current and plasma density and separated by magnetic field. Figure from [3].

phenomenon that can only be explained through the use of a residual stress term since the diffusive and convective terms will not be able to recreate inverted profiles inside a fixed rotation location.

4.2 Turbulence Changes during Reversals

It was observed on the PCI system that during a rotation reversal there is a marked change in the density fluctuations in the plasma. A characteristic comparison of the PCI spectra before and after a reversal is shown in Figure 4-5. After the transition, there is increased intensity at constant $v_{ph} = \omega/k \simeq 5$ km/s, which are referred to as "turbulent wings". The wings only appear in the low confinement, low collisionality regime. These observations suggest that during the rotation reversal there is a significant change in the turbulence in the plasma.

In order to understand these turbulence changes, gyrokinetic simulations during the two phases of the rotation reversal were analyzed. Full profiles of the plasma parameters are shown in Figure 4-6, where it is seen that most parameters do not

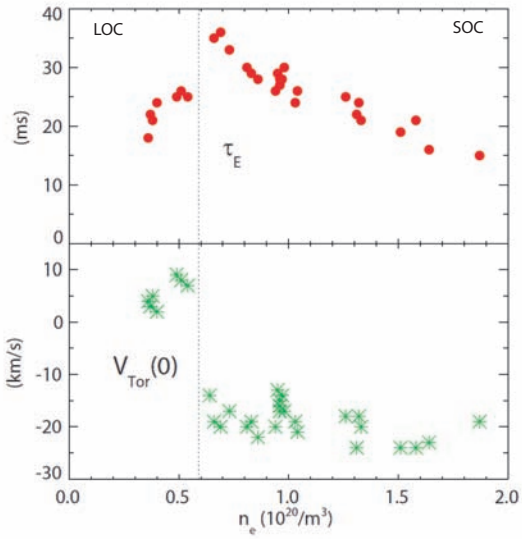

Figure 4-3: Rotation reversal position plotted with the energy confinement time to highlight the relation of the rotation reversals to the LOC/SOC changeover. Figure from [3].

change significantly across the reversal except for the rotation, magnitude of density, and the T_e/T_i ratio. The GYRO code (see Section 3.2.3) in linear operation mode was used to identify the dominant instability type at various times and radii in the plasma for both forward (LOC) and reverse (SOC) rotation. These simulations were limited to $k_y\rho_s$= 0.25-0.75, in order to analyze only long wavelength turbulence which generally drive more transport than the short wavelength turbulence. The selected range still captures both ITG and long wavelength TEM turbulence. An example spectra at r/a=0.475 of the growth rate and frequency of the modes versus $k_y\rho_s$ is shown in Figure 4-7 for the rotation reversal discharge. At t=1.0 s, the mode structure is of mixed stability (part of it is in the ion diamagnetic direction and part is in the electron diamagnetic direction). At 1.4 s, however, the mode structure is solidly in the ion direction. This suggests that at this radius the plasma transitions from a mixed mode case to a solidly ITG case after the transition to SOC. These simulations were run over a wide space of parameters to test their sensitivities to the common turbulence driving factors a/L$_n$ and a/L$_{T_i}$. The first parameter scan was performed on the previously shown rotation reversal discharge with grids of 15x15 in a/L$_n$ and a/L$_{T_i}$ space. The two characteristic times chosen were 1.0 s and 1.4 s

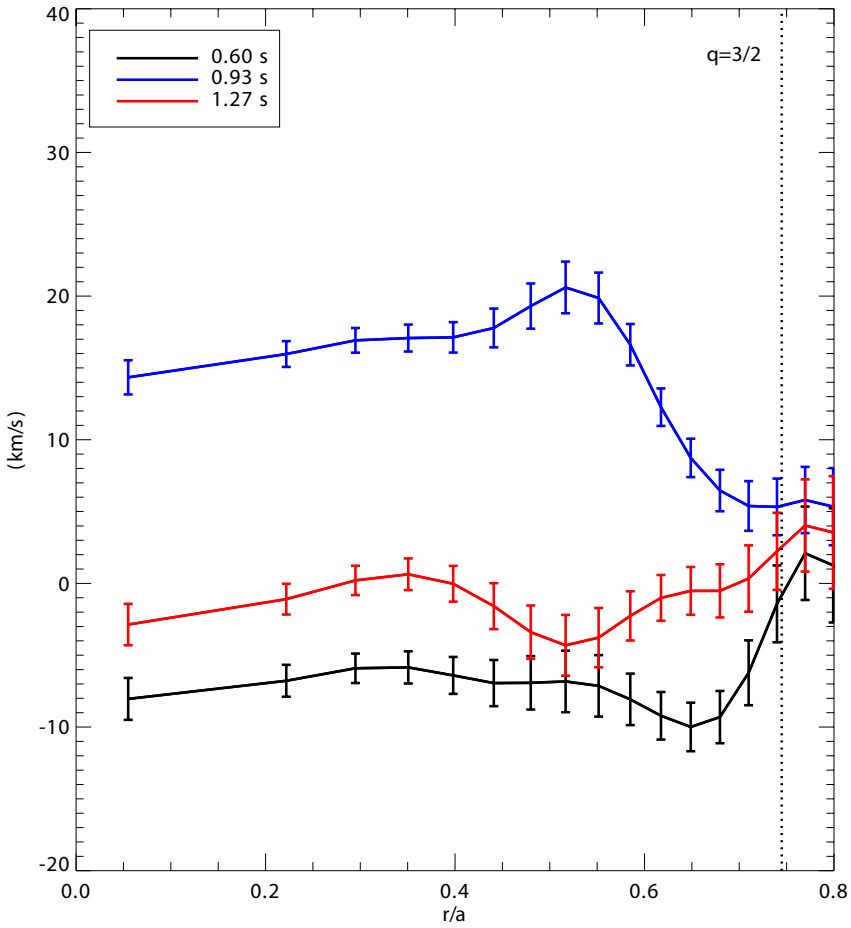

Figure 4-4: Rotation profiles versus r/a at three characteristic time points during a discharge with two rotation reversals (shown in figure 4-1). The position of $q = 3/2$ is overplotted as a dashed line in this figure.

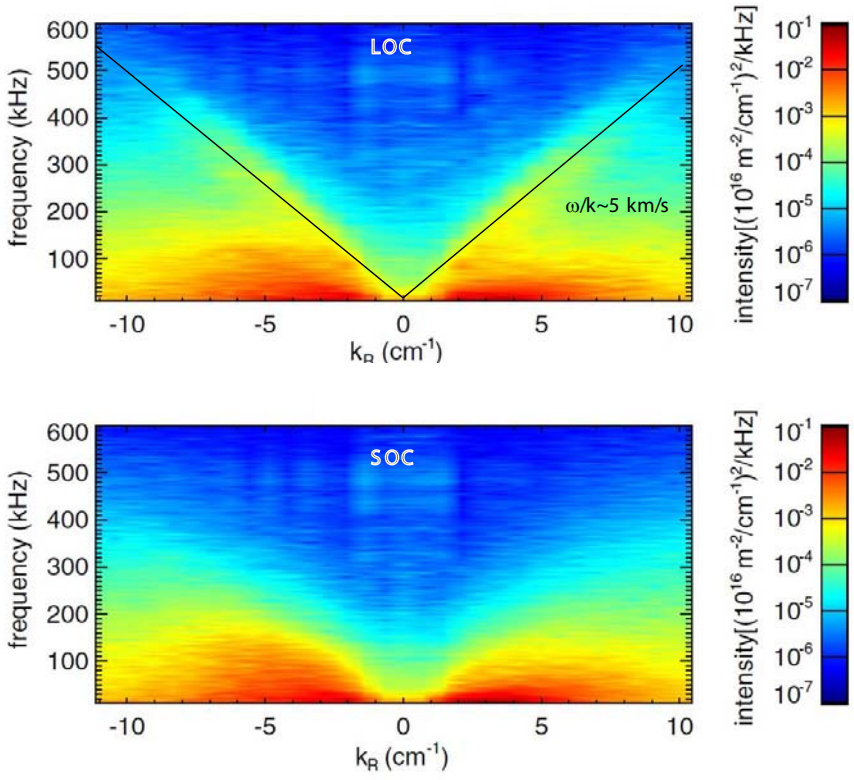

Figure 4-5: PCI density fluctuations before and after a rotation reversal highlighting the appearance of turbulent "wings" in the LOC regime. Black lines highlight areas of increased turbulence in the LOC regime. Original figure from [3].

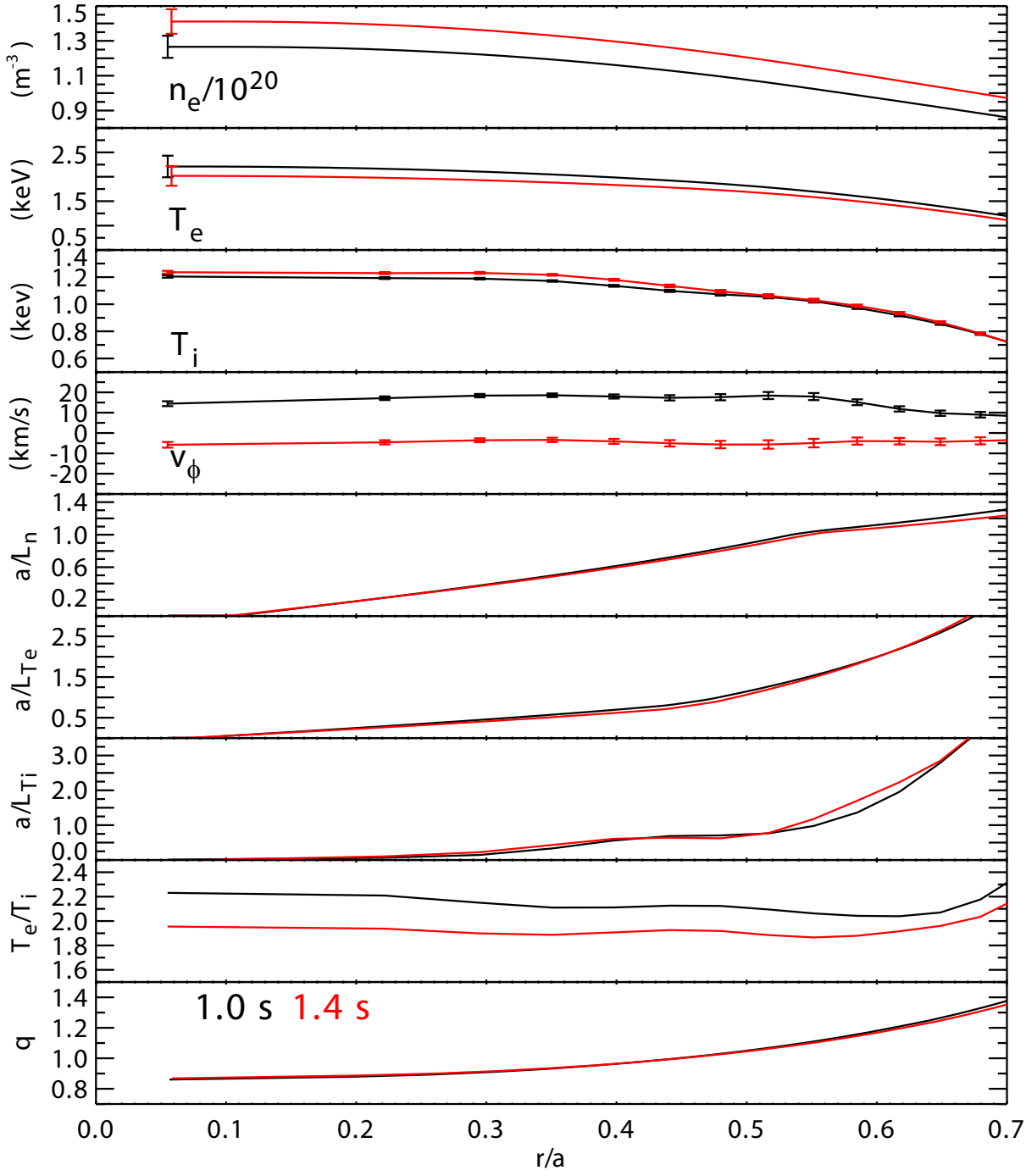

Figure 4-6: Plots of profiles of electron density, electron temperature, ion temperature, and plasma velocity, as well as the various drive terms for turbulent modes for two characteristic times in a rotation reversal discharge (1.0 s and 1.4 s). Black curves are for co-current rotating plasmas and red curves are for counter-current. Characteristic statistical error bars are shown in the top four graphs.

and the profiles were averaged over 50 ms for smoothed data. The same gyrokinetic simulations were run on this discharge with the density scanned by a factor of two in both the low and high direction: this effectively scans the collisionality in the plasma since the density scale length is not changed. These simulations were performed at three radial positions: r/a=0.475, 0.600, and 0.700. The results of the simulations are shown in six sets of figures: 4-8 (1.0 s, r/a=0.475), 4-11 (1.4 s, r/a=0.475), 4-9 (1.0 s, r/a=0.600), 4-12 (1.4 s, r/a=0.600), 4-10 ((1.0 s, r/a=0.700), and 4-13 (1.4 s, r/a=0.700). In the referenced figures, the crosses represent the experimental data and the black lines represent the transition from electron directed to ion directed turbulence, commonly considered the ITG/TEM transition. A short discussion of the ITG and TEM microturbulent modes is provided in Appendix D. Thin black lines represent contours of equal linear growth rate of the most unstable mode, so these figures show the dependencies of the dominant modes' linear growth rate to turbulence driving parameters.

It is seen from the linear stability profiles that in the 1.0 s rotation case, the experimental profiles place the most unstable mode on the cusp of the ITG/TEM threshold. In the 1.4 s case, however, the experimental data are significantly more in the ITG turbulence regime (dependent on a/L_{T_i} and in the ion diamagnetic direction). This is a confirmation of the previous assertion that the rotation reversal is the marker for the transition from TEM to ITG scenarios, where the PCI wings only appear in the TEM regime. Furthermore, increasing the density causes a gradual transition from TEM to the ITG dominated plasmas. This is caused by the collisionality preventing electrons from staying on complete trapped orbits, thus decreasing the drive for the TEM. In all of the doubled density cases, the turbulence is solidly in the ITG dominated regime. This sensitivity suggests that the density dependence can cause a transition from the TEM to ITG dominated scenarios, but given that the density had to be increased by a factor of two to achieve this, these linear simulations are not capable of reproducing the exact density behavior. This implies that the profiles are, in fact, driving the transition from electron to ion directed modes. The only profile-wide effect (besides rotation) that changes significantly between the two

reversal cases is the ratio of electron to ion temperature, so this change is the most likely explanation for the changes in the plasma turbulence.

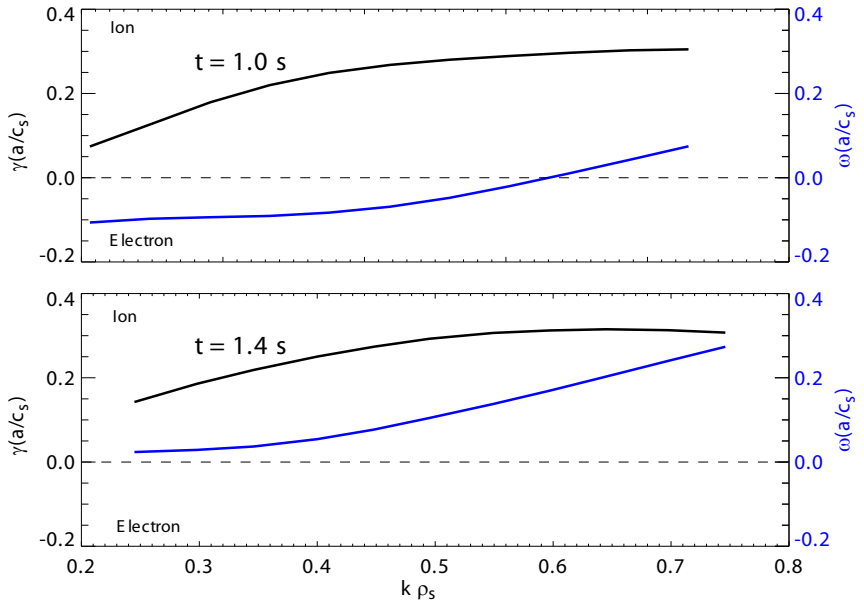

Figure 4-7: GYRO linear simulation at r/a=0.700 at t = 1.0 s and t = 1.4 s. This shows the fastest growing mode normalized growth rate and frequency as a function of normalized mode wavelength.

In order to identify the type of turbulence that is being seen in these plasmas, base cases of the three radial positions were run with scans performed in a/L_{T_e} and a/L_{T_i} instead of a/L_n and a/L_{T_i}. Since density was not observed to be the major driver of the turbulence in the simulation, these scans were not performed with the previous artificial density variations. The results of these simulations at t= 1.0 s and t = 1.4 s are shown in the following three sets of figures: 4-14 (r/a = 0.475), 4-15 (r/a = 0.600), and 4-16 (r/a = 0.700). Once in the ion direction, in all of the sensitivity studies, the instability depends primarily on the a/L_{T_i} term. In the electron direction, the most unstable mode depends strongly on a/L_n at all radii and weakly on a/L_{T_e}, with the outer radii depending slightly on a/L_{T_e} and the inner channels completely independent of it. These dependencies imply that the main turbulence modes are transferring from density gradient driven TEM to ITG modes during the rotation reversal.

Given that one of the major features of the LOC to SOC transition is the change

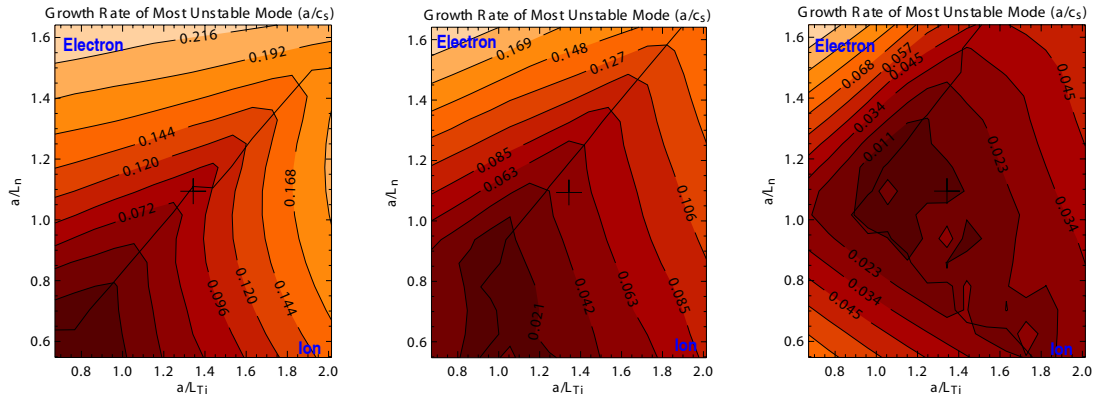

Figure 4-8: GYRO sensitivity at 1.0 second at r/a=0.475 at half the real density (left), actual density (middle), and twice the density (right).

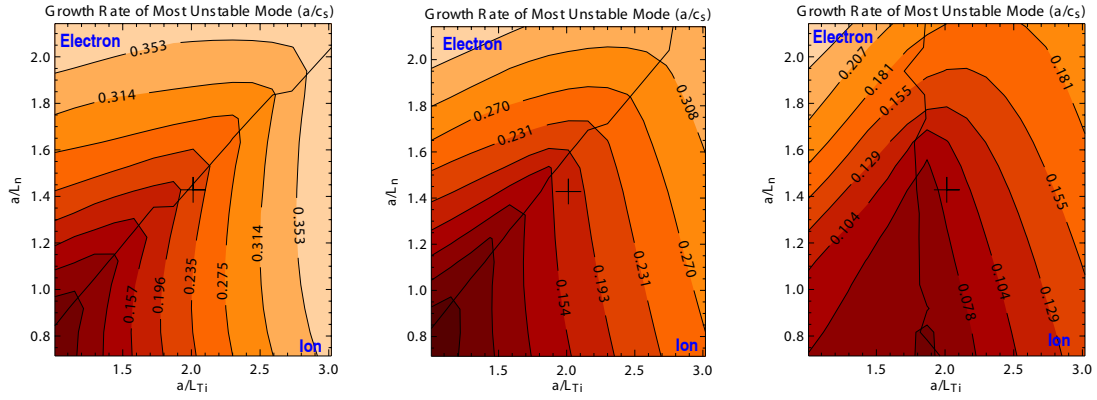

Figure 4-9: GYRO sensitivity at 1.0 second at r/a=0.6 at half the real density (left), actual density (middle), and twice the density (right).

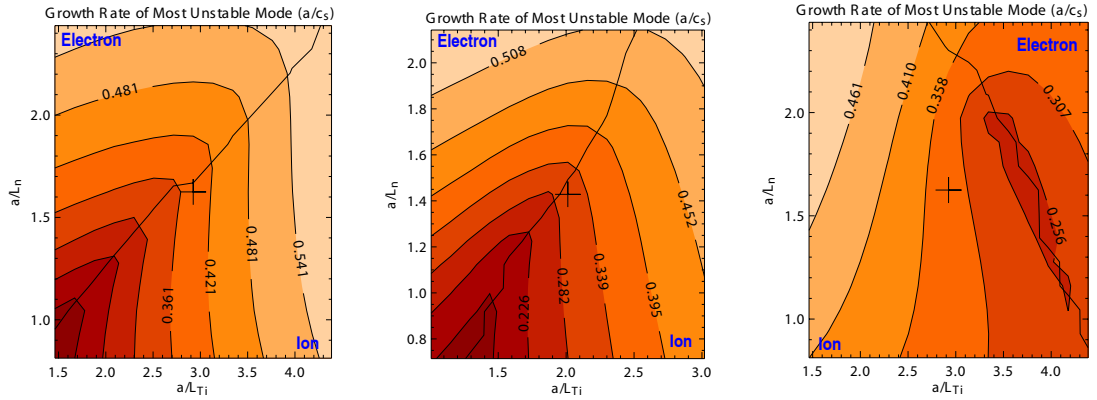

Figure 4-10: GYRO sensitivity at 1.0 second at r/a=0.7 at half the real density (left), actual density (middle), and twice the density (right).

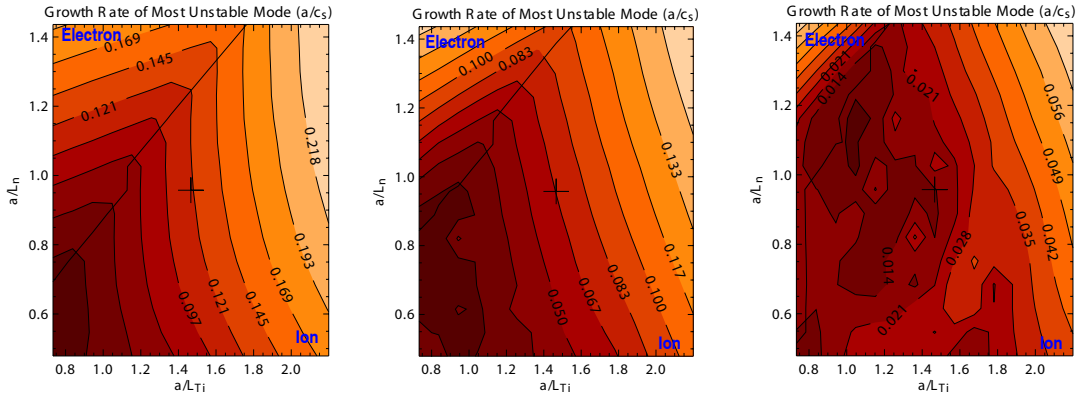

Figure 4-11: GYRO sensitivity at 1.4 seconds at r/a=0.475 at half the real density (left), actual density (middle), and twice the density (right).

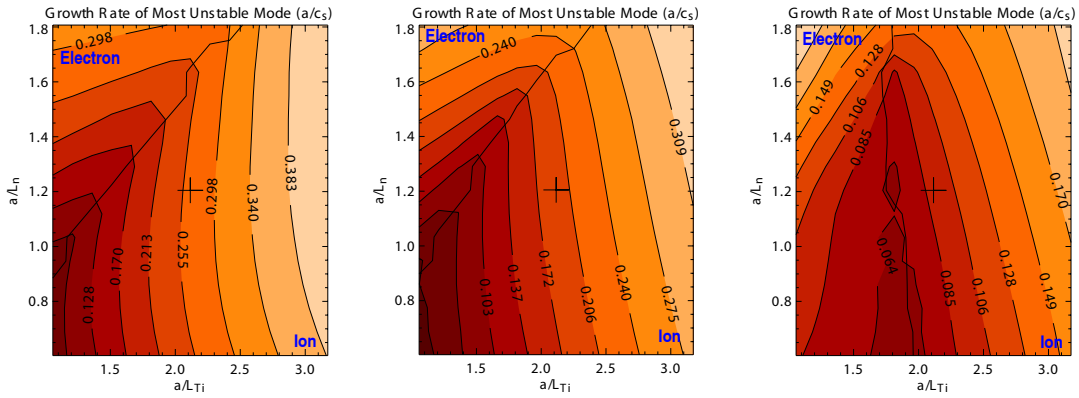

Figure 4-12: GYRO sensitivity at 1.4 seconds at r/a=0.6 at half the real density (left), actual density (middle), and twice the density (right).

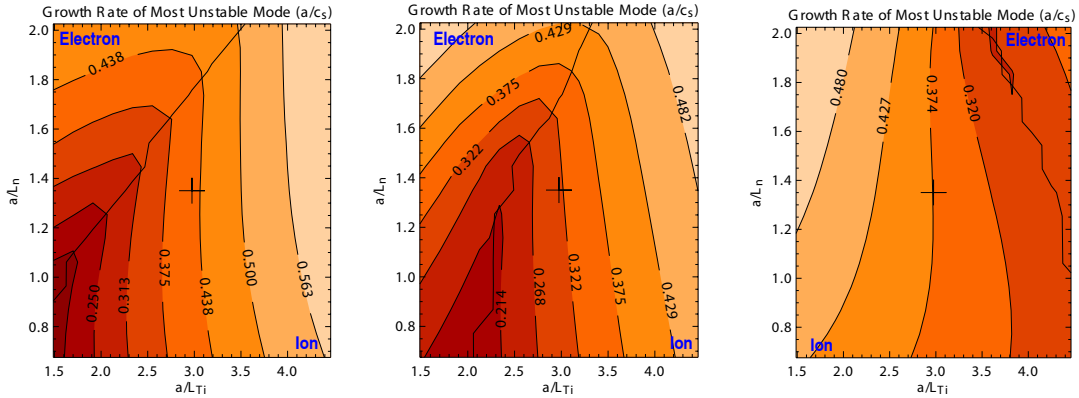

Figure 4-13: GYRO sensitivity at 1.4 seconds at r/a=0.7 at half the real density (left), actual density (middle), and twice the density (right).

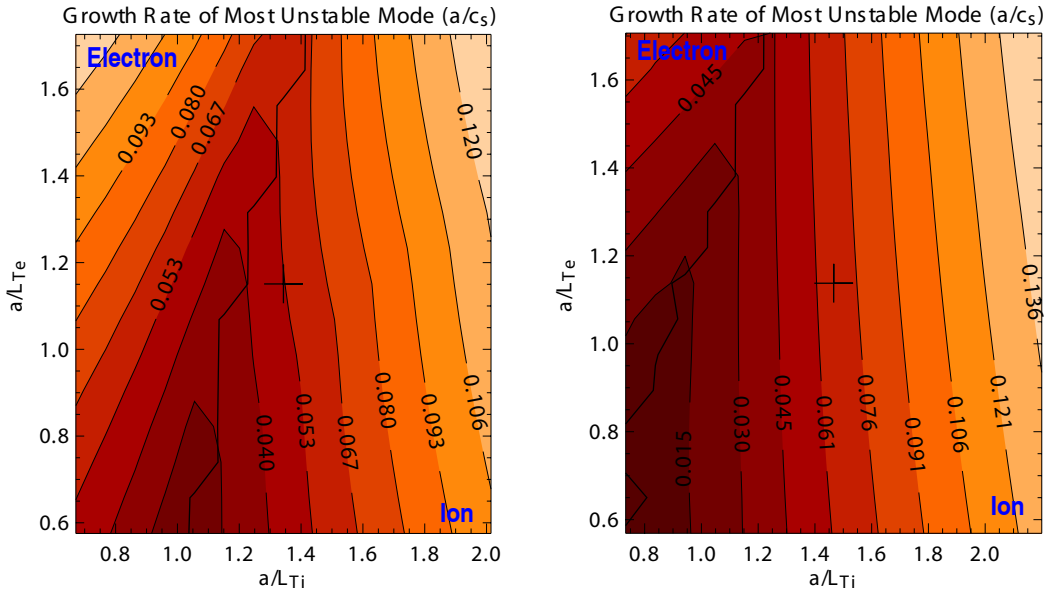

Figure 4-14: GYRO sensitivity at r/a=0.475 at 1.0 s (left) and 1.4 s (right)

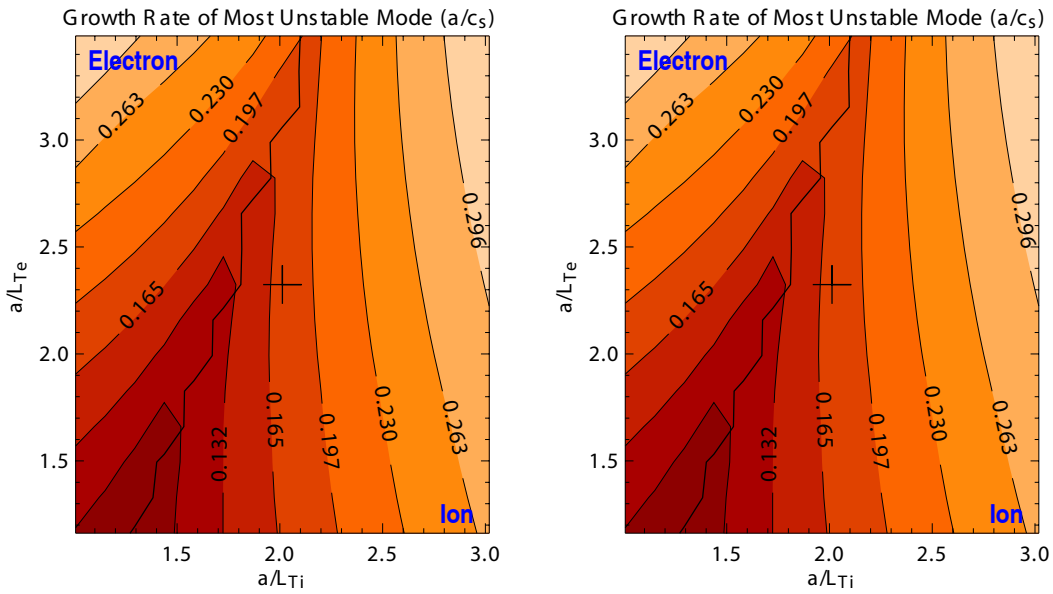

Figure 4-15: GYRO sensitivity at r/a=0.6 at 1.0 s (left) and 1.4 s (right)

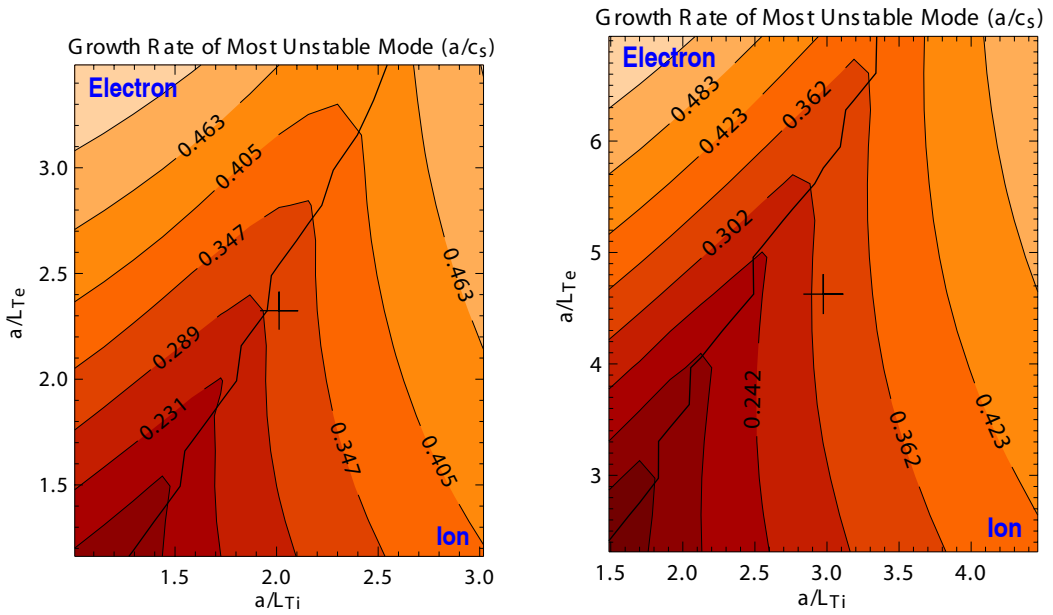

Figure 4-16: GYRO sensitivity at r/a=0.7 at 1.0 s (left) and 1.4 s (right)

of the T_e/T_i ratio as seen in Figure 4-6, two further simulations with a 50% increase in the electron temperature and a 33% decrease in the ion temperature were perofmed. Thes simulations at t=1.4s and r/a=0.7 are shown in Figure 4-17. The propagation direction of the most unstable mode is marginally in the ion diamagnetic direction in both cases, while in the base case (4-13) the most unstable mode is strongly in the ion diamagnetic direction.

In order to benchmark the GYRO simulations, a comparison of the most unstable modes was run in GS2 (see Section 3.2.2) as well. The characteristic linear instability plots for the reversal discharge in both the counter-current and co-current rotation case are shown in Figure 4-18. It is seen that the linear instability plots are nearly identical in the two cases. This is in marked contrast to the GYRO simulations where changes were observed at multiple radii of the direction of the modes.

Since it is generally considered that the density, magnetic field, and current are the drivers for the rotation reversal transitions, those driving parameters were scanned with GS2. In theory, the results from GS2 and GYRO should be very similar, since they are both being run in linear mode and with the same profiles. There have been observations of differences between the codes at low collisionality in the past, though.

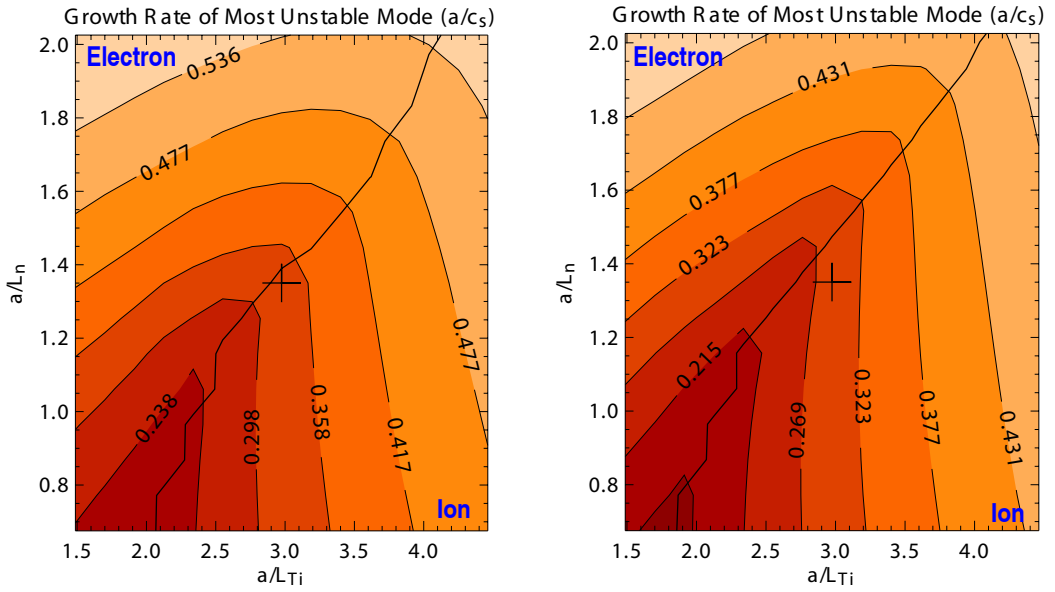

Figure 4-17: GYRO sensitivity at r/a=0.7 at 1.4 s with a 50% increase in electron temperature (left) and 33% decrease in ion temperature (right).

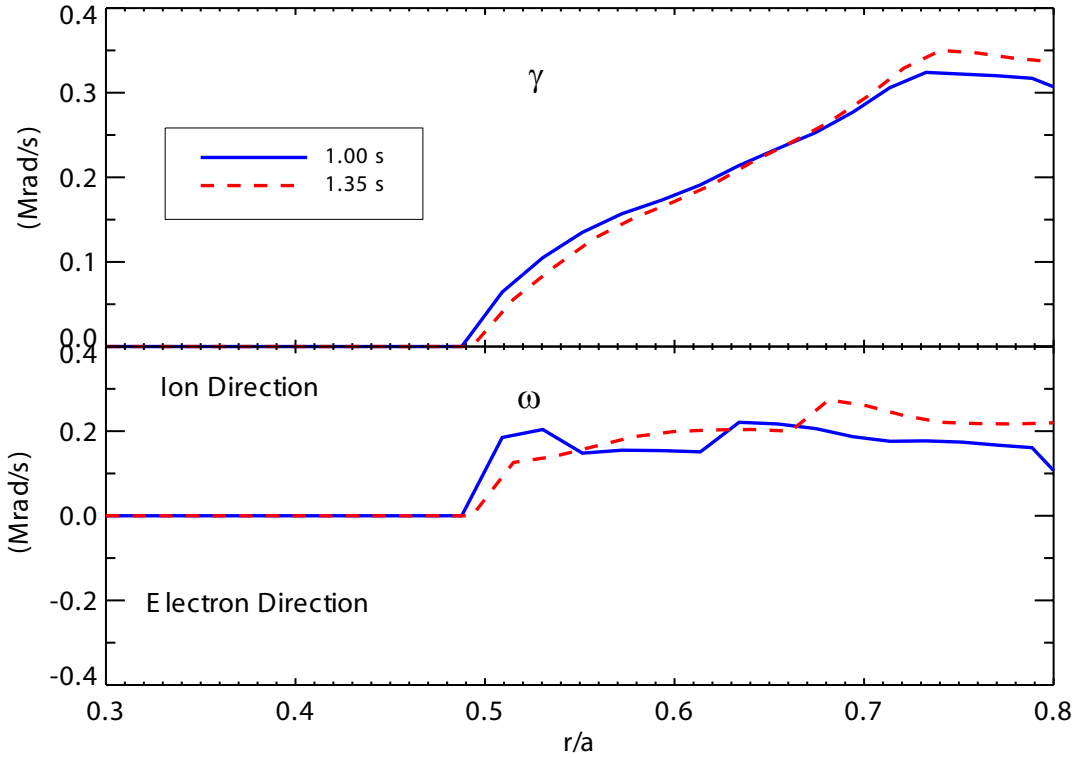

Figure 4-18: Linear GS2 calculations of the most unstable mode versus radius in a discharge with two rotation reversals. Top figure is for growth rate and bottom portrays frequency.

Therefore, GS2 sensitivity scans were run at r/a = 0.54 (a characteristic position which is within the radii that were analyzed with GYRO) with the scanned parameters a/L_n (Figure 4-19), ν_{ei} (Figure 4-20), T_e/T_i (Figure 4-21), and magnetic field (No effect, so no figure shown). For each of these scans, the discharge is analyzed at t=1.00s and t=1.35s, which are after the first reversal and after the second transition, respectively. Note that there are slight changes in the experimental data simulated by GS2 and GYRO which arise because of the method of extracting and smoothing data used by each of these codes. The differences are of order 10% and, thus, should not change the conclusions of the simulations.

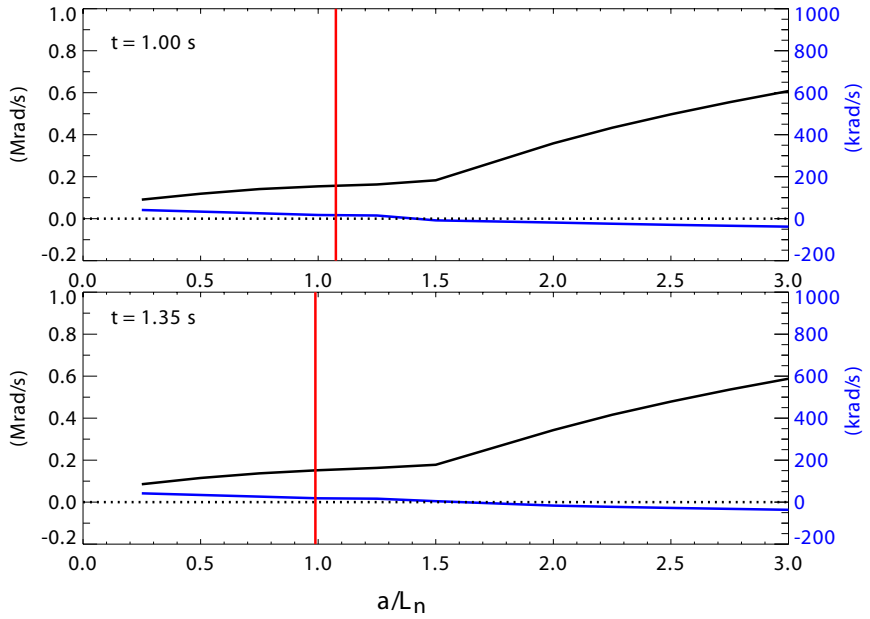

Figure 4-19: Linear GS2 sensitivity studies of density gradient scale length at two times in the rotation reversal discharge. Red lines correspond to experimental data.

The linear stability shows that there is a strong dependence on the density scale length. It is even seen that there is a transition of the modes from ion directed modes to electron directed modes as a/L_n changes. This is similar to what was observed with GYRO, but it is seen that the experimental data do not cross the transition threshold as a function of a/L_n in this code. The collisionality does not cause a transition, but it is seen that there are changes in the modes as expected. Furthermore, there was no observed dependence of the most unstable modes on the magnetic field.

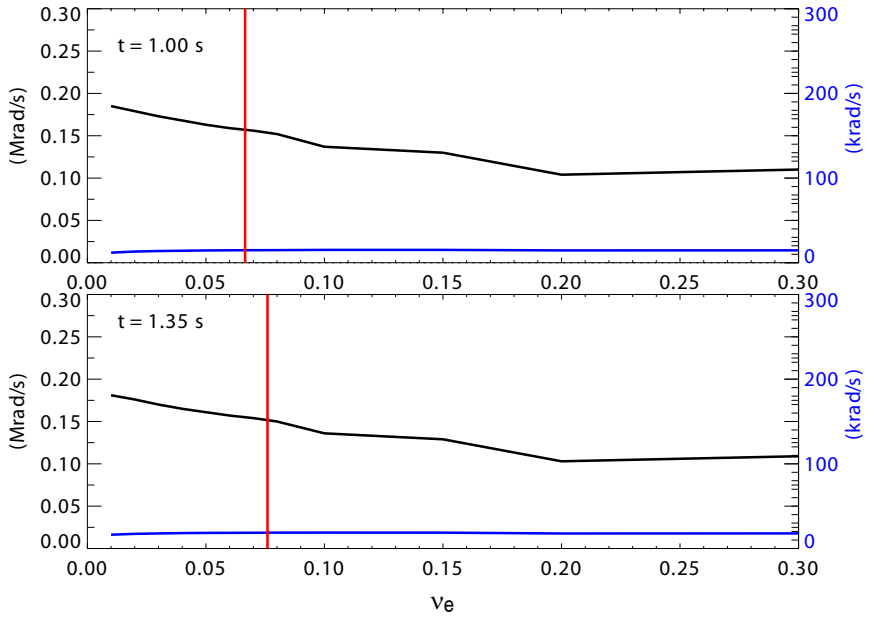

Figure 4-20: Linear GS2 sensitivity studies of electron collisionality at two times in the rotation reversal discharge. Red lines correspond to experimental data.

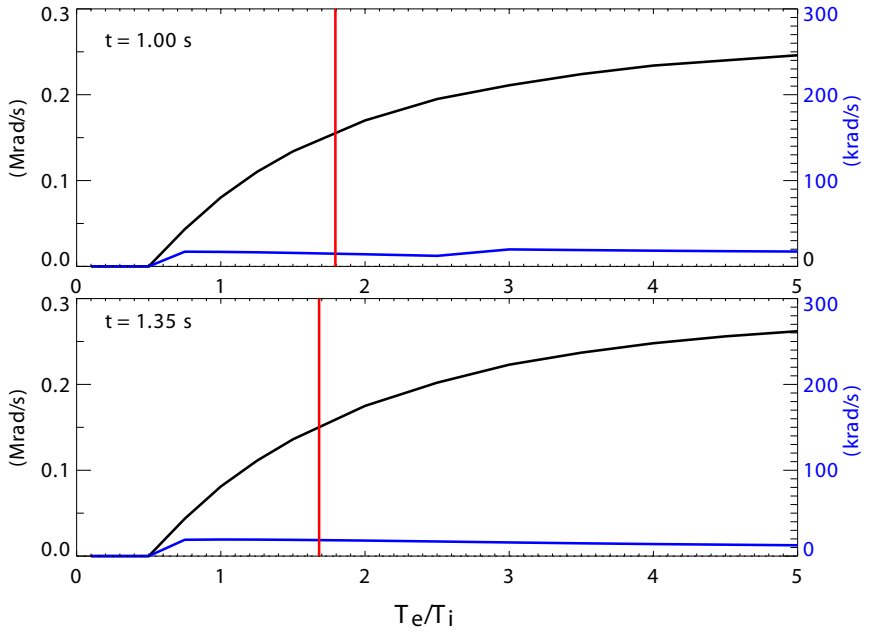

Figure 4-21: Linear GS2 sensitivity studies of electron to ion temperature ratio at two times in the rotation reversal discharge. Red lines correspond to experimental data.

While the GYRO simulations showed a transition of the modes from TEM to ITG regime occurring from the rotation reversal due to the T_e/T_i changes, the GS2 simulation does not reproduce the same behavior. They both did, however, find that if a/L_n was raised significantly, the mode would transition to the electron direction. This difference may be due to the low collisionality differences in the codes, and should be explored in more detail in the future as validation for the GS2 and GYRO codes.

In summary, the GYRO simulations showed that there exists a TEM to ITG dominated mode change as the plasma reverses direction during an Ohmic rotation reversal. The GS2 simulations showed qualitatively similar growth rate versus normalized frequency relations, but they did not show the same reversal behavior as a function of T_e/T_i, although more radial simulations may be necessary to reproduce the same behavior. Both GS2 and GYRO imply that the transition from electron to ion directed unstable modes is possible in the area (in a/L_n space) of the discharges, so it is concluded that the linear simulations support the previous assertions about the relation of the rotation reversal, turbulence, and the LOC/SOC transition.

4.3 Source Profiles in a Reversal

The only way for the rotation to reverse direction due to these profile transitions is from convection or residual stress switching sign. These changes cannot be explained by simple diffusion with edge changes, since they often appear to be core localized. Furthermore, these small changes in the profiles cannot explain the rotation behavior from neoclassical and sub-neoclassical theory. This leads to the use of the "Toy Model" to calculate the shape of the source profile required to explain the rotation. The only effect that can cause a reversals of the rotation as seen is the residual stress changing sign. It is notable that most of the residual stress formulations are only calculated in the ITG mode dominated regime and not for the TEM regime.

Furthermore, given that rotation reversals have no known external source and, thus, are fully contained within the plasma, they provide a fascinating look at what

an experimental source profile looks like during an intrinsic plasma transition. The rotation profiles are fairly flat as they are both L-modes, which suggests that the residual stress is not as important as the standard diffusion and convection terms are. This is further supported by the pinning effect at the $q = 3/2$ surface (see Section 4.1), which fixes all of the action of the source within that surface, since the gradient and value of rotation are identical at the location of $q = 3/2$ to within experimental uncertainty.

TRANSP generated ion thermal diffusion profiles are shown in Figure 4-22, and the ion thermal diffusion is taken as the momentum diffusive values. Note that despite the similarity of the plasma profiles, the energy diffusion at the decreased density time (t = 1.0 s) is approximately 20% higher throughout the entire profile, which, given the rotation reversal's relation to the energy confinement time, is reasonable. The Peeters and Yoon forms of the convective velocity are shown in Figure 4-23. The Yoon convective term has a discontinuity at r/a=0.55, which occurs because of the term α_c which is divided by the ITG criticality relation. Therefore when the plasma transitions from ITG to TEM criticality the Yoon form of the convection can go through a discontinuity.

Using these profiles, the source profiles during the rotation reversal can be calculated using the "Toy Model." These profiles are shown in Figure 4-24 at two characteristic times under four assumptions: diffusion of 1.0 m^2/s, TRANSP calculated diffusion with no convection, TRANSP calculated diffusion and Peeters convection, and TRANSP calculated diffusion and Yoon convection. For comparison, a time trace of the source at various radii under the same assumptions is shown in Figure 4-25. It is seen that as a function of time these profiles do not change significantly, but there are temporal variations toward the core as the plasma transitions from LOC to SOC. All four profiles have a similar behavior around the $q = 3/2$ surface and are of generally the same magnitude as well. The Peeters calculation does better on axis than the purely diffusive form. Note that technically the Yoon form is derived for ITG modes, so it may not be valid in the LOC regime where it has sharp changes. Generally, the source required to explain the differences in the rotation profiles is

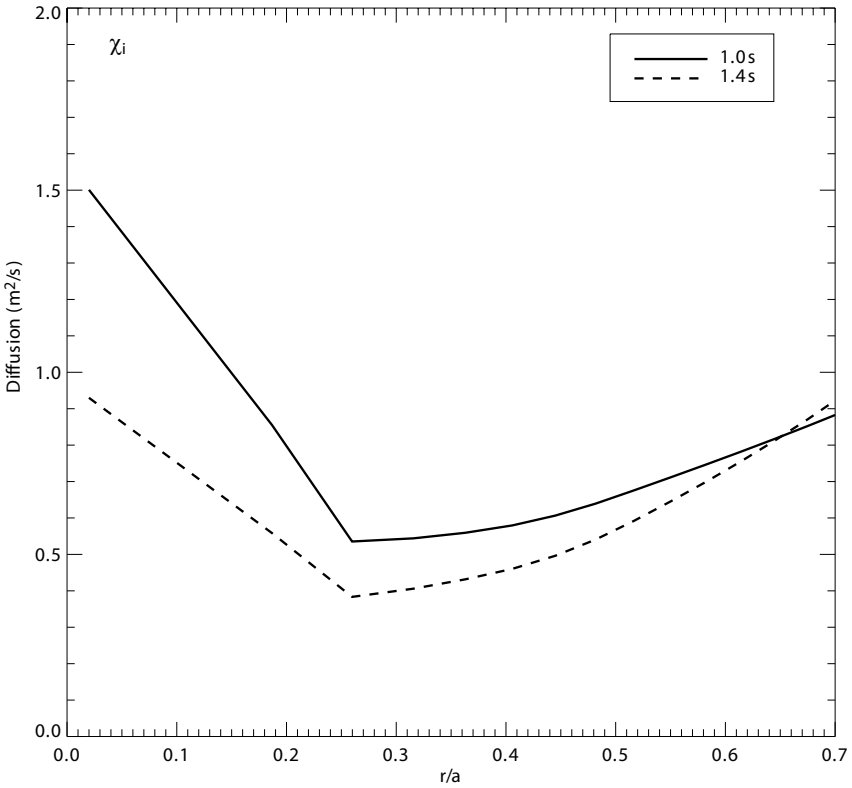

Figure 4-22: Average ion thermal diffusion values as calculated by TRANSP during the co-current (LOC 1.0 s) and counter-current (SOC 1.4 s) phases in a rotation reversal discharge.

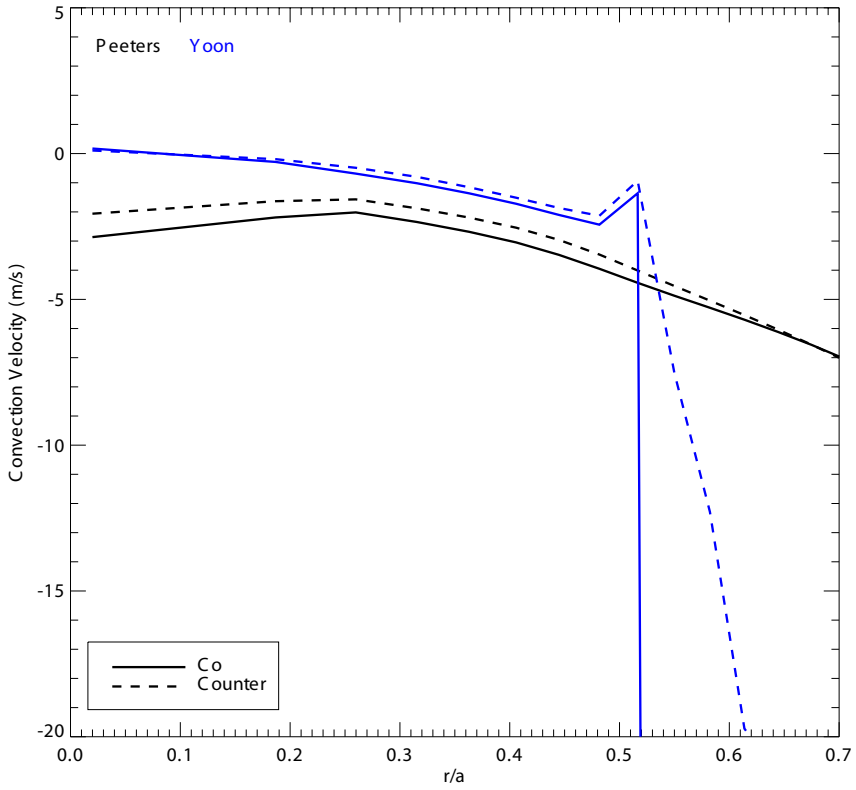

Figure 4-23: Average convective velocity values in the Peeters and Yoon form during the co-current (LOC 1.0 s) and counter-current (SOC 1.4 s) phases in a rotation reversal discharge.

somewhat negative in the core, with a negative peak around r/a=0.4 and with a positive peak around r/a=0.6. As the plasma transitions from LOC to SOC, the negative peak increases in size while the positive peak moves outward in radius. These profile changes, overall, represent large scale transitions throughout the bulk of the core plasma, suggesting that the entire plasma is changing rather than a localized source with transport accounting for the radial variations.

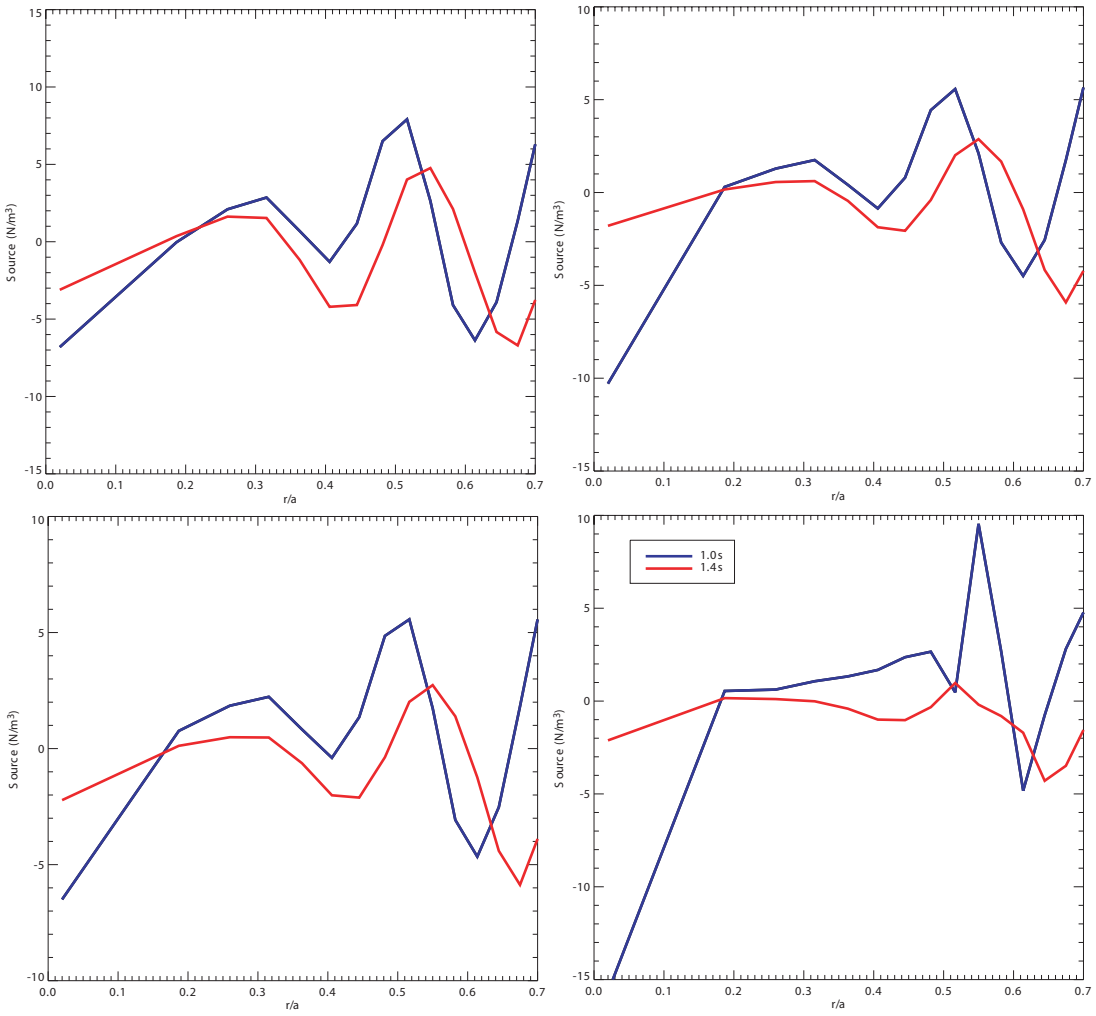

Figure 4-24: Rotation reversal source profiles using [top left] a constant diffusion (χ = 1.0 m^2/s) and no convection, [top right] a TRANSP calculated diffusion and no convection, [bottom left] a TRANSP calculated diffusion and Peeters convection, and [bottom right] a TRANSP calculated diffusion and Yoon convection. The dotted line represents the q=3/2 surface.

The q = 3/2 surface in this plasma occurs at approximately r/a=0.75, and the

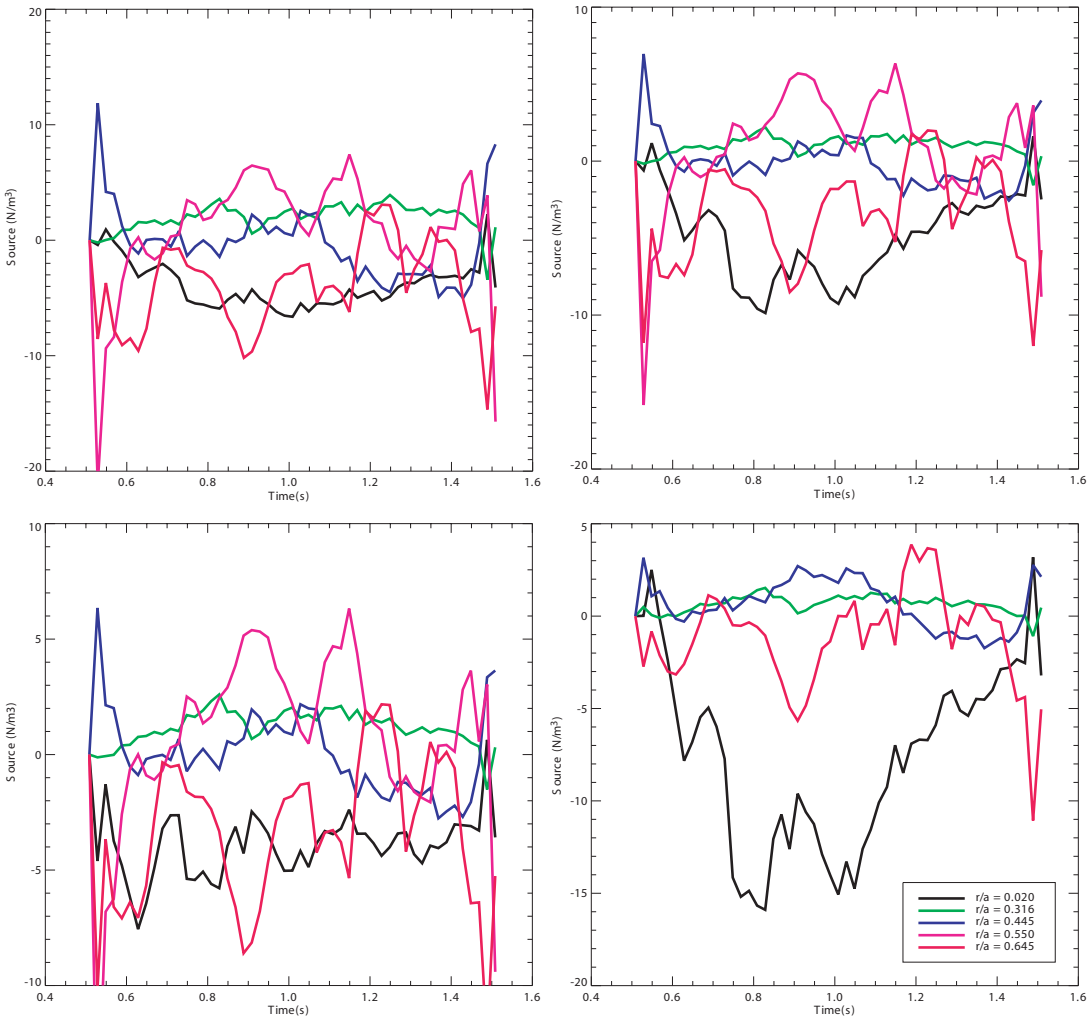

Figure 4-25: Source time traces at various radii with [top left] a constant diffusion (χ = 1.0 m^2/s) and no convection, [top right] a TRANSP calculated diffusion and no convection, [bottom left] a TRANSP calculated diffusion and Peeters convection, and [bottom right] a TRANSP calculated diffusion and Yoon convection.

source profile is peaked around that point. The major point of the source profile change occurs at r/a=0.4-0.6. This is in a flat diffusive and convective area of the plasma and is caused by the rotation profiles having a major change around the r/a=0.6 position. Interestingly, in the high density phase, the source profile has some variation around that position, but it generally remains fixed around zero within rotation error bars. In the low density section, however, there is a marked peak in the source profile, irrespective of the form of the convective term. There is a negative source seen on axis, which is required to explain the slightly hollow rotation profiles. In order to compare the source profile changes due to the rotation reversal, it is helpful to plot the normalized change in the source from LOC to SOC; this is shown in Figure 4-26.

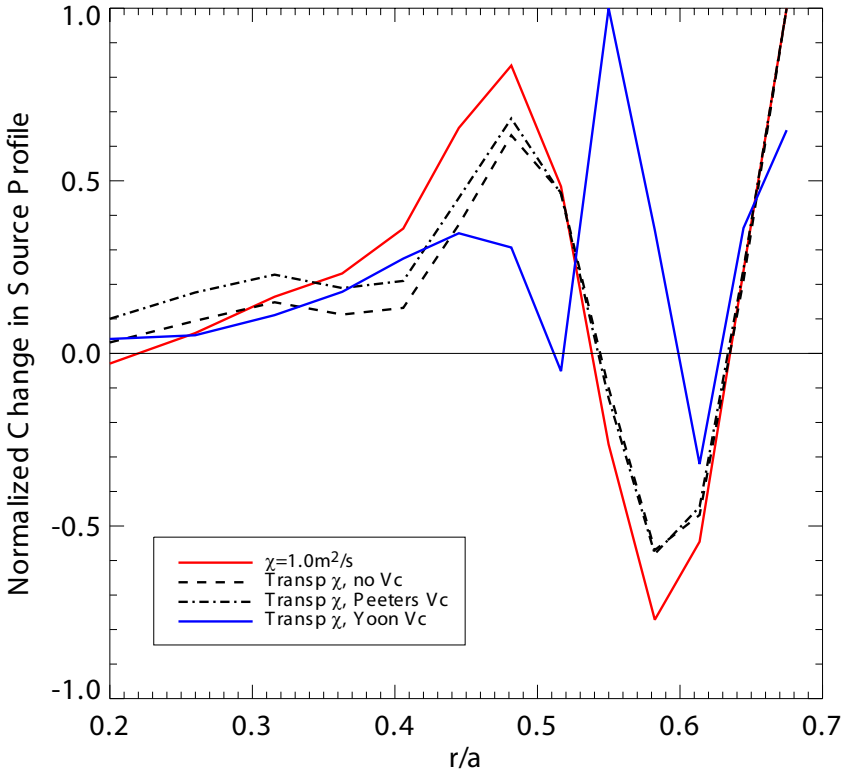

Figure 4-26: Normalized change in source profiles from the LOC to SOC phase.

There is no form of the convective/diffusive profile that is clearly superior to the other cases in the rotation reversal. It appears that the Peeters form may suffer fewer discontinuities due to its simple scaling, rather than the more complicated form of the

Yoon convection. None of the calculations of the source profile changes in the plasma from LOC to SOC have major differences in the profile shape, so this suggests that the calculations of the source are fairly resilient and are being caused by the physics of the rotation profile evolution.

The residual stress as derived by Diamond and Yoshida was also calculated to see if it can explain the profiles seen in this plasma transition. These calculations are shown in Figure 4-27. Neither calculation is capable of perfectly reproducing the experimental observations of the source profile in the plasma. The Diamond source agrees fairly well with the actual residual stress calculation at t=1.4 s (with no convective term), but it does not reproduce the negative lobes at r/a=0.4 or in the core. Since the Diamond form of the residual stress is calculated for ITG turbulence and at 1.0 s the linear turbulence is found to be much more strongly in the TEM regime, the disagreement at that time is not unexpected. The Yoshida source form underestimates the required source, but it is able to reproduce the qualitative shape of the profiles, even the negative lobe at approximately r/a=0.4. The Yoshida calculation is shown with the residual stress calculated with both 1.0×10^{-7} and 3.0×10^{-7} m^{-1} values of the coefficient α_k, but this naturally does not affect the shape of the residual stress.

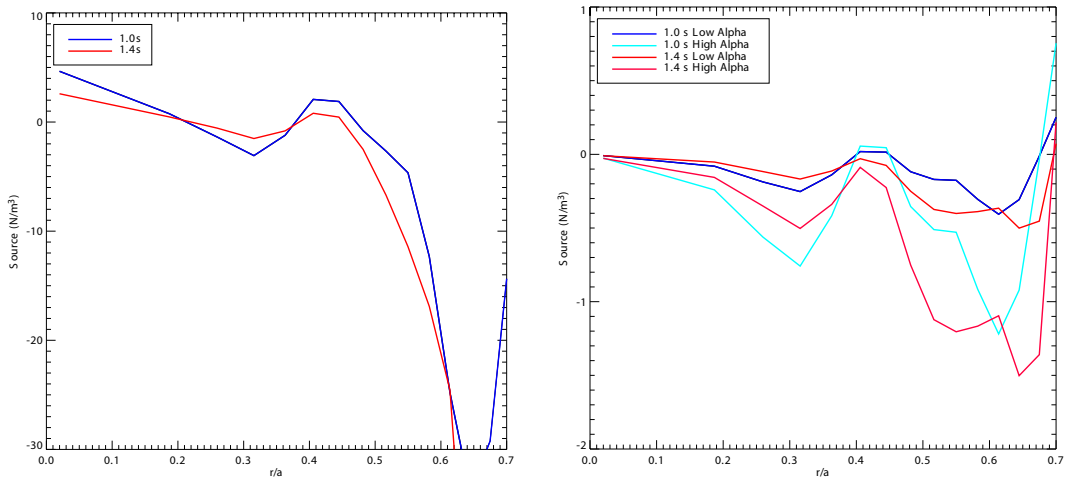

Figure 4-27: Calculation of the residual stress from the Diamond and Yoshida equations.

4.4 Summary

Rotation reversals are spontaneous inversions of the plasma rotation direction as a function of density, current, plasma shape, or magnetic field. It has been found that they are correlated with the transition of the plasma from LOC to SOC, and the reversal is likely the most telling predictor of that transition. The explanation for the plasma spontaneous reversal of direction is the transition from a TEM dominated plasma, in the linear Ohmic confinement regime, to an ITG dominated plasma, in the saturated Ohmic confinement regime. Linear stability modeling supports the assertion that the rotation reversal is correlated with mode transitions, but it is unable to reproduce the exact density behavior of the modes. Density scans qualitatively cause the correct changes in the linear turbulence, but too large density changes are required to cause the ITG/TEM transition in the simulations. It is instead conjectured that the ratio of the electron temperature to the ion temperature, which changes across the rotation reversal boundary, is the primary correlation with the mode transition and thus the rotation changes. Non-linear effects may change the stability diagrams, so they should be taken into account in future simulations.

Source profiles during the transition have been analyzed in order to understand the form of the residual stress for this transition and compare it to the models of the residual stress proposed in Section 2.4.2. It is seen that the majority of the source profile changes are localized at r/a=0.4-0.6. The convective terms in these plasmas did not significantly improve the fits to the data. The magnitude of the required source profiles was reproduced by the Diamond form of the residual stress, but the shape was better reproduced by the Yoshida form.

THIS PAGE INTENTIONALLY LEFT BLANK

Chapter 5

Lower Hybrid Current Drive Induced Rotation Changes

Lower Hybrid Current Drive (LHCD) has been a major area of interest in the plasma physics community since the 1980s. There has been a general effort in the field to find current drive mechanisms that will allow a tokamak to operate for longer time scales than those currently feasible using only the central solenoid. These methods include neutral beams, electron cyclotron waves, fast wave ion cyclotron, lower hybrid current drive, and a variety of less used mechanisms. These mechanisms all have various benefits and challenges. The expense and penetration issues of neutral beams make them difficult to use on a reactor. While fast wave current drive and electron cyclotron current drive are fairly efficient, particle trapping at larger r/a values makes them non-ideal for off-axis current drive. Lower hybrid current drive is able to drive current off-axis which makes it particularly useful for advanced scenario tokamak operation ($q > 1$). The downside of LHCD is that it has difficulty operating at high density due to accessibility issues. All of the previously mentioned methods are discussed in detail in [81].

5.1 LHCD Background

A simplified discussion of the LHCD physics issues is presented here. The Lower Hybrid system launches a wave which is represented in the cold plasma electrostatic limit with the following dispersion relation

$$k_{\perp}^2 = k_{||}^2 \frac{m_i}{m_e} \frac{\omega_{LH}^2}{\omega^2 - \omega_{LH}^2} \tag{5.1}$$

where $\omega_{\mathrm{LH}}^2 = \omega_{\mathrm{pi}}^2/(1+\omega_{\mathrm{pe}}^2/\omega_{\mathrm{ce}}^2)$ and $\omega^2 \ll \Omega_{\mathrm{ce}}^2$. The parameter $k_{||} = 2\pi/\lambda$ is the parallel wave number and is directly related to the parallel refractive index $n_{||} = ck_{||}/\omega$. The LH launcher defines the frequency and approximate parallel wave number, which only varies slightly in the plasma, of the wave, so the dispersion relation solves for the free parameter $k_{\perp}$. In warm and hot plasmas, the dispersion relation is more complicated and is discussed in detail in [82].

The actual physics of LHCD involves considerations of decay of the lower hybrid wave, the section of the distribution function that the wave damps on, and the importance of the plasma edge with regard to launcher-to-plasma coupling. This generally requires using simulation codes to calculate on which section of the plasma the waves deposit their energy and how much current this drives. Understanding the rotation drive from a simulation standpoint has been researched in more detail in [83], but the work is still in progress and is currently in the process of developing more advanced momentum conserving collision operators in the simulation code.

Nevertheless, in a simplified form, plasma current is defined as $J = -en(v_e - v_i)$, meaning that driven current is related to the rotation of the charged species. This implies that driving current is, in effect, driving rotation. The momentum of the plasma is mainly carried by the main ions which have significantly more mass than the electrons, while LHCD drives current primarily through the electron current, so this rotation would only be visible if the ions and electrons are coupling successfully. It is important to note that the lower hybrid driven electron tail would be near relativistic, since the refractive index in this situation is often $n_{||} = ck_{||}/\omega \sim 2$, implying a phase speed of $v_{ph} \sim 1.5 \times 10^8$m/s. At this velocity, the electron-ion

collision rate ($\nu_{ei} \approx e^4 n_i \ln\Lambda / 4\pi\epsilon_0^2 m_e m_\mu v_e^3$) is of order 5 ms, which, while long, is still below the energy confinement time. It was found that the fast electron to ion coupling could be even higher if the full parallel refractive index spectrum is analyzed [84], suggesting that the direct momentum input of the wave could be important for plasma rotation.

5.2 Previous LHCD Rotation Observations

LHCD has previously been seen to induce rotation in Alcator C-Mod plasmas [85, 86]. This rotation was observed to be in the counter-current direction and scales with P_{LH}/n_e. Furthermore, the rotation magnitude is proportional to the internal inductance, l_i, which is a proxy for the current modification, and scales inversely with the parallel refractive index, which controls the location of the fast electron distribution on which the wave damps its power. The time scale of this rotation change was ∼100 ms, which is approximately the current relaxation time $\tau_{curr} = 1.4\kappa a^2 T_e^{1.5}/Z_{eff}$, where T_e is in units of keV, a is in units of meters, and τ is in units of seconds.

LHCD induced rotation has also been observed on JT-60U [87], Tore Supra [88], JET [89], and, recently, on EAST [90]. In all of these cases, the rotation change was in the co-current direction, with JT-60U reporting that the entire profile was elevated. Available plasma parameters from each of these experiments are shown in Table 5.1.

Table 5.1: Table of machine parameters relevant to LHCD rotation studies for Alcator C-Mod, JT-60U, Tore Supra, JET, and EAST. Approximate values are calculated from provided data in the reference papers.

Machine	B_T [T]	I_p [MA]	q_{95}	n [10^{20}m^{-3}]	P_{LHCD} [MW]
Alcator C-Mod	5.4	0.3-0.9	3-10	0.66	0.8
JT-60U	4	∼1	∼6	0.05	1.5
Tore Supra	3.7	0.8, 1.51	∼ 5.9, 3.1	∼0.16, 0.3	1.8-3.8
JET	2.4-2.8	ramp-up	ramp-up	0.43-0.65	< 2.0
EAST	2	0.250	10	0.08	0.8

On Alcator C-Mod, co-current LHCD induced rotation was observed recently for the first time. It was seen in both upper single null (USN, unfavorable B × ∇B drift

direction) discharges and lower single null (LSN, favorable B $\times$ ∇B drift direction). It was observed that the co-current rotation in USN plasmas scaled inversely with plasma current. These observations led to a dedicated experiment being performed in order to test the dependence of the rotation change on current and to understand the issue of the direction of the LHCD induced rotation.

5.3 Co- and counter-current LHCD induced rotation changes on Alcator C-Mod

Dedicated experiments at Alcator C-Mod on LHCD induced rotation in the co- and counter-current direction have been performed at $B_{\mathrm{T}} = 5.4\mathrm{T}$, $<n_e> = 0.66 \times 10^{20}\mathrm{m}^{-3}$, plasma elongation $\kappa \approx 1.6$, and no auxiliary heating other than that due to LH wave injection. Plasma current was scanned from approximately 300 kA through 900 kA. The lower hybrid launcher was run at 800 kW of net power into the plasma and a launched refractive index $n_{||} = 1.6$, which is known to give a large counter-current rotation from the previous C-Mod LHCD rotation results.

Overall, several reproducible discharges were accomplished in upper single null and lower single null. A characteristic trace of the line-integrated plasma rotation in both the co- and counter-current directions is shown in Figure 5-1. During the high current case (black trace), the rotation drive was in the counter-current direction with a rotation change of $\Delta v \sim -20$ km/s. At low current (blue trace), however, the core rotation is driven in the co-current direction $\Delta v \sim +30$ km/s and only appears to initiate after $\sim$100 ms of the LHCD pulse. A mid-current case is also shown (in red), in which there is no net rotation change during the LHCD phase; small variations in rotation are seen, but they average out over the course of the discharge. When the lower hybrid system turns off, it is often seen that there is a sharp counter-current swing in rotation. It is not well understood what is causing this counter-current impulse. All of the upper single null discharges were sawtooth stabilized by LHCD, with the time of the stabilization depending on the current. The high current lower

single null discharges had sawteeth all throughout the discharge; the sawteeth were stabilized in the lower current cases, though.

The summary of the rotation results for different currents is shown in Figure 5-2. The change in core rotation is calculated by subtracting the pre-LHCD rotation from the final rotation during the LHCD phase. It is observed that the plasma current has a strong effect on the plasma rotation magnitude and direction. Furthermore, the USN and LSN plasmas show a marked difference in the rotation behavior. The critical rotation zero-points (alternatively called LHCD rotation reversal points) for the USN and LSN plasmas are approximately 550 kA and 400 kA. It is worth noting that location of the Ohmic rotation reversal, discussed in Chapter 4, (red dashed line) in current space is fairly close to that of the observed LHCD rotation reversal, giving the first indication of the possible relation between the two phenomena. Characteristic discharges from the previous LCHD discharges on Alcator C-Mod are overplotted on this summary as well. These discharges show why this effect may have never been observed previously: the previous experiments were all run in the higher current, seemingly asymptotic rotation change section of the figure. In order to transform the data to a dimensionless form, the q value is substituted for the current and rotation changes are shown in terms of ion thermal Mach number, which is presented in Figure 5-3. Given that Figure 5-3 is in a dimensionless form, it is possible to compare C-Mod data with other machine data. Only the Tore Supra and EAST data were available for this comparison, and they are overplotted in the figure. It is seen that they both approach the high q-values where the rotation is in the co-current direction. It is nevertheless an imperfect comparison to overplot these data because of their different densities, magnetic fields, and heating mechanisms.

Rotation profiles of the USN and LSN cases at high and low current are shown in Figure 5-4. It is observed that the rotation profiles appear to be pinned at r/a $\approx$ 0.5-0.6, which suggests that the effect of the LHCD rotation drive is localized to the core of the plasma than to the edge. At the start of LHCD, the rotation at high current transitions to the counter current direction, while low current discharges have co-current rotation profiles with the largest change located in the core.

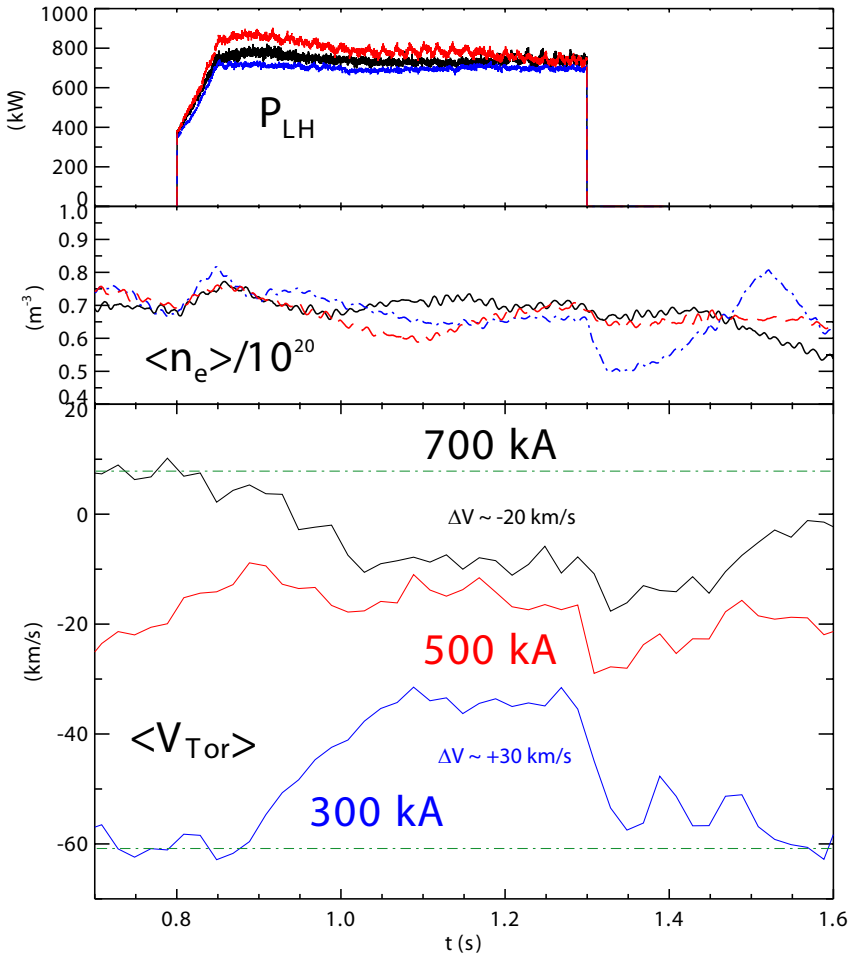

Figure 5-1: Characteristic (taken in the USN case) time histories of LHCD induced rotation: lower hybrid power, average density, and line integrated rotation are shown. Dashed, blue lines represent the 300 kA case with co-current rotation and black lines represent the 700 kA case with counter-current rotation. The red mid-current case is shown for comparison to demonstrate a nearly no rotation change situation.

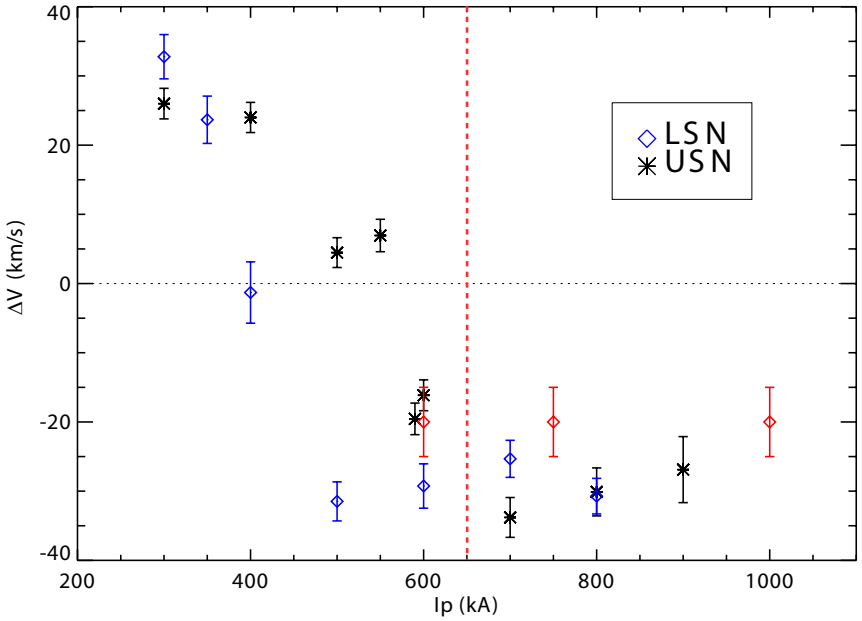

Figure 5-2: Rotation change from LHCD versus plasma current. Diamonds (asterisks) represent equilibria with ion ∇B drift toward (away from) the X-point. Red points are from 2008 data; density and LHCD power are 10% higher than current values, and the points are shown for comparison. All data from respective years are at fixed density and power. The dashed red line marks the "empirical" position of the intrinsic plasma rotation reversal with $q(r) < 1$.

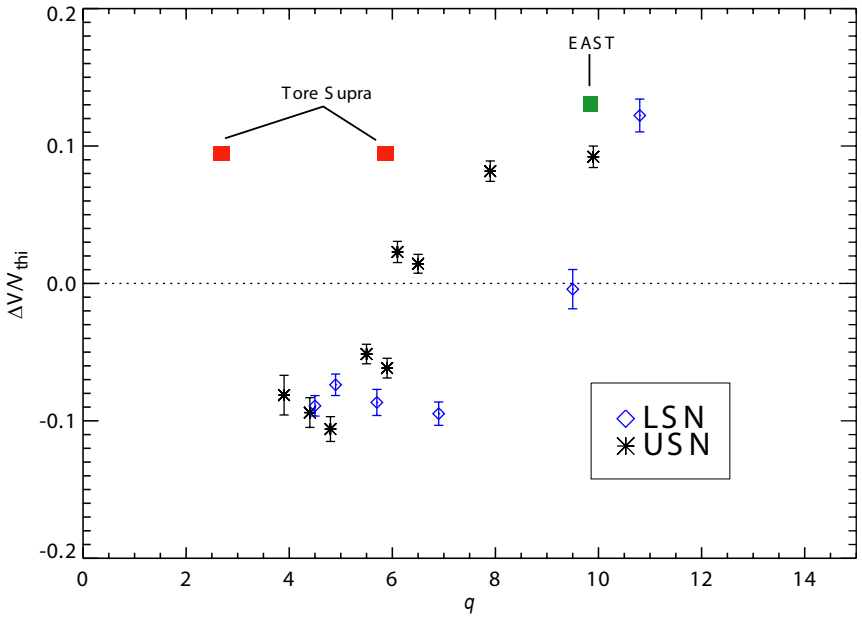

Figure 5-3: Rotation change normalized to ion thermal speed from LHCD versus q. Diamonds (asterisks) represent equilibria with ion ∇B drift toward (away from) the X-point and diamonds are toward the X-point. The red and green boxes represent the overplotting of Tore Supra and EAST published results with regard to their rotation.

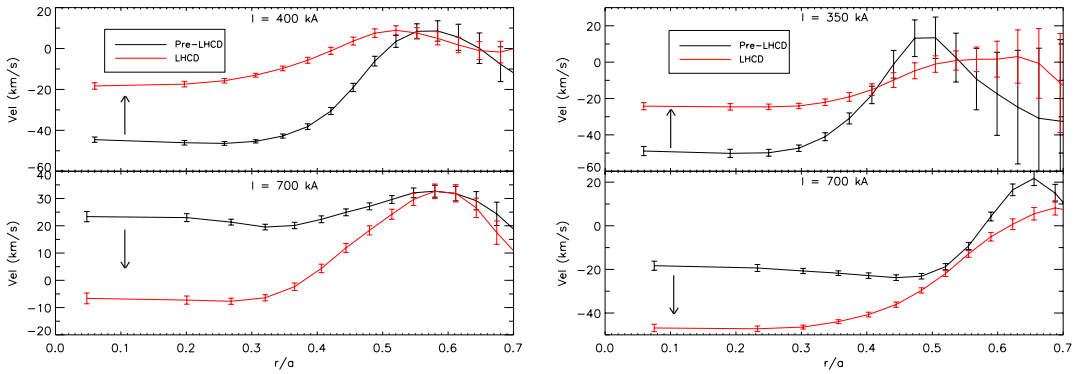

Figure 5-4: Characteristic rotation profiles before and during LHCD for two USN (left) and two LSN (right) discharges. Both high and low current cases are shown, and statistical errors bars are shown as well. Note that error bars in the low current case around r/a = 0.5 increase due to uncertainties in the EFIT reconstruction.

An interesting observation is that the disappearance of the sawteeth in these discharges varies depending on the current and the configuration of the plasma. A plot of the sawteeth disappearance times is shown in Figure 5-5, where it is seen that, as expected, as the current increases it takes longer for the LHCD to drive sufficient current to force the sawteeth to disappear. The LSN discharges have significantly larger disappearance times than the USN discharges. It is likely that the current drive from LHCD is significantly worse in the LSN versus the USN case, which may explain some of the discrepancy seen between the two cases' rotation results.

5.4 LHCD Rotation Theory

It has been proposed that the counter-current direction of rotation from LHCD is caused by the direct momentum input of the waves driving fast electrons in the counter-current direction [83]. The electrons then collisionally couple to the main ion species and drive counter current directed momentum. The estimated rotation drive using this method can be approximated with $n_i m_i \Delta(R v_\phi)/\Delta t = T_{LH} = R n_{||} P_{LH}/c$ and leads to a ∼40 km/s change from LHCD which is the correct order of magnitude in the counter current direction. This calculation assumes a time constant of the change of ∼100 ms, which is what is normally measured on Alcator C-Mod and is

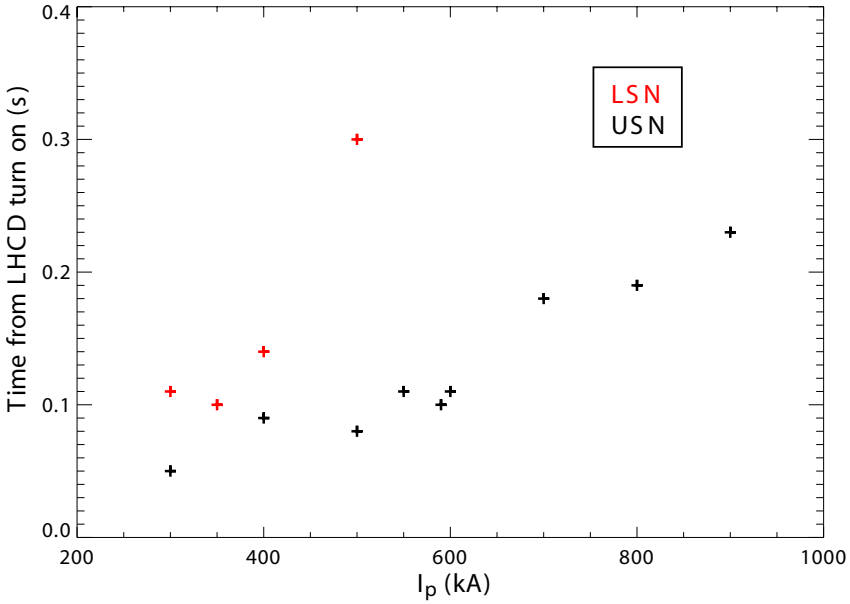

Figure 5-5: Sawteeth disappearance times as measured by the electron cyclotron emission system versus current and magnetic configuration.

also approximately the current relaxation time. While this method may explain the counter-current rotation observed previously and produces synthetic rotation profiles that qualitatively agree with the experiment, it does not explain how LHCD can drive co-current rotation. There have been many proposals about what could be the reason for this co-current rotation. Several of these proposals are presented below.

1. **Fast Electron Losses**. This mechanism was suggested by the Tore Supra and JT-60U groups, and it is based on the formation of a radial electric field (E_r) in the outward direction. Ripple (toroidal asymmetries in the magnetic field) losses of fast electrons are assumed to cause an outward radial electric field. This radial E_r would cause a toroidal rotation via radial force balance

$$E_r \approx v_\phi B_\theta - v_\theta B_\phi + \frac{1}{Z_i e n_i} \nabla p \tag{5.2}$$

where the equation is evaluated for the rotating species. Lower hybrid is expected to generate increased ripple losses and, thus, generate co-current rotation. HiReX Sr did not observe large ($>$ 5km/s) changes in the poloidal rotation during the LHCD as seen in Figure 5-6, so the second term can often

be neglected, and the third term is generally considered to be small due to the coefficient being divided by the rotating species' charge and flat profiles of density and temperature. This leads to the approximation that the interior radial electric field is primarily an effect of the toroidal rotation and poloidal magnetic field, therefore, radial E_r and toroidal rotation are strongly coupled.

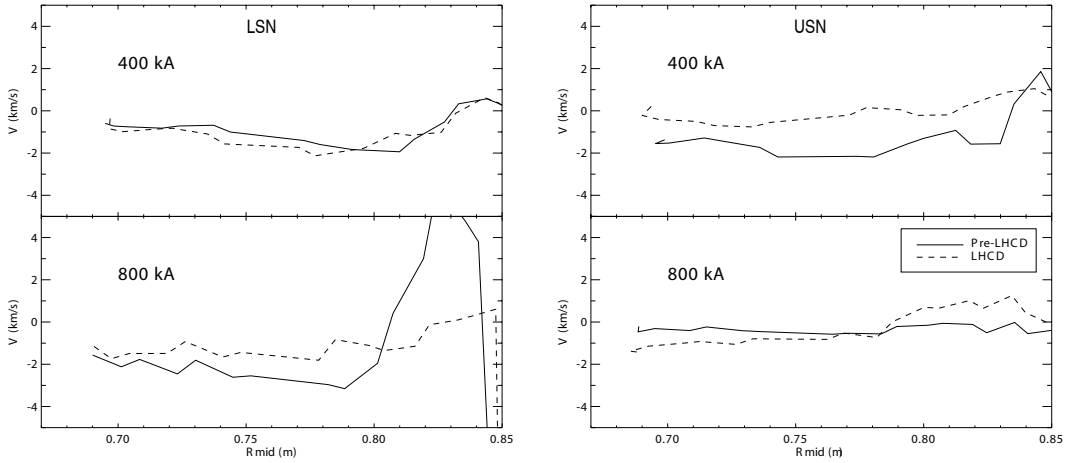

Figure 5-6: Poloidal rotation changes during LHCD discharges in lower and upper single null.

It is unlikely that this is the explanation of the co-current rotation on Alcator C-Mod. C-Mod's ripple field is approximately 1% [91], whereas Tore Supra's is approximately 7%. Furthermore, in work performed at Tore Supra, it was found that the fast electron loss due to magnetic ripple scales linearly with plasma current [92]. This implies that the radial electric field and thus the co-current rotation should increase with plasma current, whereas the rotation actually decreases with increasing plasma current. Finally, the ripple generally increases towards the edge of the plasma, so one may expect that the observed rotation changes should also increase towards the edge of the plasma, but the observation is that the rotation initiates in the core rather than at the edge. These findings demonstrate that the ripple loss of fast electrons is not a likely explanation for the co-current rotation.

2. **Convective Velocity From Changes at the Plasma Edge**. The proposal for the explanation of the co-current rotation from EAST [90] was that the edge

rotation was changing, and the convective velocity in the plasma is transporting that rotation toward the core. The pinch velocity in this case is taken to be $v_c/\chi_i = -4/R$ from the Peeters form of the pinch. EAST had edge measurements of the rotation velocity that changed significantly during the discharge. By calculating the core rotation from the edge using this model for the convective pinch it was found that the calculation and the data seemed to agree.

A model with no residual stress and a convective form of the pinch that is simply related to the ion diffusion will always create a monotonically increasing or decreasing rotation profile. These forms can explain an H-mode or I-mode rotation profile, but in LHCD driven plasmas it is observed that there is a pinning point off-axis. At this point, the rotation does not change from the pre-LHCD phase to the LHCD phase. This pinning in rotation is not possible with a simplified model of momentum transport such as that described above. At the pinning location, the diffusive and convective transport of momentum would be identical in both the high and the low current cases and, thus, the rotation inside the pinning location would be identical.

3. **Intrinsic Rotation Reversals**. Ohmic L-mode plasmas have been observed to reverse rotation direction spontaneously with slight changes of current, density, and magnetic field, and this has been discussed in more detail in Chapter 4. The observed reversal current at the operational density and magnetic field of the LHCD experiment is $\approx$ 650kA. This current is within 20% of the calculated LHCD induced reversal point based on the scaling in [3], and this is shown for 5.4 T discharges in Figure 5-7, so there may be turbulence changes from the LHCD that are causing differences in the plasma behavior. Furthermore, at the end of flat top of the LHCD phase of the plasma, the rotation appears to approach a similar value; if this behavior is repeated at other densities, this suggests that the LH system is changing the plasma behavior rather than directly inputting momentum. Several traces of rotation are shown in Figure 5-8, where velocities appear to approach approximately -20 km/s, except for the 300 kA case.

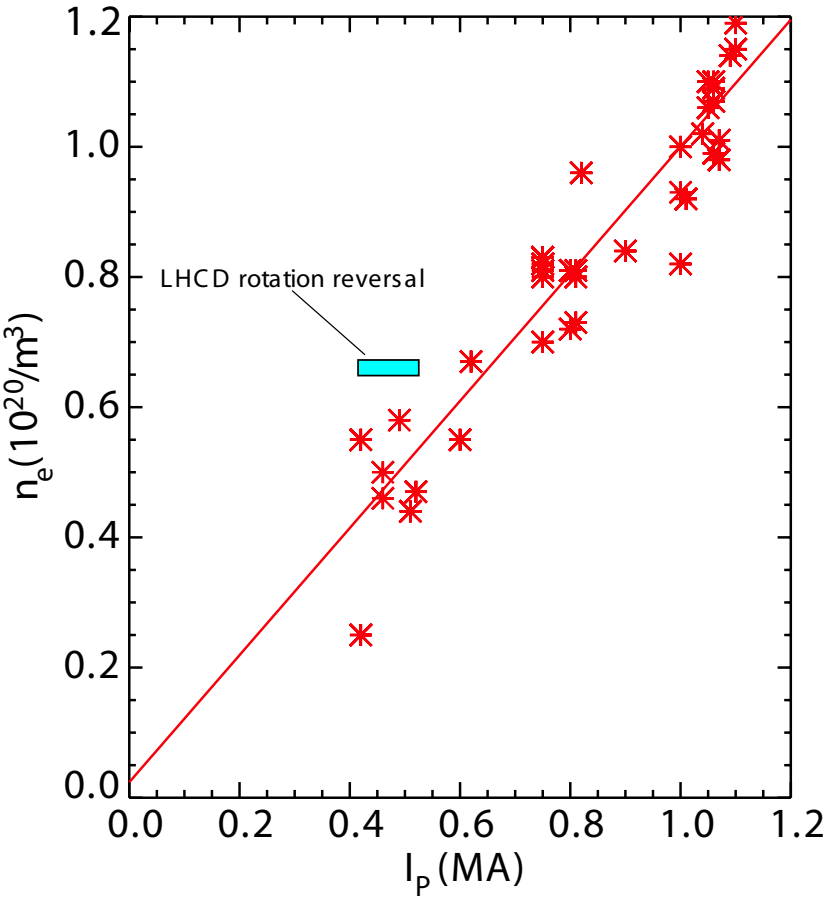

Figure 5-7: Overlayed LHCD rotation reversal point on the intrinsic rotation reversal densities at 5.4T. Note that while the LHCD rotation reversal is somewhat removed from the line, it is still fairly close in n_e vs I_P space.

These observations suggest that the LHCD is changing the intrinsic plasma behavior, and the rotation is due to a modification of the density and temperature profiles by the current drive. If the rotation is purely controlled by changes in the profiles then it would not be expected to see any concurrence of the rotation behavior with direct momentum input from the launcher. The counter-rotation effect, however, seems to agree with the modeling, suggesting multiple coupled generating mechanisms. Furthermore, some of the traces in Figure 5-8 have an initial counter-current change even in net co-current rotation cases supporting the argument that at least two drivers are acting.

Using the simplified model of momentum transport as in Section 2.3, the residual stress is calculable. The form is shown in Equation 2.30, and is listed again below for convenience.

$$\Pi_r^{res} = -\rho_* \frac{L_s}{2c_s} \chi_i \left(\frac{\nabla T}{T} \right)^2 v_{th,i}^2 \tag{5.3}$$

where c_s is the sound speed, χ_i is the ion thermal diffusivity, $v_{th,i}$ is the ion thermal speed, and ρ_* is the normalized Larmor radius. All of the terms are positive while $L_s = R_0 q^2 / r(\partial q / \partial r)$ is the only one that can be negative or positive due to the reversed shear. LHCD can create such a reversed q-profile by driving current off-axis. Since rotation depends on the divergence of the residual stress, hollow temperature profiles can also cause rotation to reverse, but these profiles were not observed in the LHCD plasmas. This implies that a q-profile change is causing multi-directional changes in the plasma rotation; more research on this topic can be found in [93]. As seen in Figure 5-9, the LHCD deposition profile (as calculated by GENRAY [94]) and, thus, the q profile will be different in high and low current cases.

MSE measurements of q-profiles were available on several of the discharges from this experiment [95]. A comparison of high and low current discharges is shown in Figure 5-10. It is notable that in the low current upper single null case, the data show highly reversed shear q-profiles, which are hallmarks

of advanced tokamak profiles. The low current LSN case, however, does not show an inverted q-profiles, while the rotation profiles, nevertheless, experience highly co-current driven rotation. The low current rotation profile change is narrower than the high current case for both q-profiles, which agrees with the lower hybrid estimated deposition profiles.

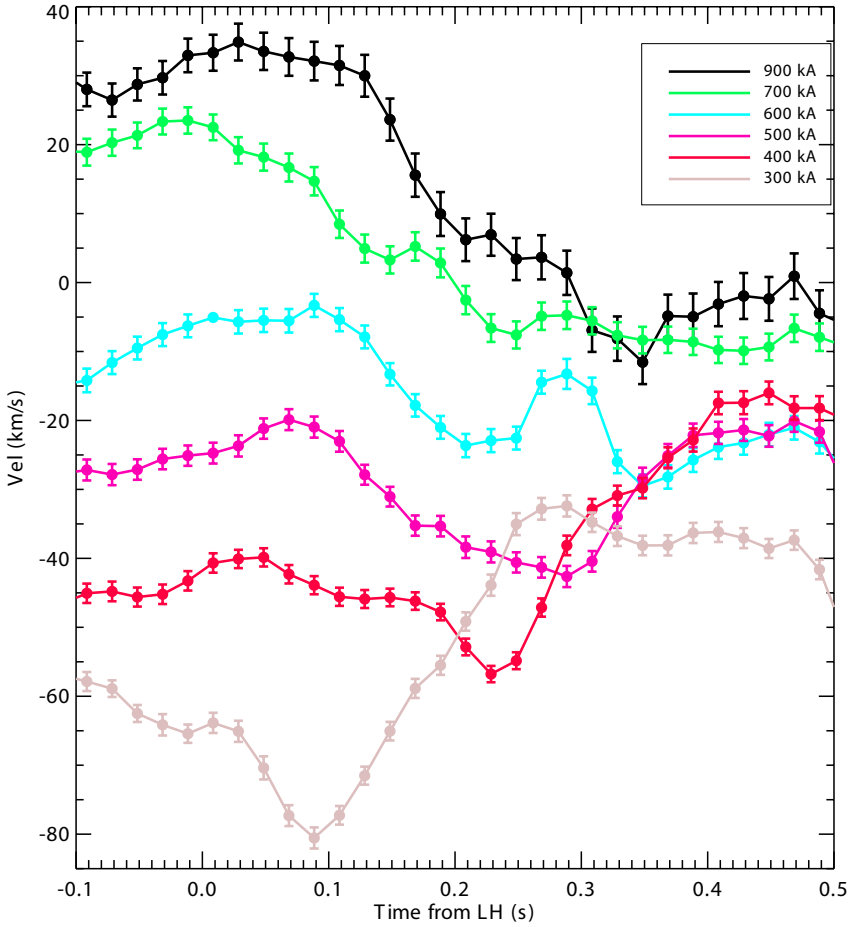

Figure 5-8: Overlayed time traces of core rotation value during the plasma current scan. These are inverted local rotation values, and statistical error bars are shown.

A scan of the same plasma parameters was performed at lower LHCD power. One of these discharges is shown in Figure 5-11, where it is seen that at 600 kW and 800 kW of Lower Hybrid there are two different rotation behaviors. At 600 kW the rotation does not appear to change during the LHCD phase while at 800 kW there is a noticeable rise in plasma line integrated rotation. In these cases, there are also measured internal inductance changes from 1.8 to 1.6 for the 800 kW case and 1.85 to

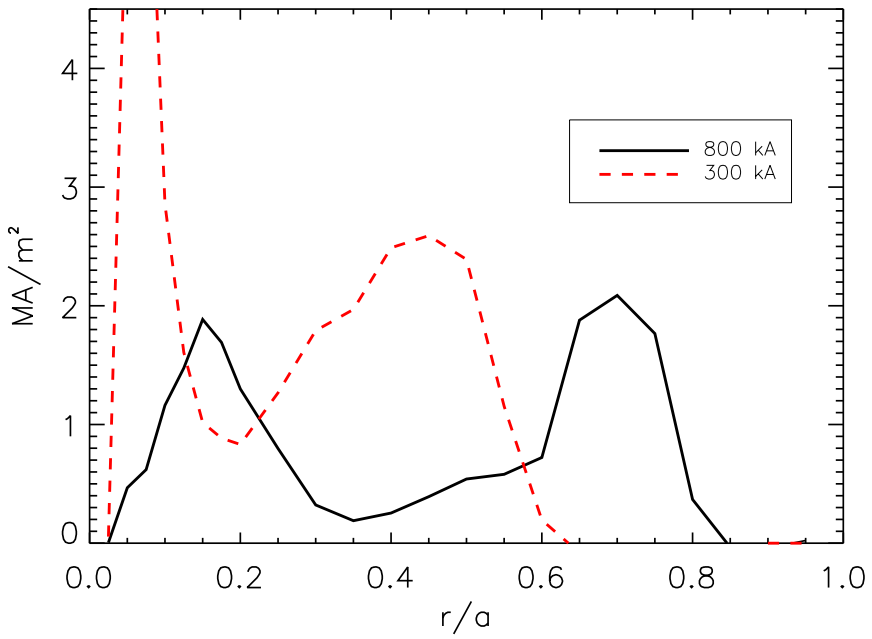

Figure 5-9: GENRAY calculated deposition profile of LHCD power from a 300 kA discharge and a 800 kA discharge. Note broader deposition profile in high current case.

1.7 for the 600 kW case, confirming that there are differences in the internal current profile modification. Since there are no other plasma changes, this result implies that one of two effects may be driving the rotation change: the modification of the q-profile or the ratio of T_e to T_i. The q-profile change in LSN and USN was significantly different as shown previously, so the value of T_e/T_i seems a likely explanation for this reversal effect. This parameter is also what is likely involved in the Ohmic rotation reversal, which the LHCD rotation reversal appears to be related to as well.

In general, it appears that the rotation mechanism for LHCD induced rotation is due to a combination of several different effects acting in concert. The most likely explanation appears to be that the rotation is primarily dominated by the intrinsic plasma rotation with possible shifts due to the direct momentum input from the LH wave.

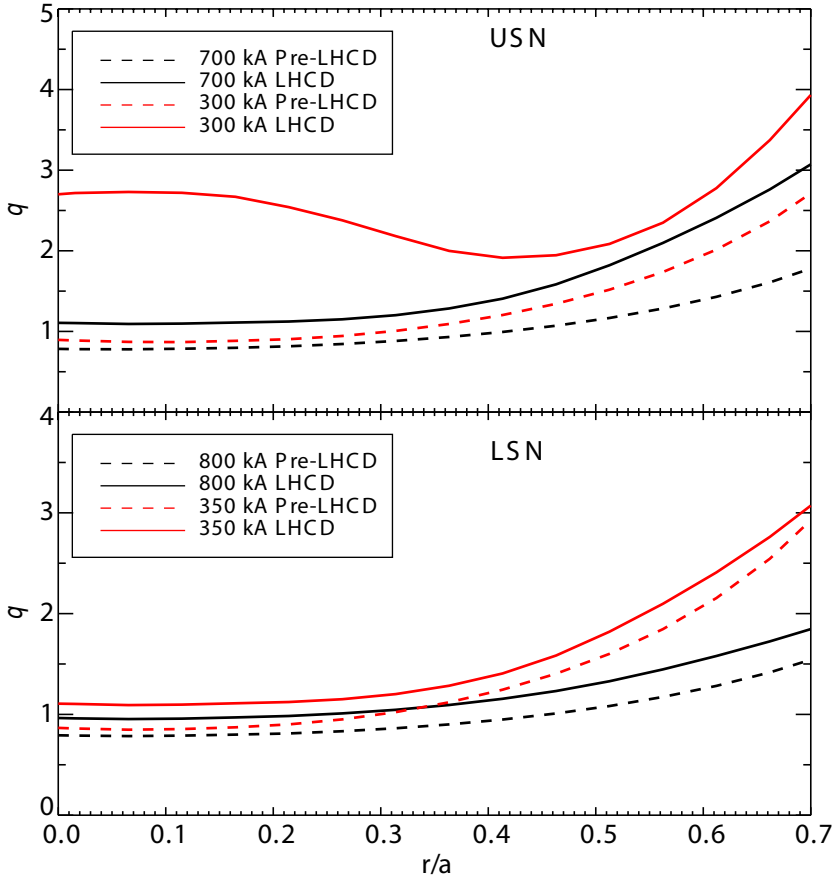

Figure 5-10: Profiles of MSE constrained kinetic EFIT measurements of the q-profile. Four profiles are shown in each plot with the top plot corresponding to USN plasmas and the bottom plot corresponding to LSN plasmas. In both low current cases, reversed magnetic shears are observed, but the USN case has a significantly more reversed profile.

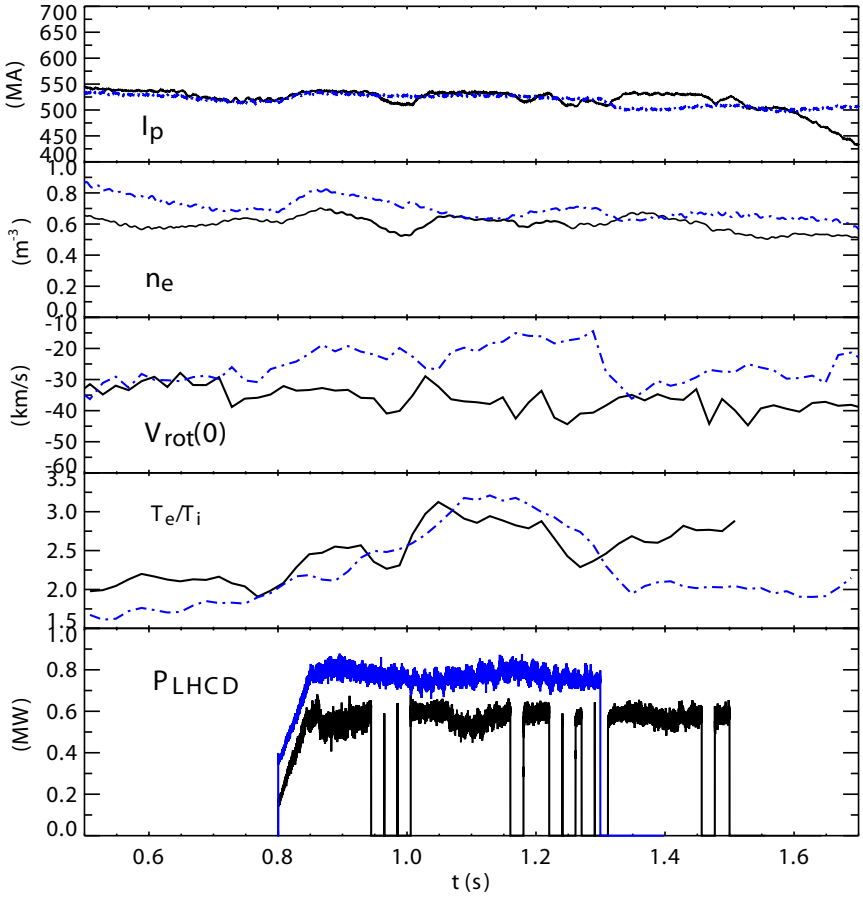

Figure 5-11: Comparison of 600 kW (black trace) and 800 kW (blue trace) LHCD discharges. Note that the lower power trace has almost no rotation change when the LHCD power turns on.

5.5 LHCD relation to Intrinsic Rotation Reversals

The change in the residual stress through q or T_e/T_i is considered the most likely candidate to explain the LHCD rotation. Ohmic rotation reversals are believed to be created by the TEM/ITG changeovers when the plasma transitions from to Linear Ohmic Confinement to Saturated Ohmic Confinement, so it is logical to search for features consistent with the ITG/TEM changeover during LHCD.

5.5.1 Observed Turbulence Differences

One of the most interesting observations during the LOC/SOC transition is the density fluctuation modification discussed in Section 4.2. It has been observed that during LHCD on Alcator C-Mod, there is a marked modification of the turbulence spectrum as well, as measured by the PCI system. In Figure 5-12 turbulence spectra are shown. During the LHCD phase at high current, it is seen that a wing of the fluctuation spectra increases in magnitude. The phase velocity of this turbulence is calculated to be 1 km/s (note, however, that sufficiently accurate, <1 km/s, poloidal rotation measurements are not available for this correction, so a Doppler shift may be important in this phase velocity calculation). This wing appears intermittently and is only seen during the counter current rotation of the LHCD. During co-current rotation the turbulence spectrum does not change, as shown in the figure.

These turbulence plots are reminiscent of the turbulence "wings" seen in the rotation reversal research. This observation supports the assertion that rotation reversals and lower hybrid rotation change reversals are related via turbulence changes in the plasma. Furthermore, these spectra show that there are major turbulence differences between the co- and counter-current rotation cases. These turbulence plots are asymmetric in wavenumber space, which, given the geometry of the PCI system, implies that the fluctuations are located either at the top or at the bottom of a flux surface. While not impossible, this asymmetric geometry is rarely observed and is thought to be caused by rotation shear in the core. The wings in the rotation reversal only appear during the co-current LOC phase of the plasma, while in the LHCD case the

asymmetric wings appear in the counter-current phase only. This is not consistent with the Ohmic reversal data, but as shown below it is consistent with the appearance of TEM in the plasma.

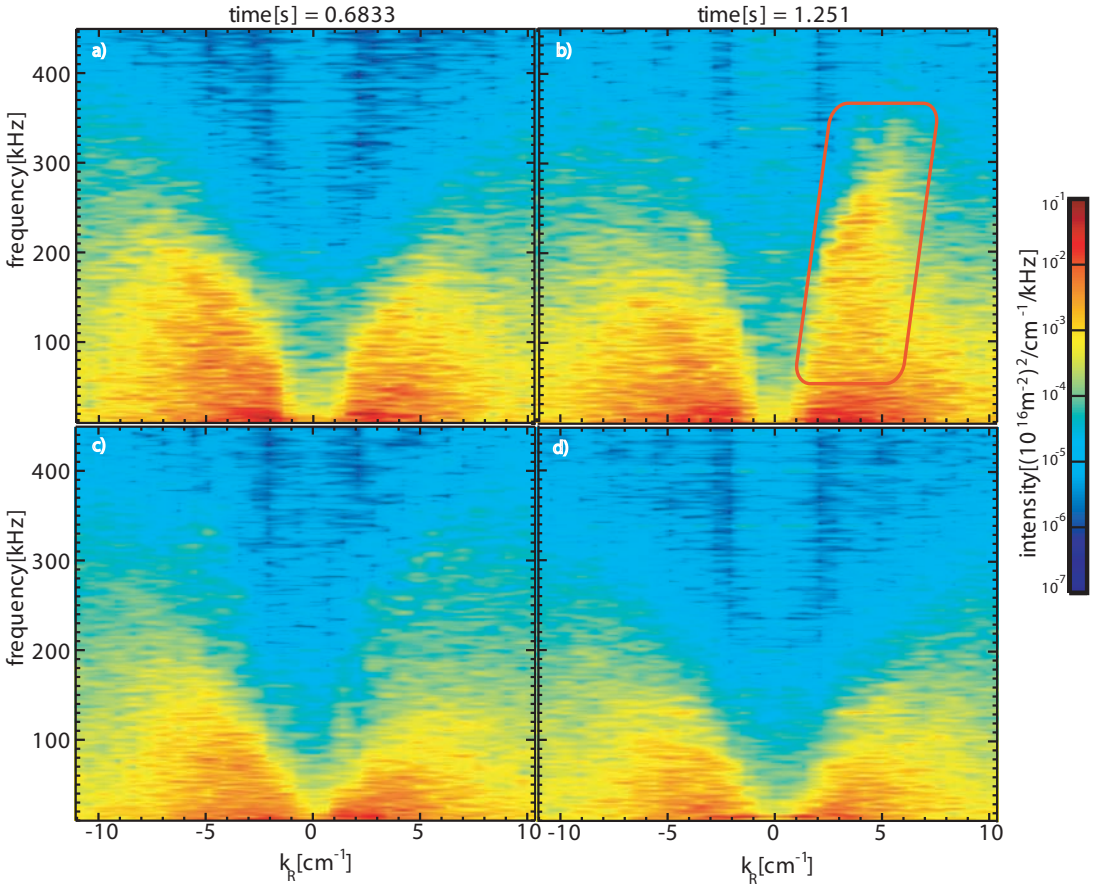

Figure 5-12: PCI turbulence spectra from 700 kA (a, b) and 350 kA (c, d) LSN discharges. Left columns correspond to turbulence prior to the LHCD phase and right columns correspond to turbulence ∼450 ms after the turn on of the LHCD. The highlighted area shows the turbulence feature observed on the counter-current rotation change LHCD plasmas.

5.5.2 Gyrokinetic Simulation of LHCD Profiles

In order to understand the turbulence modes in the plasma and relate it to the intrinsic rotation changes, a similar method as that described in Chapter 4 is used. The high and low current cases were focused on in order to bracket properly the turbulence behavior in upper and lower single null, and this method has primarily

used GS2 linear simulations.

The full profiles of the discharges along with the commonly shown turbulence driving terms (a/L_n and a/L_T) are shown in Figures 5-13 and 5-14. It was seen that when lower hybrid current drive turns on, there are, as expected, changes in the T_e, since the waves are damping on the electrons. There are also observed changes in the electron density distribution between the low and high current cases. These profile changes may cause major differences in the turbulence spectra in the plasma, which had been observed in the PCI spectrum. Furthermore, MSE provided q-profiles were used during these simulations to account properly for the effect of the current profile modification from LHCD. In Figure 5-14, there are errors with the EFIT reconstruction as imported to the HiReX Sr inversion, so the HiReX Sr profiles around r/a=0.5 have large errors. TRANSP processing is used to remove these errors in the simulations below.

Linear simulations of the high and low current upper single null discharges were performed. These simulations focused on low k instabilities because of the quasilinear approximation for transport depending on $\gamma/\langle k\rangle^2$. The normalized wavenumber $k_\theta\rho_i$ was restricted to 0.0-0.5 in these simulations, which is where, on many of the discharges, it was observed that there was a local maximum in the growth rate. An example growth rate and frequency plot versus normalized wavenumber is shown in Figure 5-15. At high k, there are also often observed local maxima, but these generally occur at $k_\theta\rho_i \sim 40$, which is significantly into the electron thermal gradient (ETG) turbulence range and is unlikely to cause major transport (more detailed plots of these modes are shown in Appendix B). The linear most unstable mode calculations for high and low current, both before and during the LH phase, are shown versus r/a in Figures 5-16 and 5-17. As is seen, the instabilities in the pre-LHCD phase are primarily in the ion direction and are at mid-to-high radii. When the LHCD turns on, however, the unstable modes move to lower radii and switch to the electron diamagnetic direction. This suggests that the turbulence is changing from ITG dominated to electron mode dominated. The low current case does have an ion directed lobe at low radii, but this may be due to the uncertainties in the profile fitting. The move

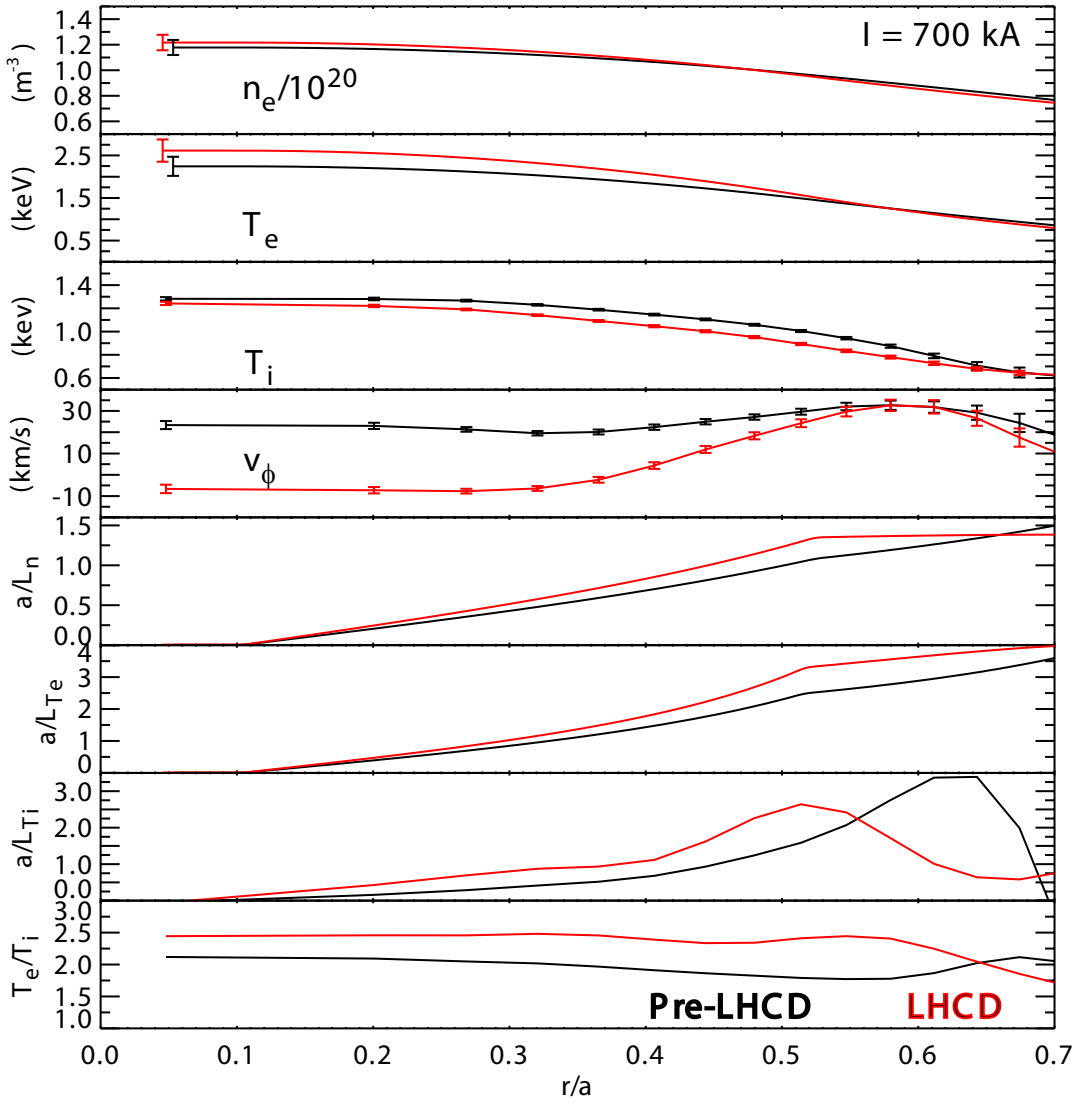

Figure 5-13: Plots of profiles of electron density, electron temperature, ion temperature, and plasma velocity, as well as the various drive terms for turbulent modes during the high current LHCD case. Black curves are for data which are pre-LHCD and red lines are for data during LHCD. Characteristic statistical error bars are shown in the top four graphs and removed for clarity for the bottom graphs.

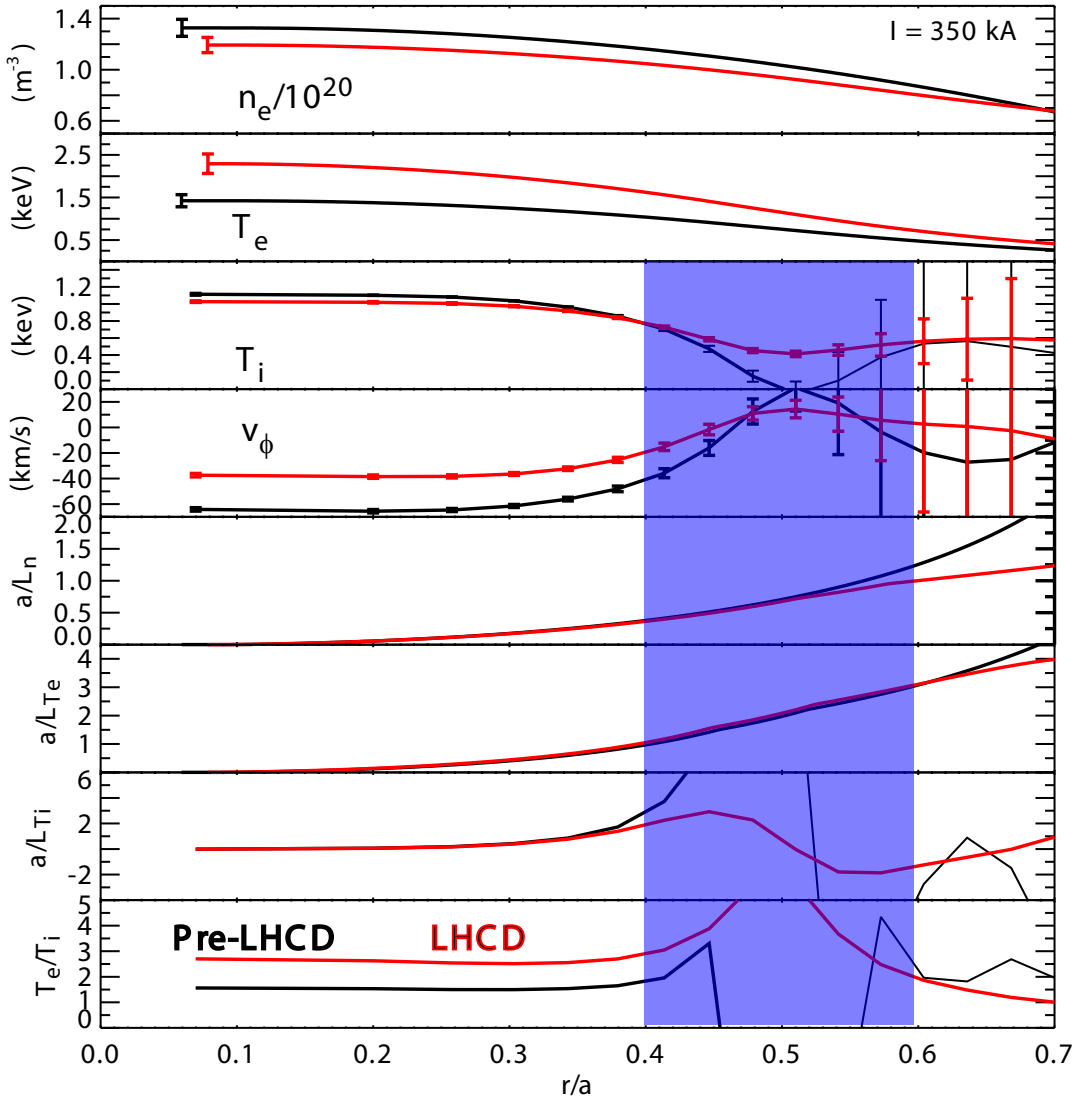

Figure 5-14: Plots of profiles of electron density, electron temperature, ion temperature, and plasma velocity, as well as the various drive terms for turbulent modes during the low current LHCD case. Black curves are for data which are pre-LHCD and red lines are for data during LHCD. Characteristic statistical error bars are shown in the top four graphs and removed for clarity for the bottom graphs. Note that at r/a ~ 0.5 the T_i and v_ϕ profiles are not as dependable due to the low current interfering with the EFIT reconstructions; those areas are highlighted in blue.

to TEM is consistent with the Ohmic rotation reversals for the co-current phase, but it is not consistent in the counter-current phase. Furthermore, a calculation was run with a simulated hot electron population, as LH heating is expected to generate, but this did not have any affect on the instability results and was not included in these simulations.

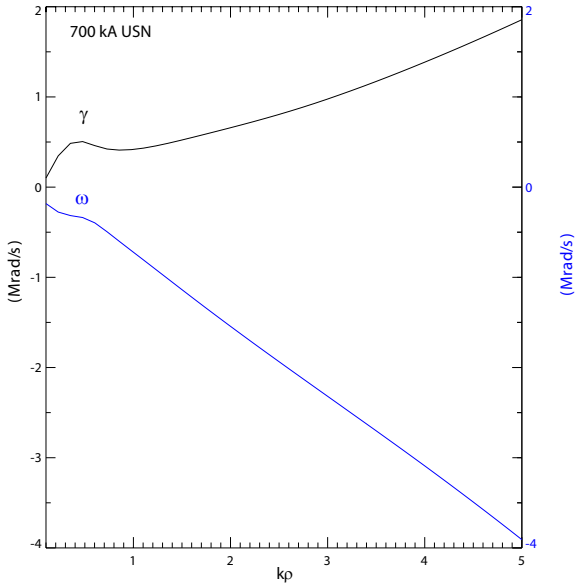

Figure 5-15: Example plot of linear instability versus normalized wavenumber as calculated by GS2 during a high current LHCD discharge in USN.

It is notable that in Figure 5-16, the linear frequency of the instability is ∼200 krad/s, and the asymmetric turbulence seen in Figure 5-12 is also in that range. It appears that both the high and the low current case have an electron directed instability appearing in the LHCD phase of the discharge. This suggests that LHCD is destabilizing the trapped electron mode when it turns on. From the Ohmic rotation reversal research, comparing LOC to SOC confinement, there is an empirical observation that in TEM dominated plasmas, the plasma rotation is in the co-current direction, while in ITG plasmas, it is in the counter-current direction. Therefore, these observations suggest that there should be turbulence differences observed between the low and the high current cases.

By fixing a point at the most unstable radial location in the unstable mode plots, the sensitivity of this mode to changes in plasma parameters has been tested. Specif-

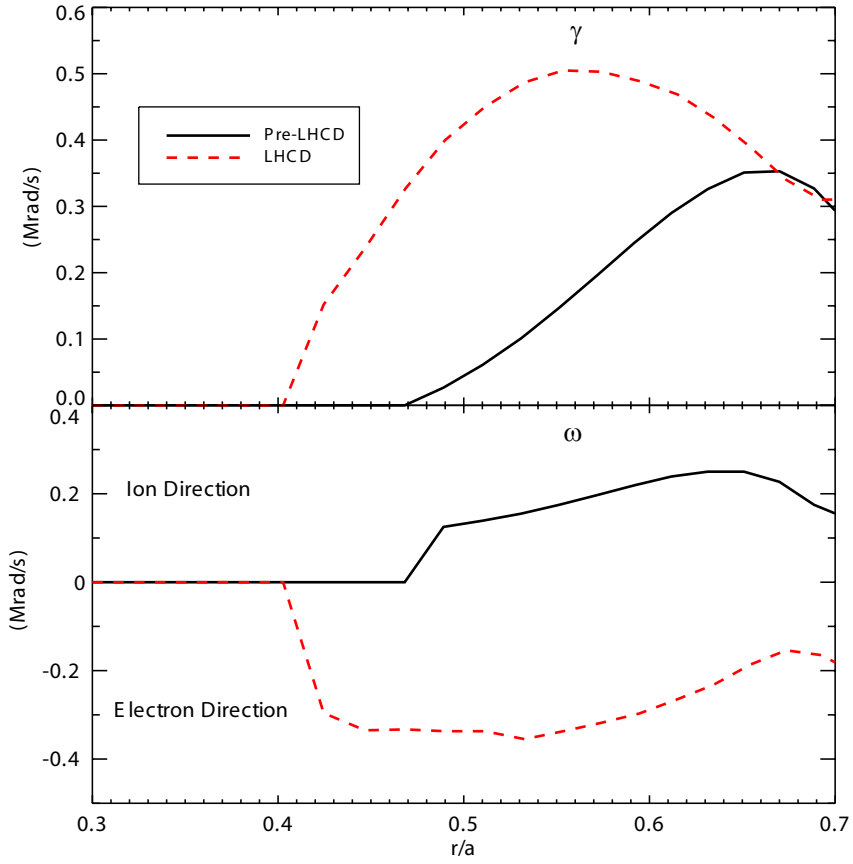

Figure 5-16: Linear GS2 calculations of the most unstable mode versus normalized radius in a 700 kA discharge with LHCD.

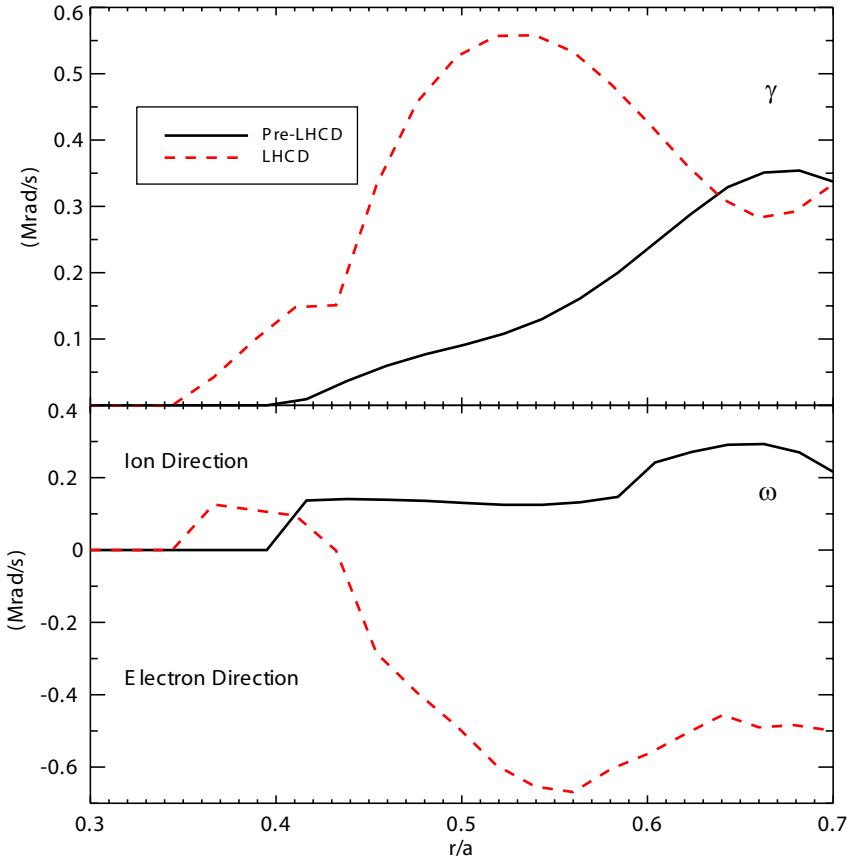

Figure 5-17: Linear GS2 calculations of the most unstable mode versus normalized radius in a 350 kA discharge with LHCD.

ically the terms a/L_n, a/L_{T_E}, a/L_{T_i}, T_e/T_i, q, $\hat{s}$, ν_e, ν_i, Z_{imp}, and n_{imp} were scanned over a broad range for both cases. It is unphysical to change some of these terms while keeping the others fixed, but this was still performed in order to identify the type of instability in these cases. Plots of growth rate at these varying parameters are shown in Figures 5-18 and 5-19.

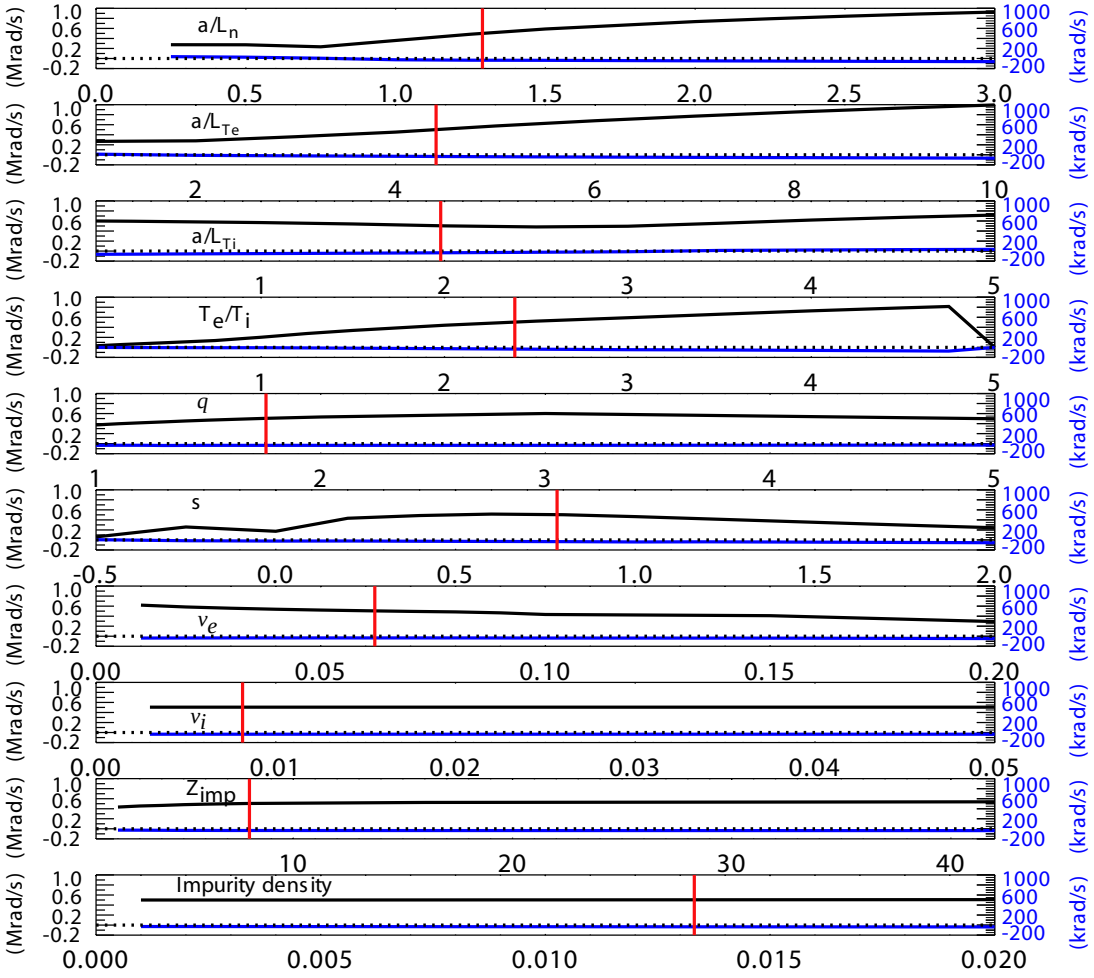

Figure 5-18: GS2 linear sensitivity of the most unstable mode at r/a = 0.5 at 700 kA to various changing parameters. Black lines correspond to growth rates and blue lines are for frequency. Negative frequency represents electron diamagnetic direction. Red vertical line is the experimental value of the parameter.

It is seen in the sensitivity studies that the growth rate profiles in both the low and the high current cases have similar parametric dependences. Both low and high current turbulence profiles are mostly independent of Z_{imp}, n_{imp}, and ν_i. They are

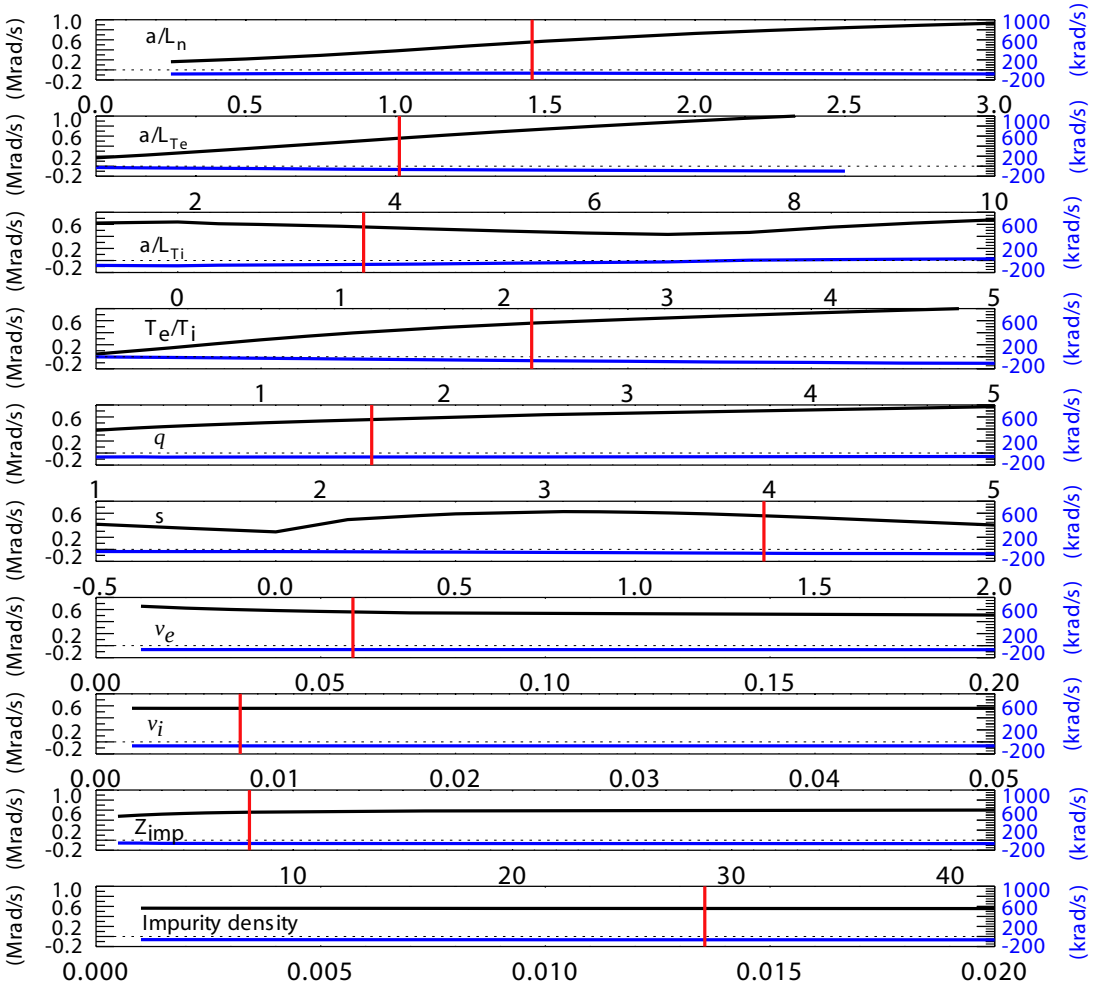

Figure 5-19: GS2 linear sensitivity of the most unstable mode at r/a = 0.5 at 350 kA to various changing parameters. Black lines correspond to growth rates and blue lines are for frequency. Negative frequency represents electron diamagnetic direction. Red vertical line is the experimental value of the parameter.

dependent in the same fashion on a/L_{T_E}, q, T_e/T_i, ν_e, and s. The two parameters where there are marked differences in the spectra are a/L_n and a/L_{T_i}.

It is observed that in the high current case, in the density gradient dependence plot, the changeover (the location where the modes switch from the electron to the ion direction) to ion directed (or ITG) turbulence occurs far more closely to the operational point than it does in the low current case. These plots were generated at r/a$\sim$0.5, and there are some errors in the density gradient from the profile fitting, therefore, it is conjectured that the actual turbulence at high current has an ITG component. It is expected that the ITG dominated modes, based on arguments about rotation reversals, would rotate in the counter-current direction. This argument is consistent with the lower hybrid current drive rotation results. For comparison, at low current, the dependence on density gradient is still strong, but there is no changeover to ion directed modes observed. Characteristic instability plots of γ and ω versus $k\rho$ are shown in the ion directed and electron directed cases in Figure 5-20.

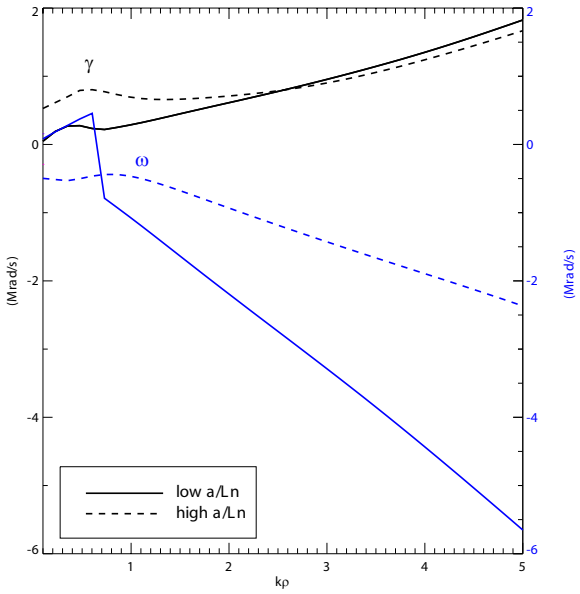

Figure 5-20: Example instability profiles of growth rate and frequency in the low a/L_n (solid lines) and high a/L_n (dashed lines) cases. Blue color refers to frequency and black color refers to growth rate.

The dependence on the gradient of the ion temperature is less clear than that of the density gradient. The high current case, once again, has an ion direction

changeover in the turbulence dependence at very high ion thermal gradient. In the low current case, this changeover is not observed, and this is consistent with high current plasmas being closer to the ITG threshold, thus developing counter-current rotation.

Overall, these simulations provide supporting evidence to the assertion that the primary effect of the Lower Hybrid Current Drive, with respect to rotation, is to modify the density and temperature profiles, thus destabilizing the density gradient driven TEM. The high current plasmas, however, may remain in the ITG regime over a large portion of the plasma volume with an increased drive term, and, thus, have a change in rotation in the counter-current direction. The low current plasmas fully transition to the TEM regime and their change in rotation is in the co-current direction.

5.6 LHCD Rotation relation to ECH

Another area of rotation that has been analyzed in the past is the rotation driven by the electron cyclotron heating (ECH) which have also been seen to cause bi-directional rotation similar to LHCD [4, 96]. It was seen that in co-current directed neutral beam plasmas on JT-60U, the ECH rotation changes were in the counter-current direction, while in the counter-current neutral beam plasmas, the rotation was in the co-current direction. Furthermore, DIII-D had seen strong counter current driven rotation from ECH in H-mode plasmas. The JT-60U group proposed that these rotation changes were due to the induced changes in the pressure gradient in the plasma, from the ECH injection. A summary of the JT-60U results is shown in Figure 5-21.

This observation of bi-directionality of the rotation from ECH is similar to the LHCD rotation reversal, but the ECH systems were run with a minimum of current drive to avoid complications of the heating and current drive physics. The primary difference seen in the profile changes at JT-60U was the ion and electron temperatures. In fact, in the core of the plasma, which was the primary area of ECH deposition, the ratio changes from approximately 1.0 to 1.2. This 20% change in the ratio of T_e

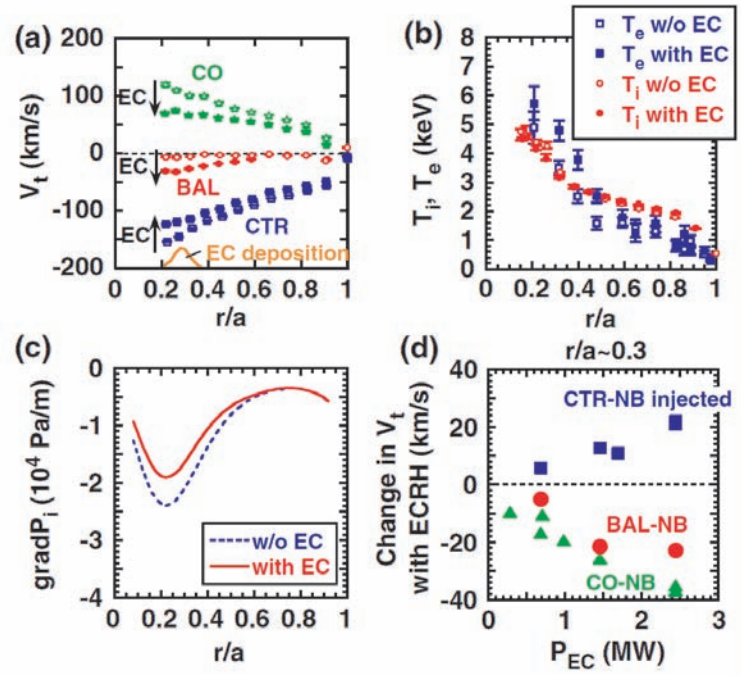

Figure 5-21: ECH rotation results from JT-60U. (a) The toroidal rotation changes with co-current, balanced, and counter-current neutral beams due to ECH. (b) The electron and ion temperature profiles from ECH. (c) Pressure gradient changes from ECH. (d) Change in velocity at r/a$\sim$0.3 as a function of of ECH power. Figure from [4].

to T_i is similar to the one seen in the high current LHCD case. Overall, it would be interesting to see if the ECH rotation follows a similar current dependence to what has been observed at Alcator C-Mod.

5.7 Summary

LHCD induced rotation changes have been observed for the first time in both the co- and counter-current direction in a tokamak. There is a strong plasma current dependence and a magnetic configuration dependence appears to exist as well. High current discharges have rotation changes in the counter-current direction, while low current discharges develop an acceleration in the co-current direction. These observations reconcile the differences in LHCD rotation results between Alcator C-Mod and other tokamaks.

Various theories have been proposed to explain these rotation results. From the new C-Mod results, the explanations of ripple losses of fast electron and convective velocity pinches can be discounted as they do not explain the new rotation results. A new explanation was developed relying on the observation of Ohmic rotation reversals and intrinsic rotation changes in a plasma. It was seen that there were turbulence changes between the co- and counter-current rotation cases and gyrokinetic simulations identified these changes as consistent with a move toward the critical changeover from density gradient driven TEM to a ITG dominated plasma. These results are consistent with the primary rotation driver during the LHCD results not being actual LHCD input of momentum, but rather being LHCD induced modifications of the profiles, thus leading to changes in the intrinsic rotation.

Given LHCD's presence in many future reactor designs and the importance of rotation for reactor transport and predictability, this work helps to predict the plasma behavior in a reactor setting. Reactors will generally operate at low q-values, and the high current C-Mod results are run at reactor-relevant $q \sim 3$. These results should be accounted for in any reactor scheme seeking to predict plasma behavior with LHCD present. Since plasma rotation has been seen to be important for H-mode access,

this is particularly fusion energy relevant. Steady H-modes generally benefit from co-current rotation, whereas these results show that LHCD will drive counter-current rotation instead. The densities used here are well below those for reactor relevance, but this is an issue of the LHCD accessibility. Overall, these results are important from a physics stand-point, since they provide another way of controlling the rotation profile in a plasma without the use of neutral beams or external coils, thus giving another knob for control of the plasma in a tokamak.

Chapter 6

Source Modeling

Using the "Toy Model" of rotation described in Section 2.3 and incorporating a full rotation profile, it is possible to model various rotation changes in a plasma. This chapter focuses on the applications of the "Toy Model" to SSEP sweeps, H-modes, and I-modes. This chapter should be taken as a series of examples of the "Toy Model", highlighting its flexibility, rather than a conclusive statement about the various plasma transitions.

6.1 SSEP Sweeps

A simple rotation change to model is one in which only the edge condition changes, while most of the plasma profiles, such as density and temperature, remain fixed. It has been conjectured that such a transition is caused by changing the magnetic geometry of the plasma, which alters the edge scrape-off-layer (SOL) flows [97] that, it is believed, couple to the edge of the plasma and change the rotation through transport. By changing from upper to lower single null geometries (consequently changing the distance from the primary to secondary separatrix, defined as SSEP, from positive to negative) while keeping all other parameters fixed, it is possible to study this case of momentum transport. In the rest of this chapter, this change is referred to as an SSEP sweep.

In this transition, the profiles of density and temperature do not change signifi-

cantly from the LSN to the USN case. The time traces of current, density, temperature, and SSEP are shown in Figure 6-1 for a discharge which switched from LSN to USN at 0.70 s and back to LSN at 1.00 s. The rotation during this transition, however, changed drastically. Rotation time traces at various radii are shown in Figure 6-2. These traces demonstrate the diffusion of the rotation into the core of the plasma: outer radii change first followed by inner radii. Characteristic profiles in USN and LSN are shown in Figure 6-3; the errors on rotation start increasing dramatically around r/a=0.6 due to decreased X-ray signals.

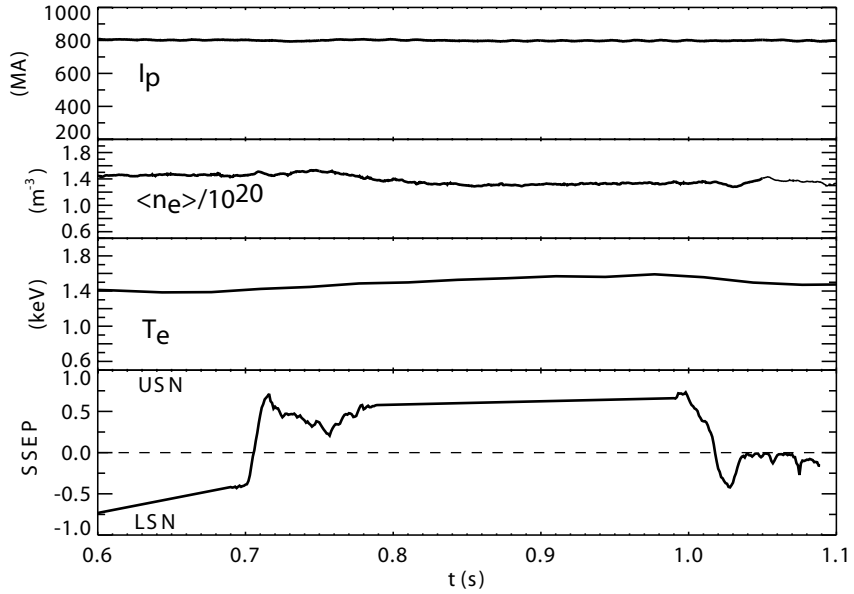

Figure 6-1: Time traces of plasma current, line averaged density, central electron temperature, and SSEP during an SSEP sweep. Note that the time traces of the density and temperature do not change significantly as a function of SSEP.

The Toy Model of rotation was applied to the SSEP profiles with pure diffusion (spatially and temporally unvarying), TRANSP diffusion and no pinch, TRANSP diffusion and Peeters pinch, and TRANSP diffusion and Yoon pinch. Characteristic diffusion and convection profiles are shown in Figures 6-4 and 6-5; note that because the plasma profiles do not change significantly from LSN to USN, the diffusion and convection profiles do not change significantly either. The Yoon convection has some discontinuities, particularly at outer radii, which make it difficult to use. These discontinuities occur because of the α_c term depending inversely on a function of the

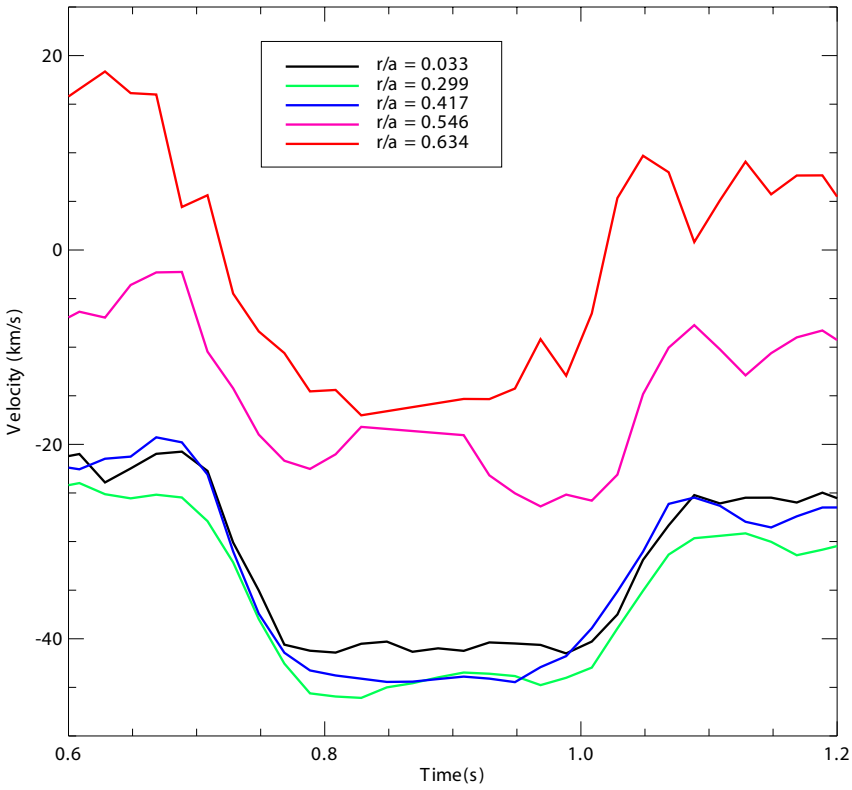

Figure 6-2: Time traces of rotation at several r/a for an SSEP sweep discharge.

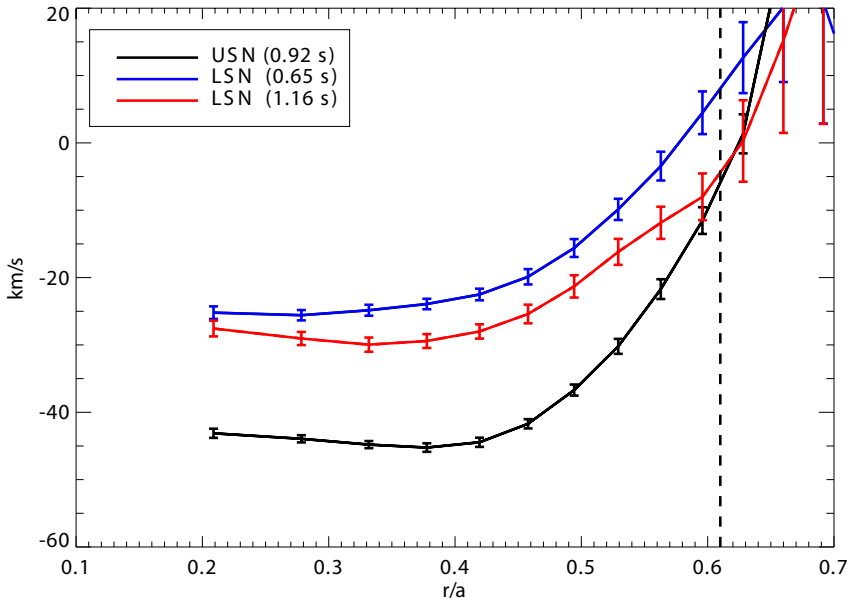

Figure 6-3: Average rotation profiles in the LSN and USN case with characteristic statistical error bars shown. Vertical dashed line corresponds to position of q=3/2 surface.

temperature gradient scale length that can cross through a singularity.

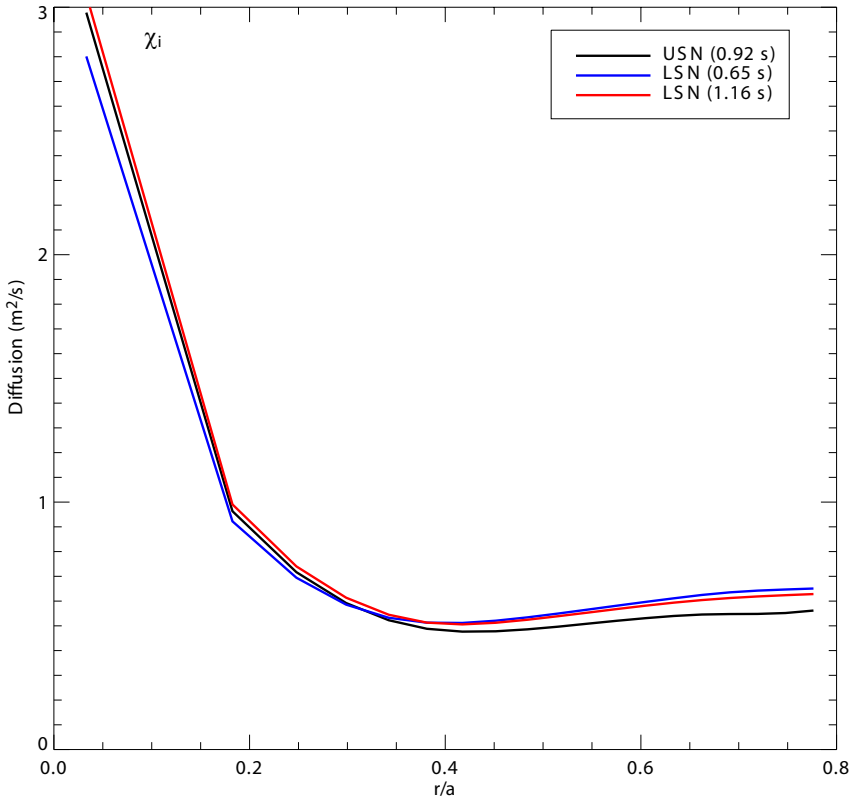

Figure 6-4: Average ion thermal diffusion values as calculated by TRANSP before and during an SSEP sweep. These values are taken as the momentum diffusion as well.

The source profiles for the SSEP case are shown in Figure 6-6 for the previously listed assumptions. Note that in all of this chapter the source is a force density and not a torque density, since this model is effectively a slab model. Because of the errors in the rotation profiles all of the source calculations are restricted to be within r/a=0.60. Irrespective of the form of the diffusion or convection used, the core source profiles have flat traces as a function of time. This means that in an SSEP sweep discharge, the rotation is fully explained by diffusion and convection in the core. There are also baseline source values appearing in the plots, and these exist in order to explain the noise in the data and a general offset from baseline that occurs because of errors in the diffusion and convection profile. At mid radii, however, there are temporal changes in the source profiles which appear in the USN case. These are not well correlated with the transition from magnetic geometry transitions and are suggestive of some

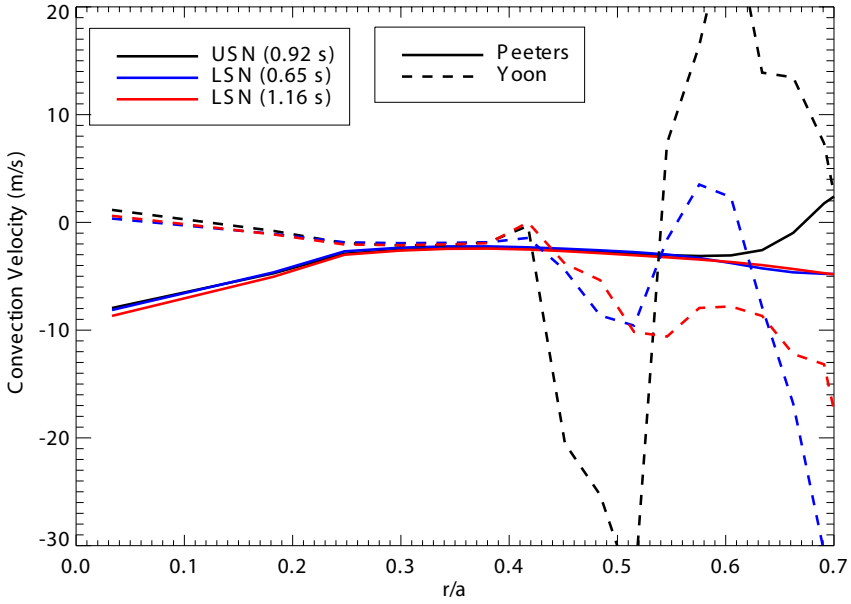

Figure 6-5: Average convective velocity values in the Peeters and Yoon form before and during an SSEP sweep. Three times are given because there are two LSN phases.

uncaptured momentum transport physics rather than an appearance of core source profile.

Characteristic radial profiles of the source in USN and LSN during the SSEP sweep are shown in Figure 6-7. Overall, the shapes of these profiles suggest that the source is explaining minor variation in the plasma rotation rather than a conclusive source profile itself, except at the outer channels where there exists a negative peak in the USN case. The differences between the LSN and USN source profiles, however, are fairly small.

The sensitivity of the "Toy Model" to its assumptions based on the shape of the diffusive and convective terms was tested using the SSEP case as well. Detailed results of these tests are shown in Appendix E. It is seen that, generally, the "Toy Model" source profiles are dominated by the rotation/temperature profiles and not by the variations in the diffusive and convective parameters.

A calculation of the Diamond and Yoshida forms of the residual stress for this plasma is shown in Figure 6-8. The Diamond form of the stress is fairly consistent with that calculated by the "Toy Model", without a convective term, but it slightly overestimates the size of the residual stress. The shape of the profile is captured

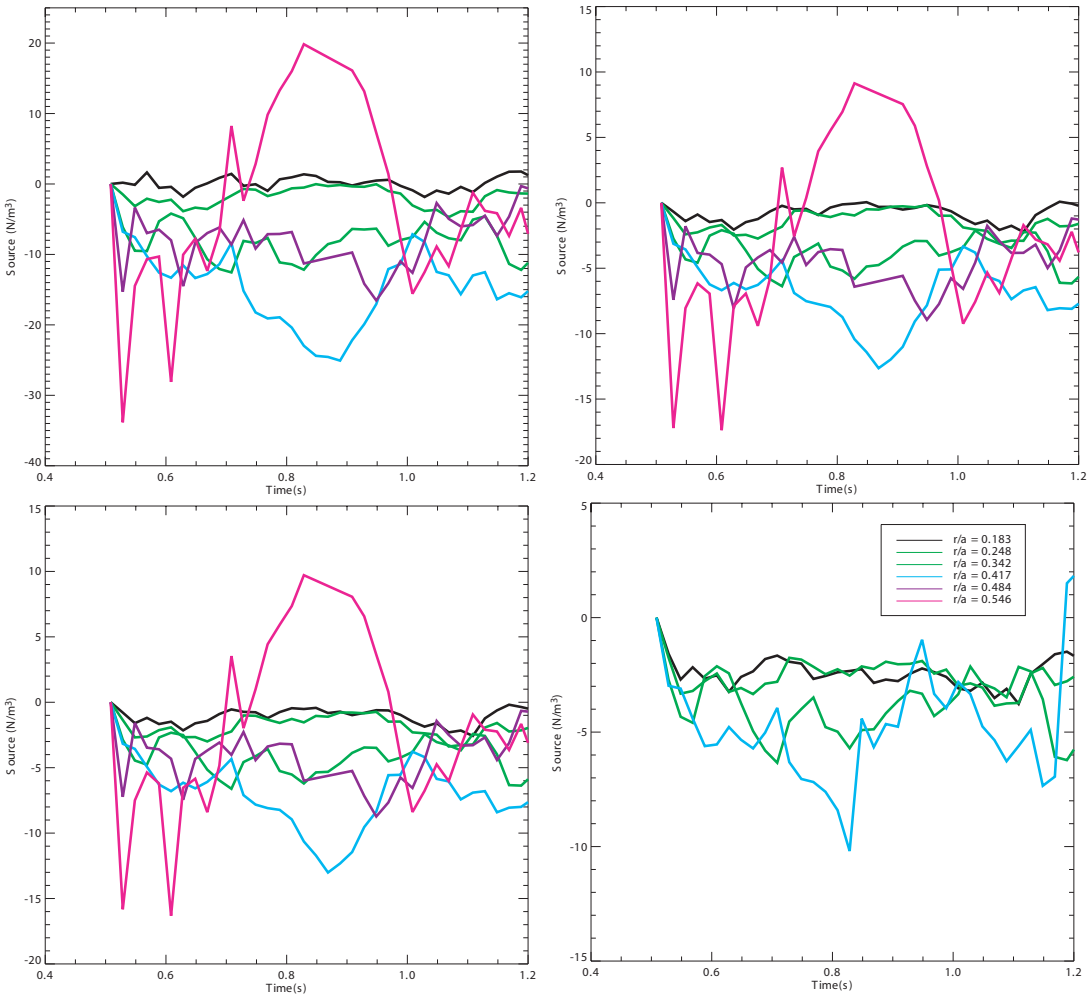

Figure 6-6: Time traces of source values at several r/a for SSEP sweep discharges. The graphs are source profiles calculated with [top left] a constant diffusion ($\chi = 1.0\ \mathrm{m}^2/\mathrm{s}$) and no convection, [top right] a TRANSP calculated diffusion and no convection, [bottom left] a TRANSP calculated diffusion and Peeters convection, and [bottom right] a TRANSP calculated diffusion and Yoon convection.

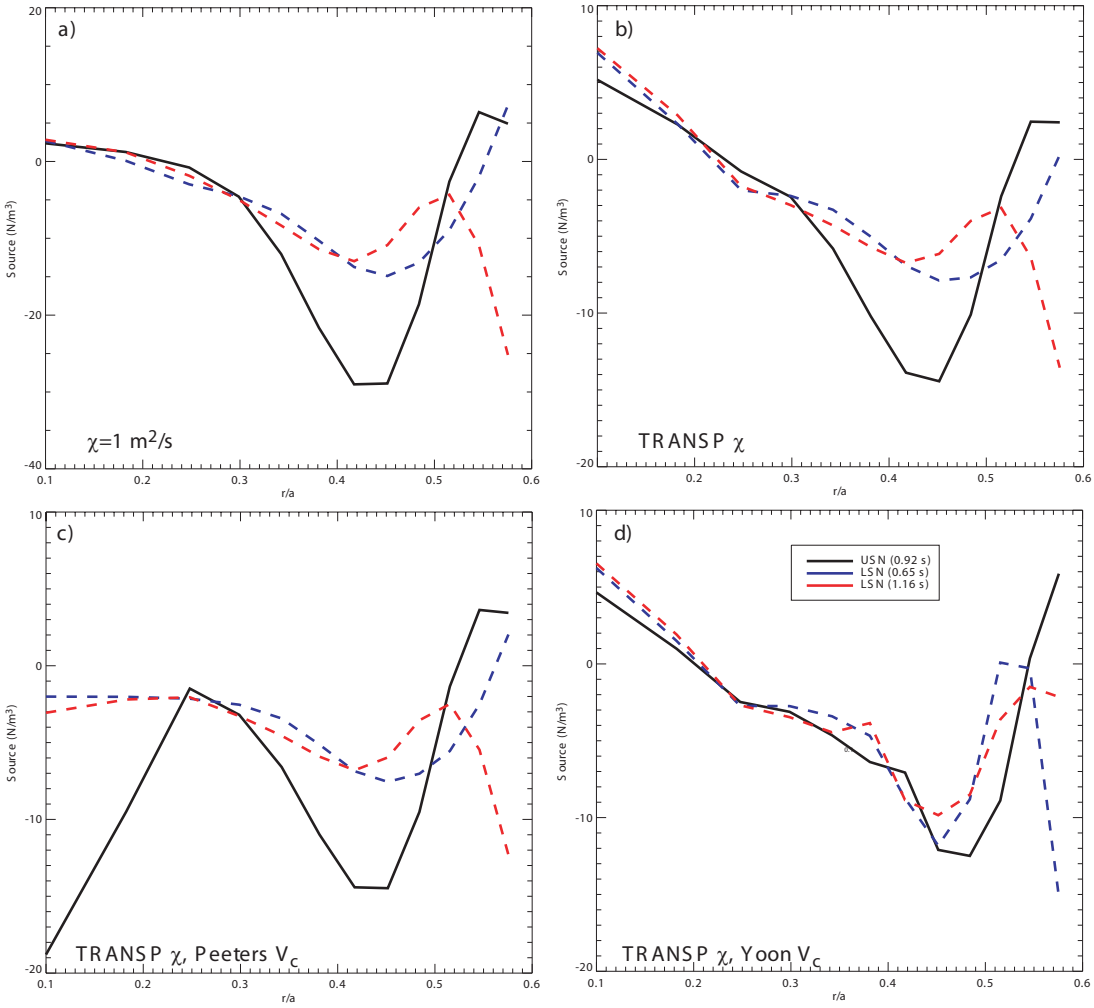

Figure 6-7: SSEP source profiles using (a) a constant diffusion ($\chi = 1.0$ m^2/s) and no convection, (b) a TRANSP calculated diffusion and no convection, (c) a TRANSP calculated diffusion and Peeters convection, and (d) a TRANSP calculated diffusion and Yoon convection at characteristic LSN and USN times.

fairly well in LSN but not in USN. The Yoshida form is qualitatively similar to the Diamond form as well. In fact, the magnitude of the Yoshida form agrees well with the calculation without a convective term and is seemingly a superior model in this case. Note that the Yoshida form has a constant coefficient ranging from 1.0×10^{-7} to 3.0×10^{-7} m^{-1} s, and the extrema of the calculations are shown in the figure.

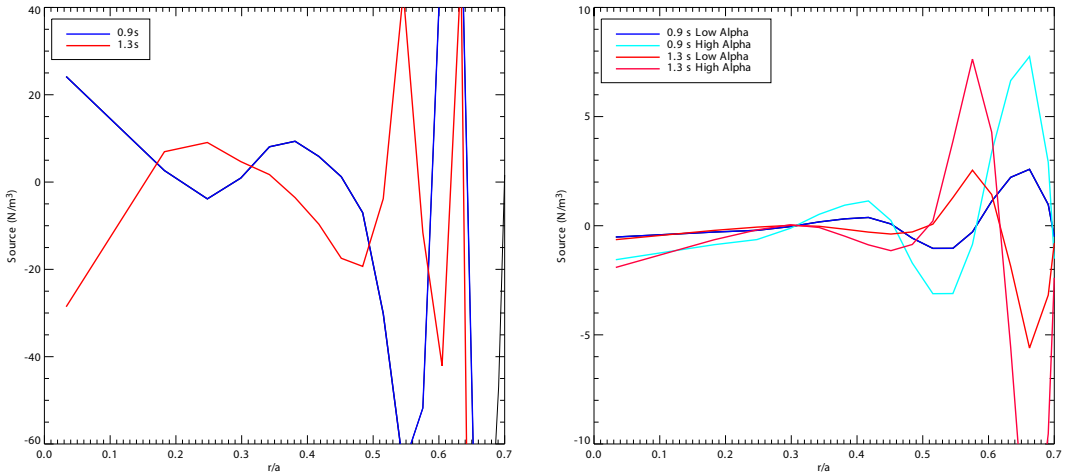

Figure 6-8: Calculation of the characteristic source profiles in a SSEP sweep as derived from the Diamond and Yoshida forms of the residual stress.

Despite the assertion that the SOL flows are the driver for the rotation change, there appear to be internal sources that need to arise off-axis in order to explain the rotation. There are small momentum sources near the core of these plasmas which agree fairly well with the Diamond and Yoshida residual stress calculations. Overall, the SSEP sweep is well characterized by the diffusive and convective models (particularly in the LSN phase of the discharge), and this implies that the "Toy Model" is a good characterization of the momentum transport in the plasma. Furthermore, the Yoshida model is qualitatively similar in both shape and magnitude to the calculated source profile.

6.2 H-modes

Another area of interest for rotation profile changes is the spontaneous rotation associated with Enhanced Dα (EDA) H-mode transitions. It has been observed that

when a plasma transitions into an EDA H-mode, it spontaneously spins-up in the co-current direction [98]. Characteristic time traces of an EDA H-mode are shown in Figure 6-9. During an H-mode transition, there is a marked increase in both temperature and density in the plasma, and in an EDA H-mode there is a drop in the Hα signal, a characteristic line seen from hydrogen in the edge of the plasma, associated with the transition as well. The density and temperature rise makes H-modes attractive operational modes for generating fusion power in a reactor, but issues still exist with impurity accumulation in the core plasma. It has been observed that during an H-mode transition, the rotation changes begin at the edge first and then transport to the core of the plasma. Example rotation time traces are shown in Figure 6-10. There is no external input of momentum, so all of these changes are spontaneously generated by the plasma itself.

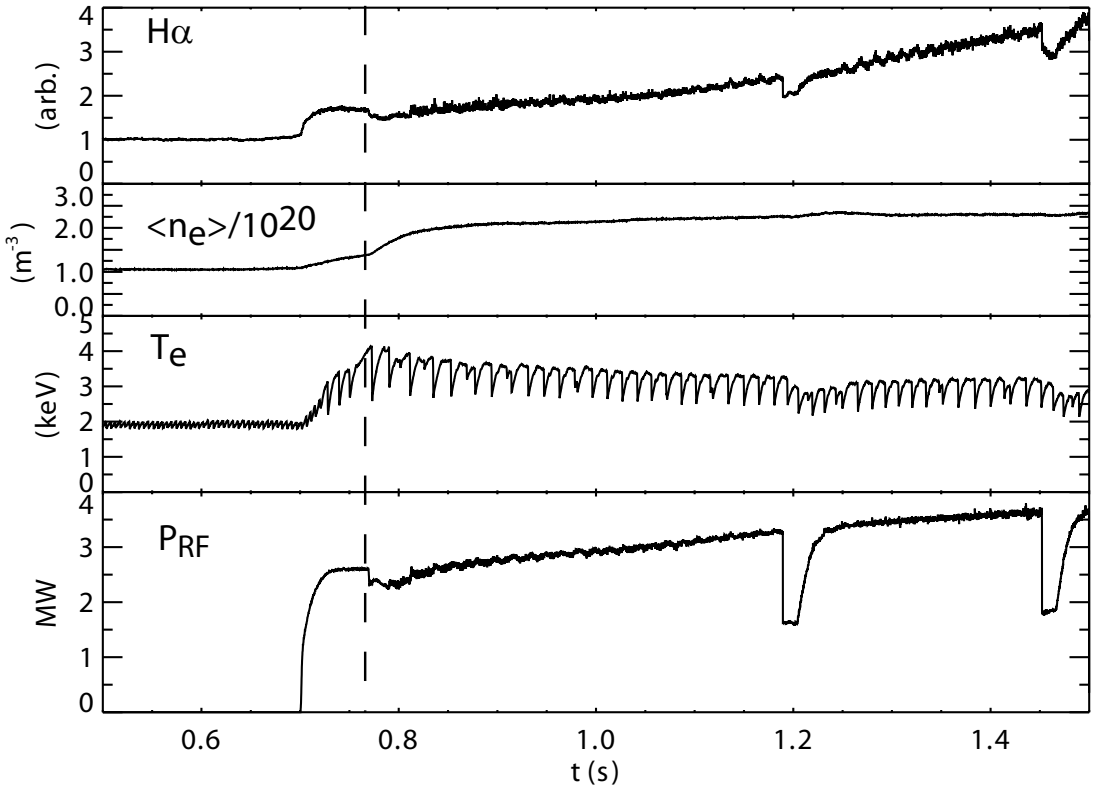

Figure 6-9: Time traces of Hα brightness, line averaged density, central electron temperature, and RF power during an H-mode transition.

Characteristic rotation profiles with statistical errors are shown in Figure 6-11.

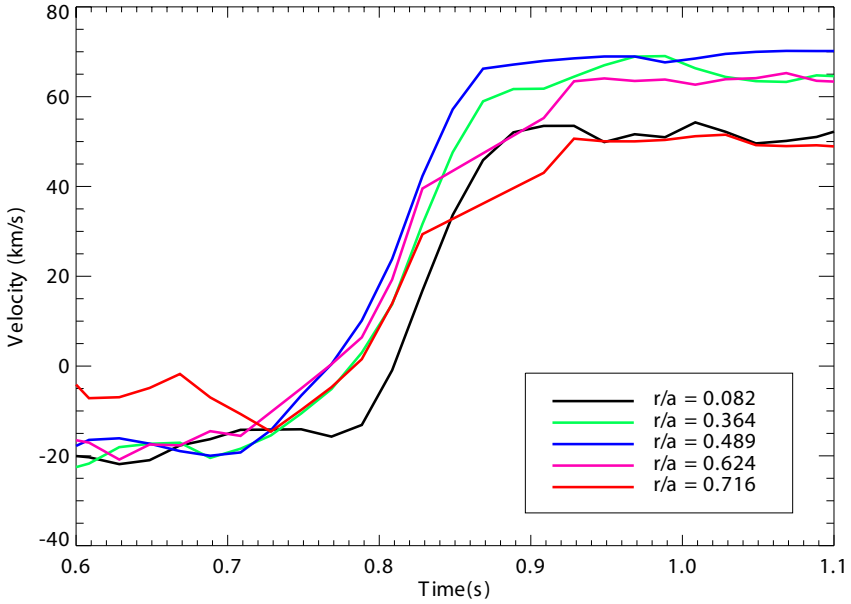

Figure 6-10: Time traces of rotation at several r/a for an H-mode transition. Note the outer part of the plasma rises before the inner section does.

Note that the L-mode rotation profile is very similar to those shown in the SSEP case, and the plasma is in a USN geometry. The H-mode profile is elevated at all radial locations, and the error bars decrease because of the higher temperature in the core which increases the photon count rate from the argon impurities in the plasma. Outside of r/a=0.8 the profiles are not usable because of the high error bars for an H-mode; for the L-mode the error bars are elevated at r/a$\sim$0.7, so many of the time traces of rotation and source profile are not usable outside of r/a=0.7. The somewhat sinusoidal behavior of the rotation in the L-mode case is not realistic, which is supported by the elevated error on that section.

The "Toy Model" of rotation was applied to the H-mode profiles with pure diffusion, TRANSP diffusion and no pinch, TRANSP diffusion and Peeters pinch, and TRANSP diffusion and Yoon pinch. Characteristic values of diffusion (effective total thermal diffusion is used) and convection before and during the H-mode are shown in Figures 6-12 and 6-13. The source profiles were calculated using the "Toy Model", and radial profiles are shown in Figure 6-14. Source time traces at various radii are shown in Figure 6-15. Note that with the implementation of the convective term, the source profile size generally decreases, implying that the convective term is improving

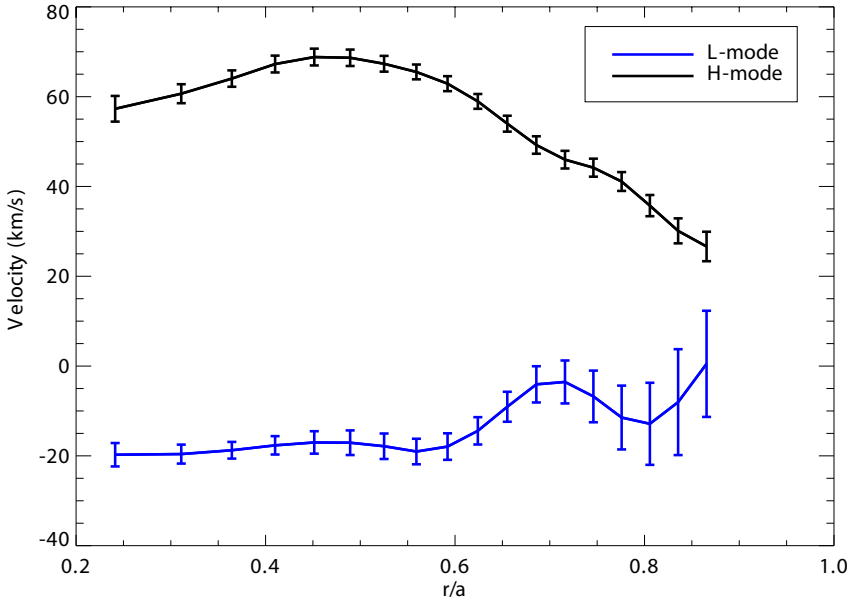

Figure 6-11: Average rotation profiles in the H-mode and L-mode case with characteristic statistical error bars shown.

the fits of the model to the plasma. Interestingly, the Peeters form of the convective term worsens the fit over a large area of the core plasma and the Yoon form improves the fit significantly except at the outer edges.

In order to simplify viewing these source profiles, they are shown in Figure 6-16 normalized to their maximum values. This figure is created by taking the average value of the source during the H-mode phase and subtracting from it the average in the L-mode phase (the core is not shown in this case for simplicity). It is seen that irrespective of the form of the diffusive/convective profiles taken, there is a peak in the source at r/a$\sim$0.5 because the pinch profiles are fairly flat at that radius, while the rotation profile has large gradients. This suggests that there is a physical mechanism driving rotation at that location. Example profiles of electron density, electron temperature, and ion temperature are shown in Figure 6-17 for the L-mode phase and the H-mode phase. As expected, each of these profiles increases during the H-mode since both temperature and density pedestals form during an H-mode.

Given the earlier discussion about the residual stress being proportional to the gradients of physical parameters, the actual driving terms are not well characterized by the profiles themselves. While the density and temperature change significantly

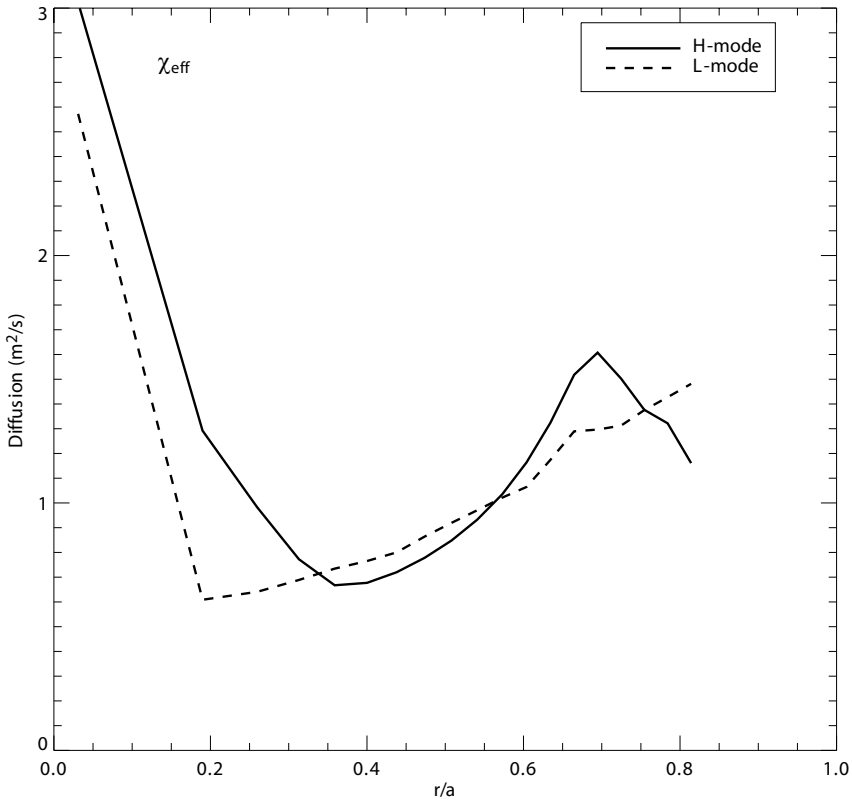

Figure 6-12: Average diffusion values as calculated by TRANSP before and during the H-mode transition. The effective total heat diffusion was taken for χ_ϕ in this case

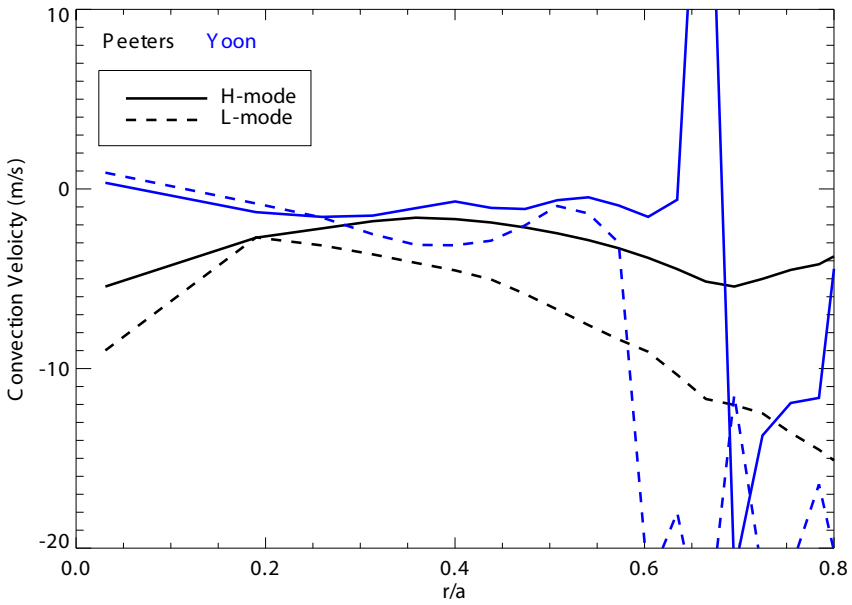

Figure 6-13: Average convective velocity values in the Peeters and Yoon form before and during the H-mode transition.

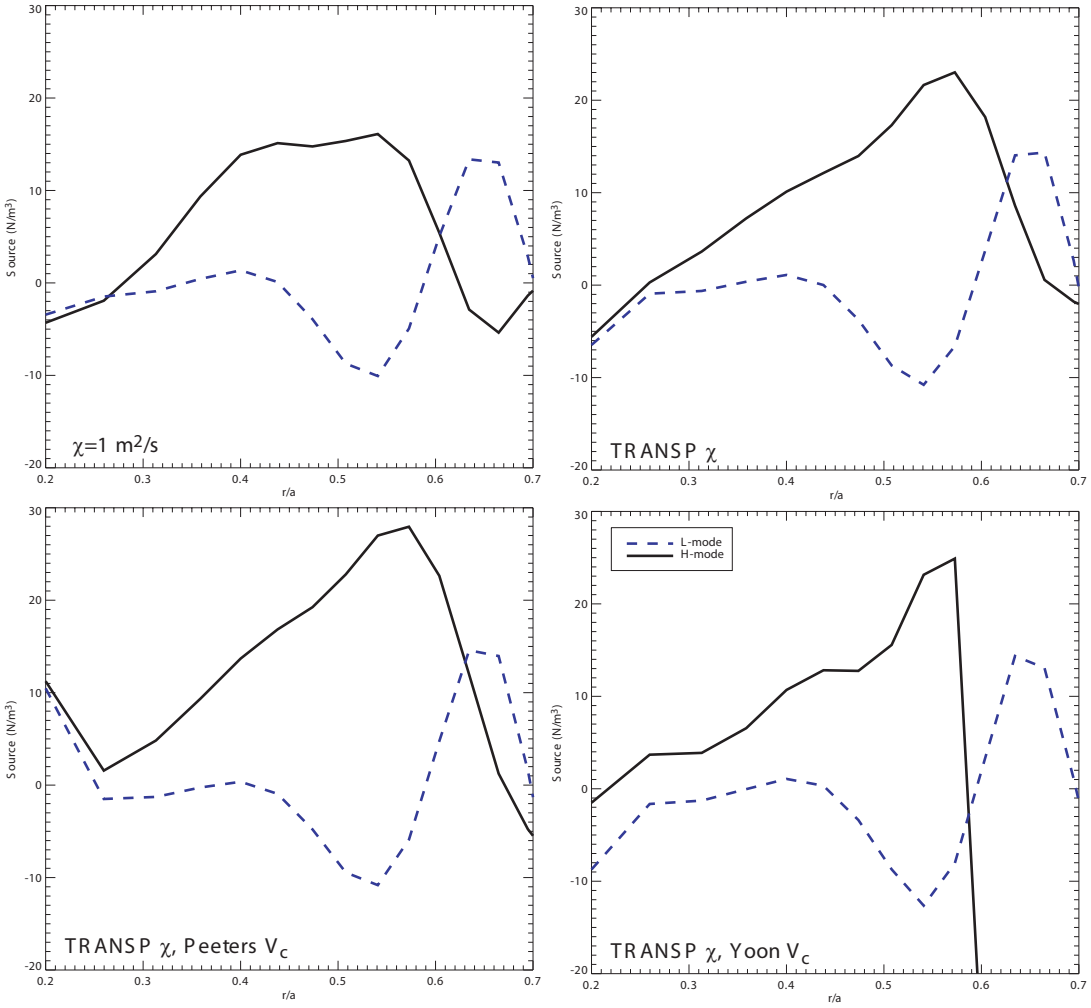

Figure 6-14: H-mode source profiles using constant diffusion ($\chi = 1.0\,\mathrm{m}^2/\mathrm{s}$), TRANSP diffusion and no pinch, and Peeters and Yoon convective values with TRANSP diffusive values at characteristic L-mode and H-mode times.

in the core plasma of an H-mode, the gradients of these terms can actually remain fairly similar. The normalized changes in the gradients of plasma density, electron temperature, ion temperature, and total pressure from the L-mode to the H-mode are shown in Figure 6-18. The changes in the electron temperature and plasma density are uncorrelated with the source profiles. The pressure gradient profile appears somewhat correlated, but the best correlation is with the change in the ion temperature profile. This suggests that the ion temperature gradient is the driving term for the rotation. The drive may be due to either the RF deposition or from the form of the residual stress (Equation 2.30), which is proportional to the temperature scale length L_T. The form of this residual stress also implies that secondary sources of momentum may be occurring during the H-mode besides the primary one at the edge. This correlates well with ITB rotation formation in a plasma, where steep temperature gradient changes have been seen to correlate with rotation shear [99, 100].

It has been seen that H-mode core rotation is proportional to the edge pressure gradient, and recently it was seen that the rotation is actually due to, as described below in Section 6.3, the edge temperature gradient. It is important to point out that these secondary sources which appear at r/a$\sim$0.5 are significantly below those at the edge of the plasma, even though both appear to be significant when plotted in their respective plasma regions.

Finally, the residual stress calculations for the Diamond and Yoshida forms were repeated for this H-mode case and are shown in Figure 6-19. In this case, the Yoshida calculation underestimates the required source to match the profiles at mid-radii. Both of the calculations do not reproduce the peak of the source moving outward in radii and spreading out as the plasma transitions into an H-mode.

6.3 I-mode

The I-mode regime was recently re-discovered at Alcator C-Mod [101]. This is an improved confinement regime with high temperature and energy confinement time but without an increased density or density pedestal. The impurity confinement

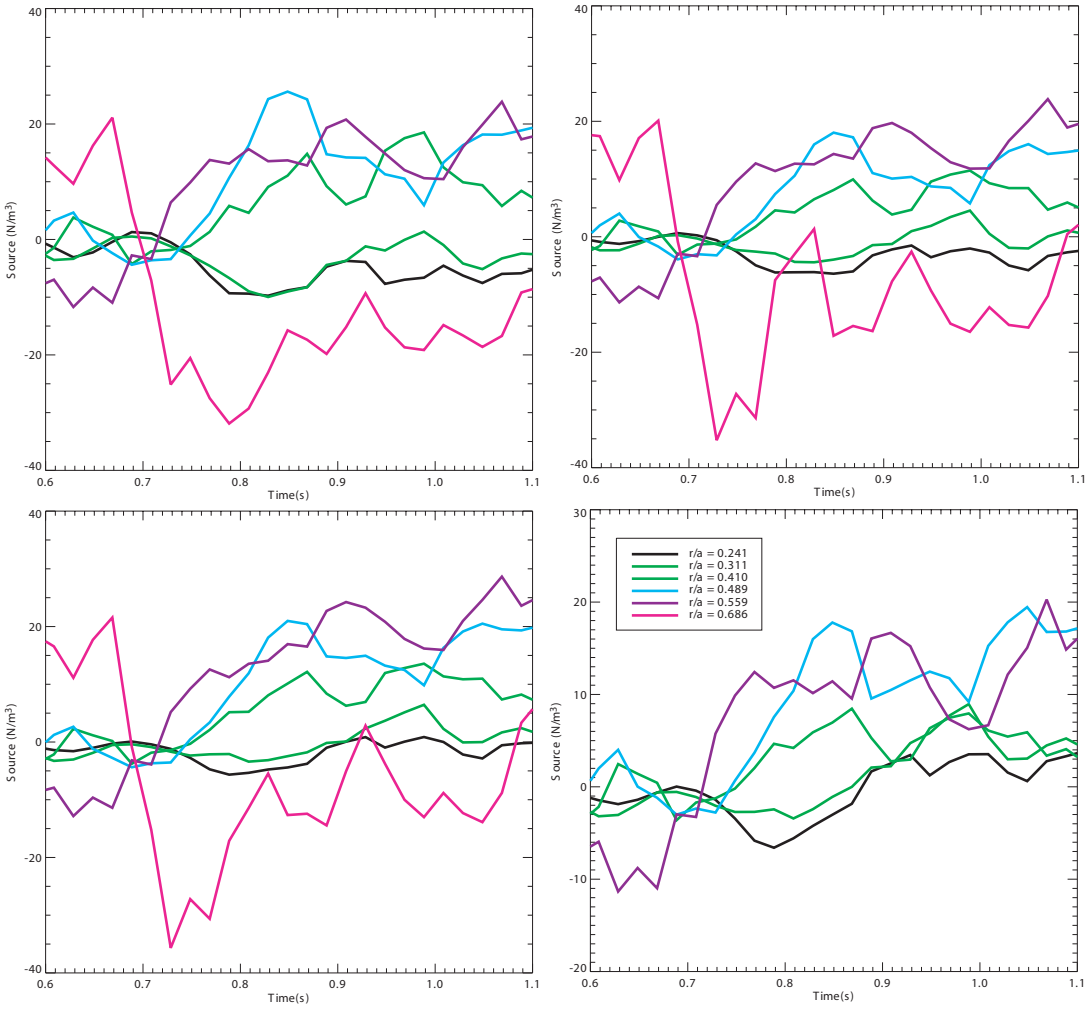

Figure 6-15: Source time traces in an H-mode at various radii with [top left] a constant diffusion ($\chi = 1.0$ m^2/s) and no convection, [top right] a TRANSP calculated diffusion and no convection, [bottom left] a TRANSP calculated diffusion and Peeters convection, and [bottom right] a TRANSP calculated diffusion and Yoon convection.

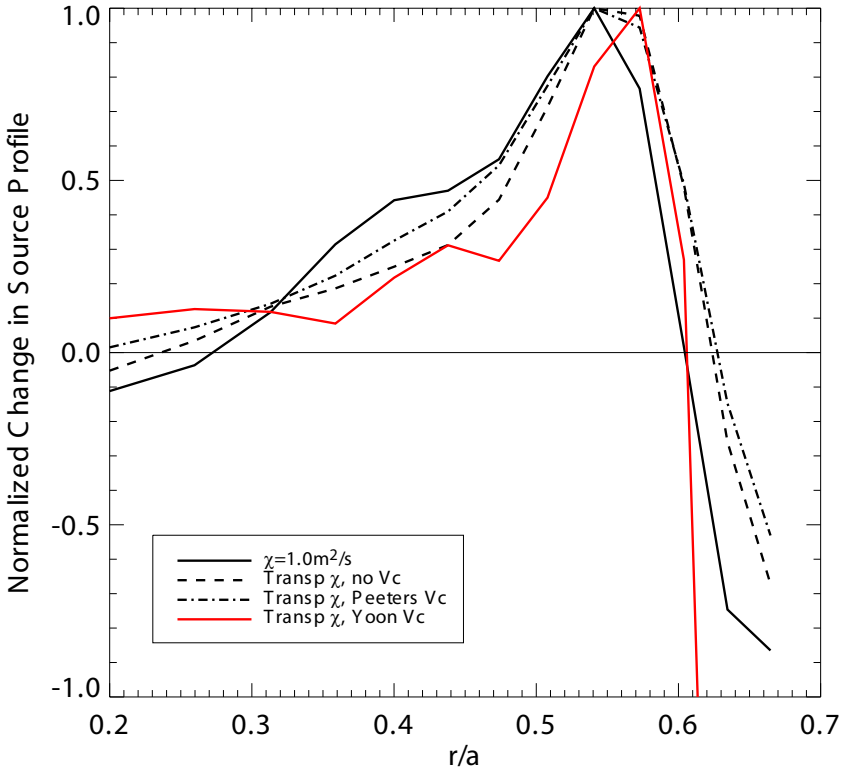

Figure 6-16: Normalized source profiles as a function of distance in an H-mode; core values are not included in this figure. Note that in all cases the source profile peaks at near the same radial positions, irrespective of diffusion and pinch forms.

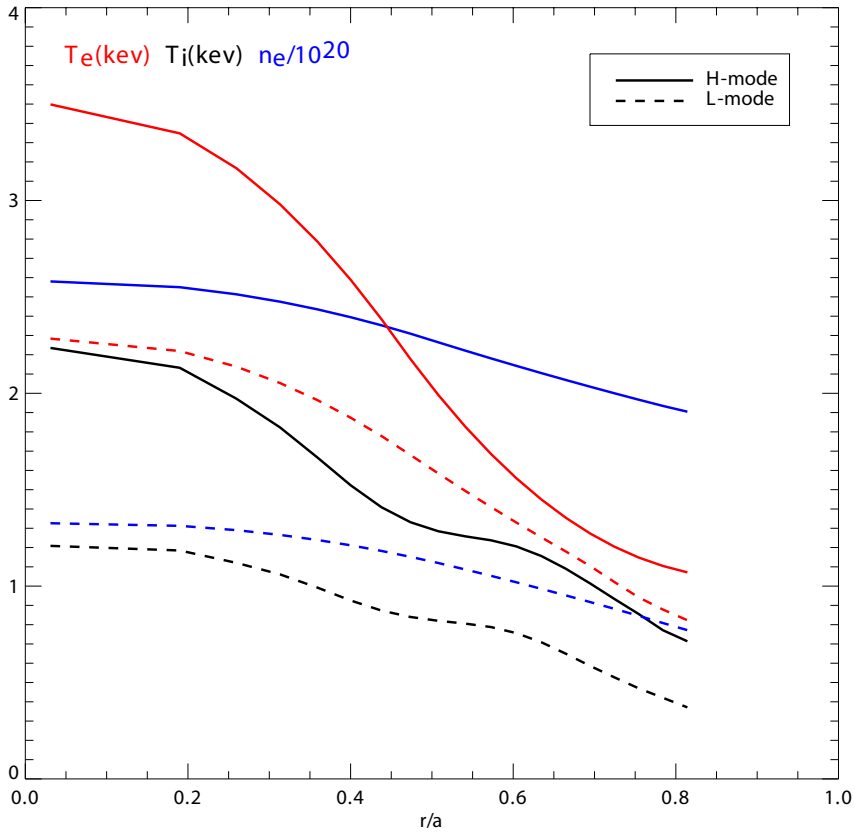

Figure 6-17: Ion temperature, electron temperature, and electron density profiles before (0.65 s) and during (1.11 s) the H-mode discharge.

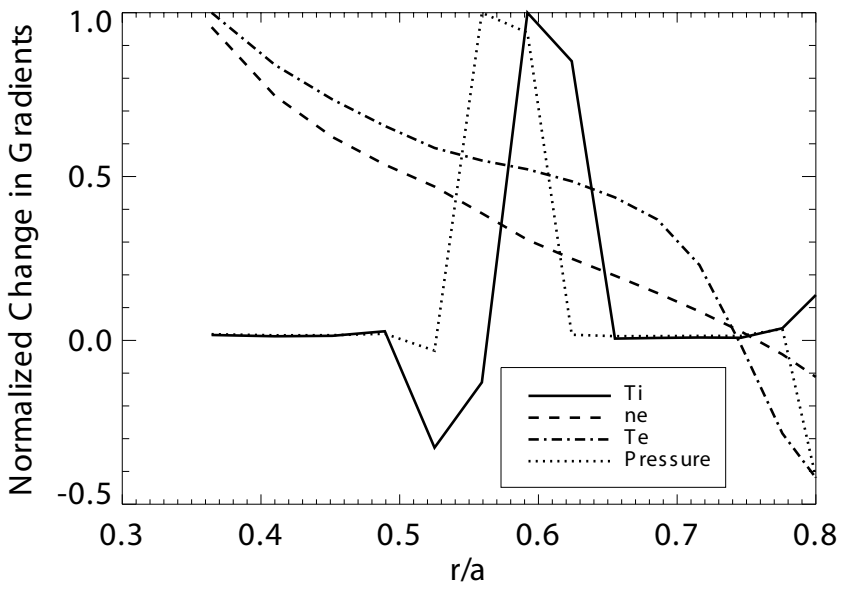

Figure 6-18: Normalized changes in the gradients from and the L-mode to the H-mode discharge.

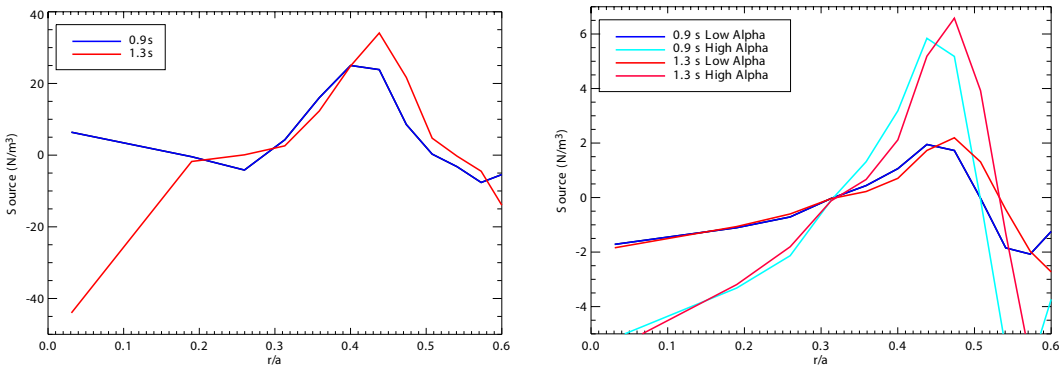

Figure 6-19: Calculation of the characteristic source profiles in an H-mode as derived from the Diamond and Yoshida forms of the residual stress.

time during an I-mode remains the same as that of an L-mode. This increase in energy confinement time with no increase in impurity confinement, as well as no edge localized modes (ELMs) and low collisionality, makes I-modes one of the most potentially advantageous operational regimes for fusion energy.

I-modes have been analyzed for their rotation behavior, and it has been seen that I-mode and H-mode regimes have similar rotation changes in the core of the plasma and, given that the only difference in these plasmas is the edge pressure pedestal, it was deduced that the rotation in H-modes and I-modes is proportional to the edge temperature pedestal gradients [102]. A time trace of characteristic plasma parameters in an example I-mode plasma is shown in Figure 6-20. The temperature of the plasma increases during the I-mode, but the density remains approximately at its L-mode value.

Example normalized rotation time histories (maximum rotation is defined as 1 and minimum rotation is defined as 0) of the I-mode are shown in Figure 6-21; it is seen that the rotation in an I-mode moves inward from the edge, similar to an H-mode. They are shown normalized to accentuate the I-mode's relation to the H-mode's rotation behavior.

Characteristic rotation profiles with statistical error bars are shown for the I-mode case in Figure 6-22. These profiles are elevated similarly to the H-mode case, and the total change in rotation is of similar magnitude as the H-mode scenario. The plasma is in USN in this discharge. Interestingly, the I-mode rotation appears to meet the

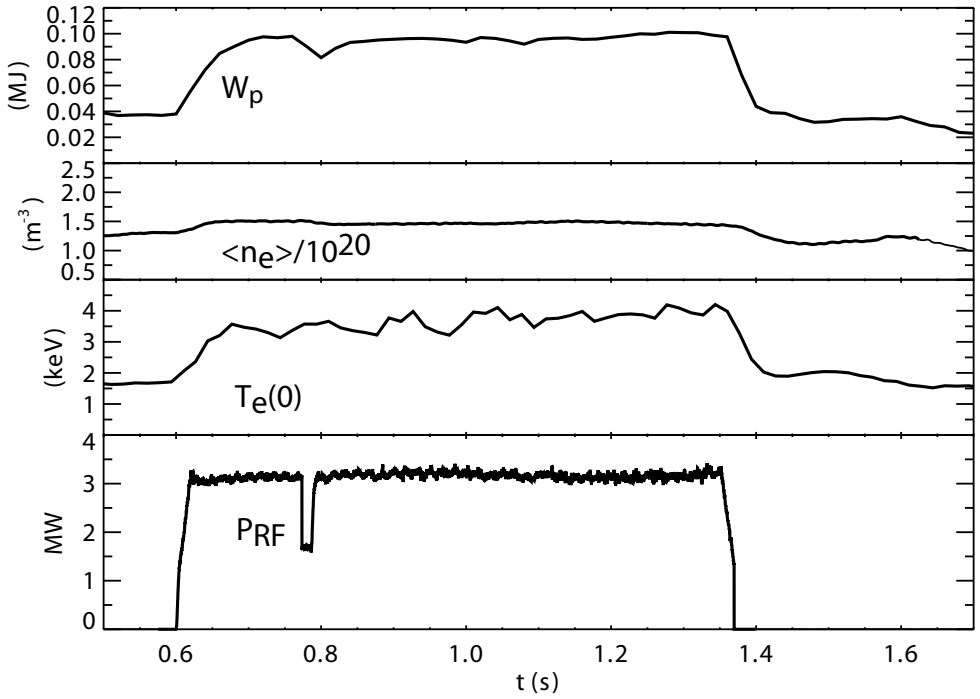

Figure 6-20: Time traces of stored energy, line averaged density, central electron temperature, and RF power during an example I-mode transition.

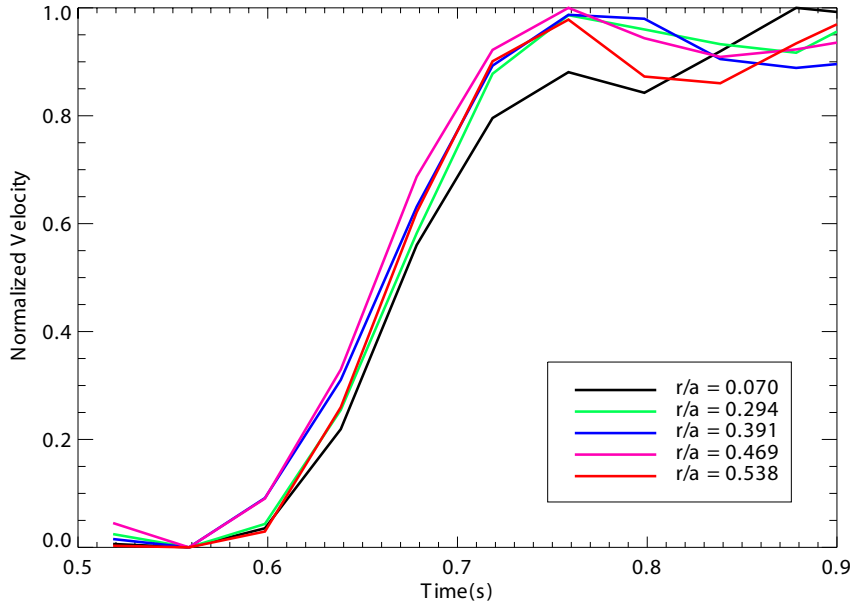

Figure 6-21: Time traces of normalized rotation at several r/a for I-mode discharges. Note that toward the end of the transition it is seen that the core channels come up later than the edge channels.

L-mode significantly off-axis.

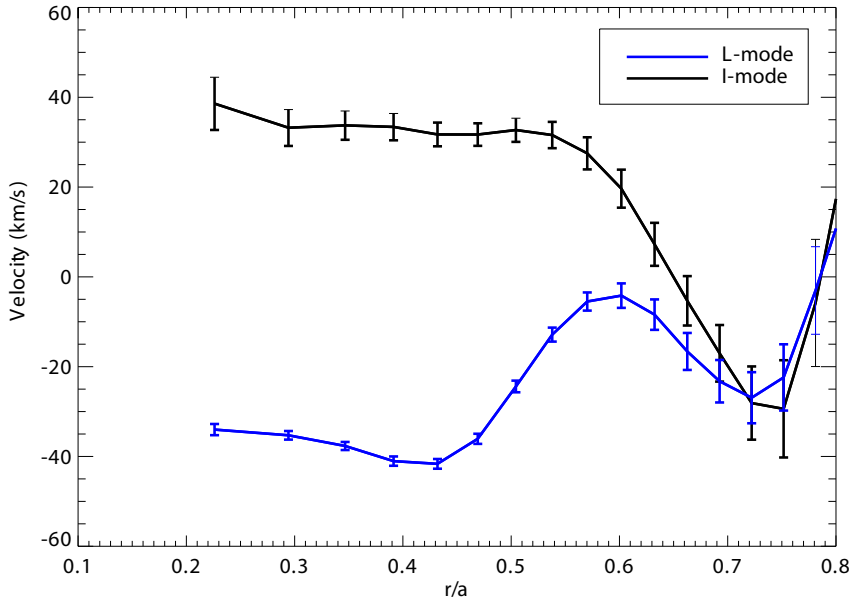

Figure 6-22: Average rotation profiles in the L-mode and I-mode case with characteristic statistical error bars shown. Note that the plasma is in upper single null.

As with the two previous cases, the "Toy Model" of rotation is applied to the example I-mode transition. The TRANSP calculated diffusion is shown in Figure 6-23, and the Peeters and Yoon form of the diffusion is shown in Figure 6-24. Note that ion temperature measurements within r/a= 0.2 are unreliable, so electron diffusion was substituted for ion thermal diffusion in these calculations. The time traces of calculated source profiles are shown in Figure 6-25. Unlike in the H-mode case, the time traces of the source do not have clear indications of the I-mode turning on.

The I-mode source profiles are compared against their L-mode complements in Figure 6-26. There is always a peak in the source profile at approximately r/a=0.6 and a negative peak at r/a$\sim$0.4, but this peak decreases in the transition to I-mode. The profiles of the electron density, temperature, and ion temperature are shown in Figure 6-27.

It is seen that while the I-mode and H-mode have some similarities in the source profile peak occurring off-axis, the profiles are far better defined in the H-mode case. Gradients of the driving terms are significantly more noisy, and the correlation of the gradient changes to the source profile changes are not as obvious as they are in the

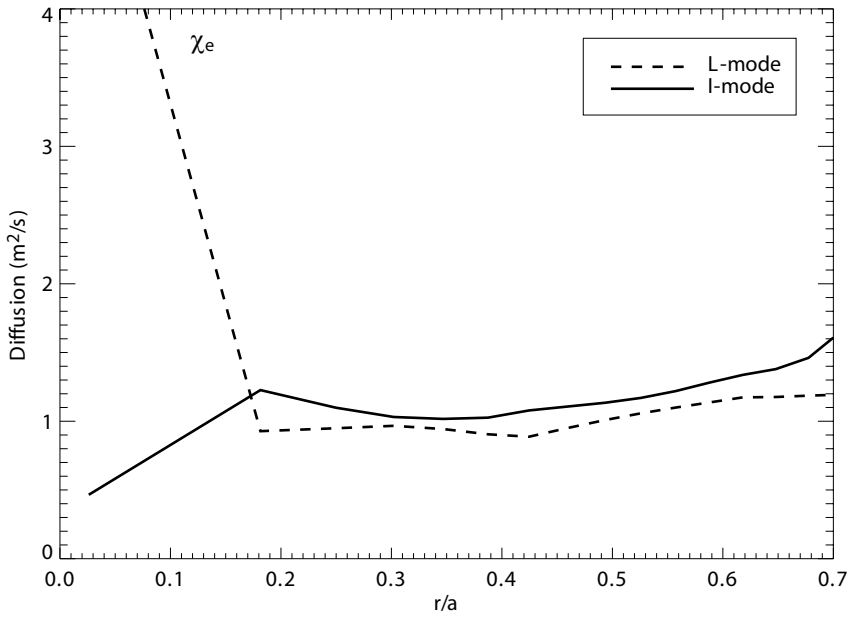

Figure 6-23: Average diffusion values as calculated by TRANSP before and after the I-mode transition. Due to high temperatures in the core of the plasma, ion temperature is not believable in the core of the plasma. The electron thermal conductivity was used instead of ion conduction.

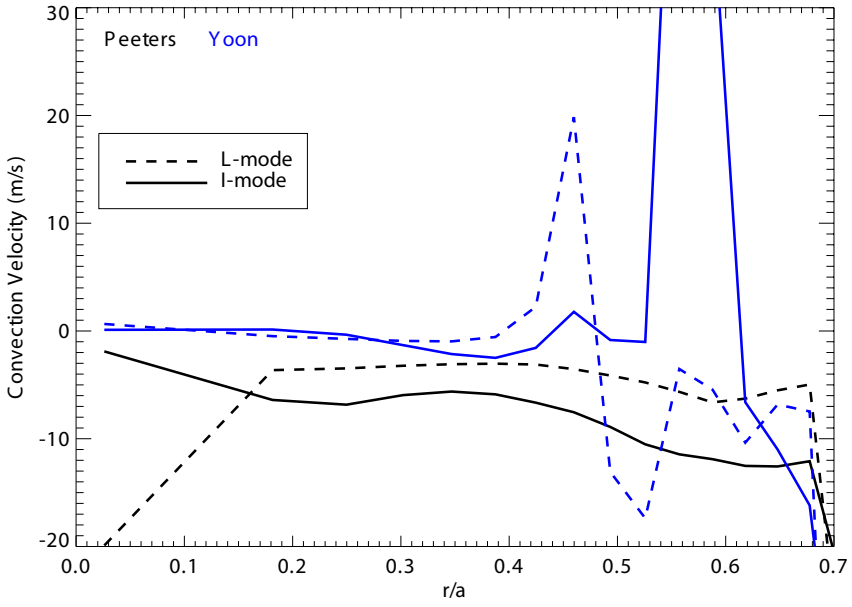

Figure 6-24: Average convective velocity values in the Peeters and Yoon form before and after the I-mode transition.

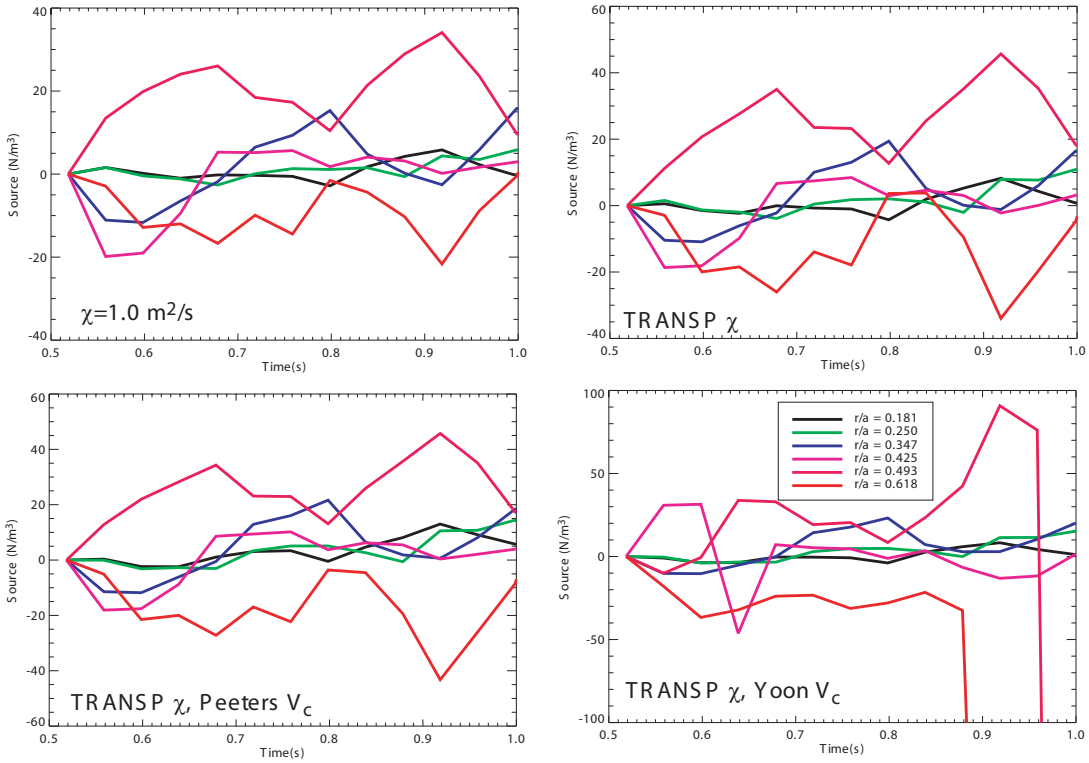

Figure 6-25: Source time traces at various radii for the I-mode case with [top left] a constant diffusion ($\chi = 1.0$ m^2/s) and no convection, [top right] a TRANSP calculated diffusion and no convection, [bottom left] a TRANSP calculated diffusion and Peeters convection, and [bottom right] a TRANSP calculated diffusion and Yoon convection.

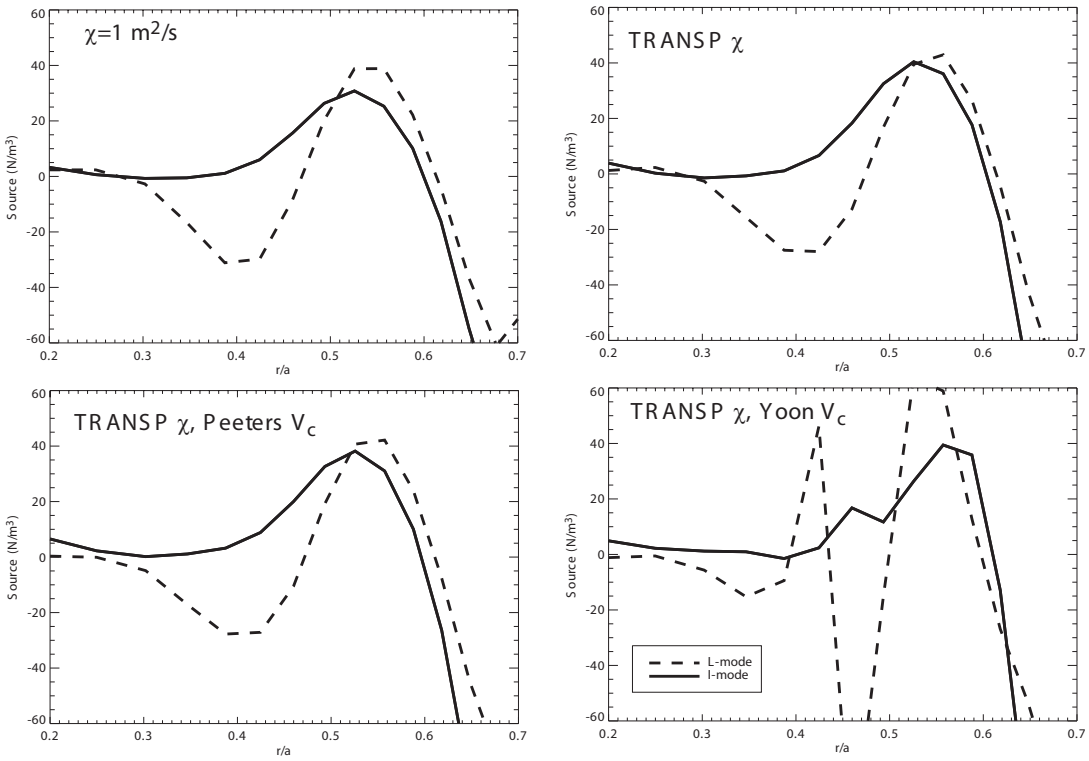

Figure 6-26: I-mode source profiles using Peeters and Yoon convective values and TRANSP diffusive values at characteristic L-mode and I-mode times.

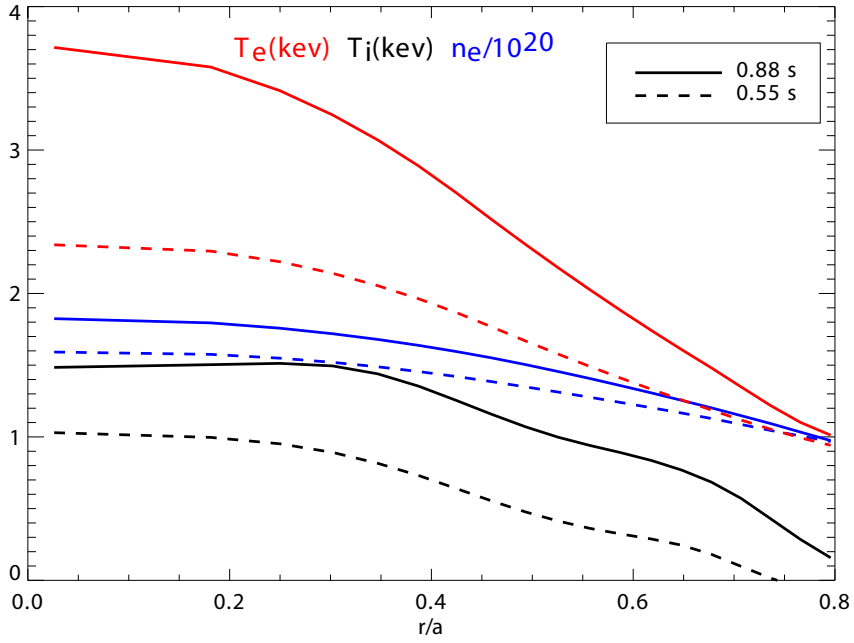

Figure 6-27: Ion temperature, electron temperature, and electron density profiles before and during the I-mode discharge.

H-mode case. While the H-mode case has a strong correlation of the change in source profile to the T_i gradient, the I-mode does not have such a strong behavior. Furthermore, the calculation of the residual Diamond and Yoshida forms of the residual stress is shown in Figure 6-28, where there are no similarities of the I-mode source profile and the H-mode source profile. The residual stress calculations do not appear to represent the experimental calculations of the source profiles. This effect may be due to a worse understanding of momentum transport in this regime with elevated temperature but not density.

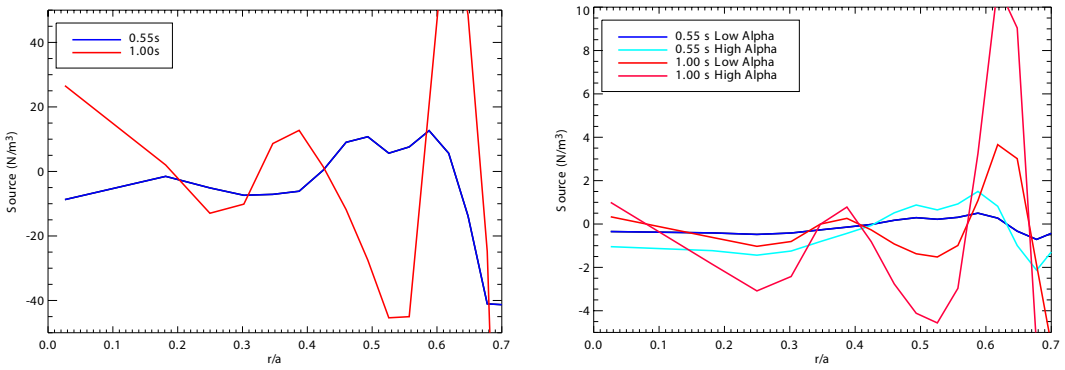

Figure 6-28: Calculation of the characteristic source profiles in an I-mode as derived from the Diamond and Yoshida forms of the residual stress.

6.3.1 I-modes and H-modes

In this section, the relation between I-mode and H-mode core rotation transitions will be analyzed. The momentum transport diffusive values will be generated using the same methodology as that discussed in [38].

In order to understand the I-mode regime in a similar way to the H-mode regime, the W.D. Lee simple model of diffusion is applied to the core profiles. This provides required momentum diffusion values to explain the I-mode transitions (assuming that the edge rotation is fixed to the final value of the rotation). The W.D. Lee calculation fits a purely diffusive model to a rotation transition in order to deduce a momentum diffusion value and, thus, a momentum confinement time. The model's more advanced version can deduce a convective term as well, but this calculation has serious issues

discussed in Chapter 2. An example fit of the W.D. Lee model to the I-mode data is shown in Figure 6-29. It is seen that the fit to the data is satisfactory with only diffusion; the momentum diffusion value is found to be 0.176 ± 0.015 m^2/s.

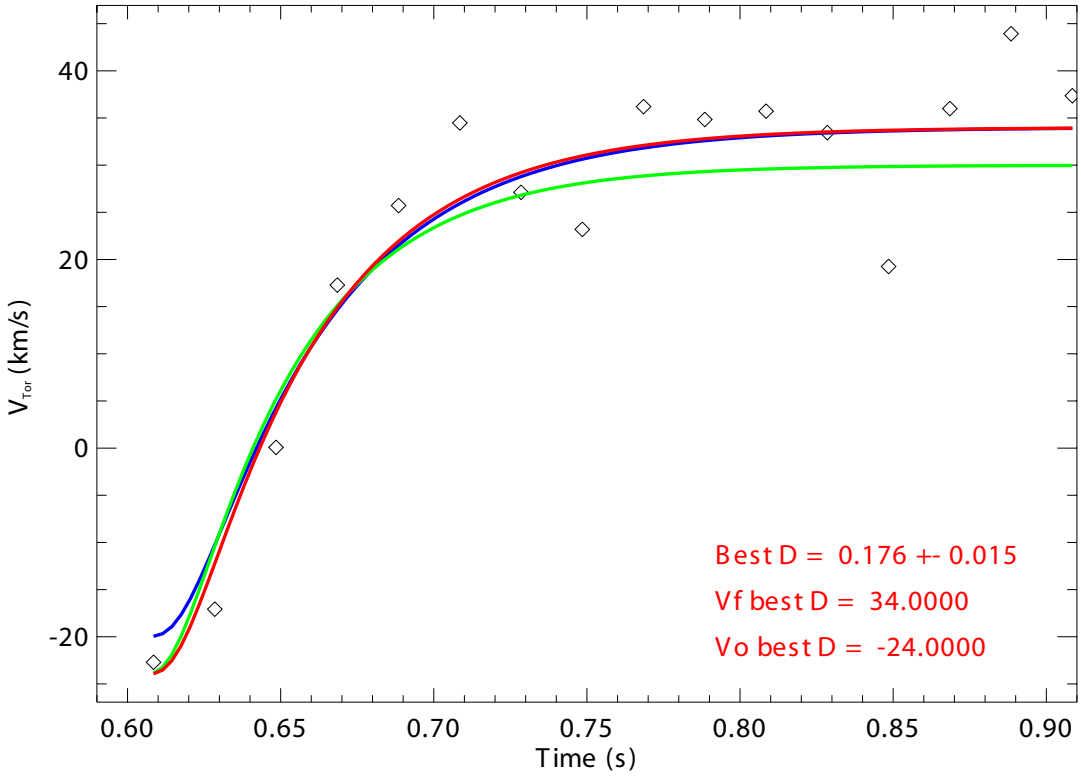

Figure 6-29: Example W.D. Lee diffusive model fits to I-mode data. The red line is the best fit and the green and blue lines correspond to extrema in the reasonable fitting parameters: they are used to generate the errors on the diffusive term.

An alternative fit with both diffusion and convection is shown in Figure 6-30. The fits appear to be better than the purely diffusive model, but, because the convective and diffusive terms can often accomplish the same effect in the fits, the errors on the terms increase dramatically from the purely diffusive case. Nevertheless, the best fit to the data has a diffusive value of 0.167 m^2/s and the convective term 1.03 m/s, which is of the order of magnitude expected for these terms.

For comparison, an H-mode diffusive value at similar magnetic field, current, and density is 0.26 ± .04 m^2/s. The diffusion in the H-mode case is significantly higher than in the I-mode case, even though the profiles are highly similar. This observation suggests intrinsic plasma differences between the I-mode and H-mode rotation

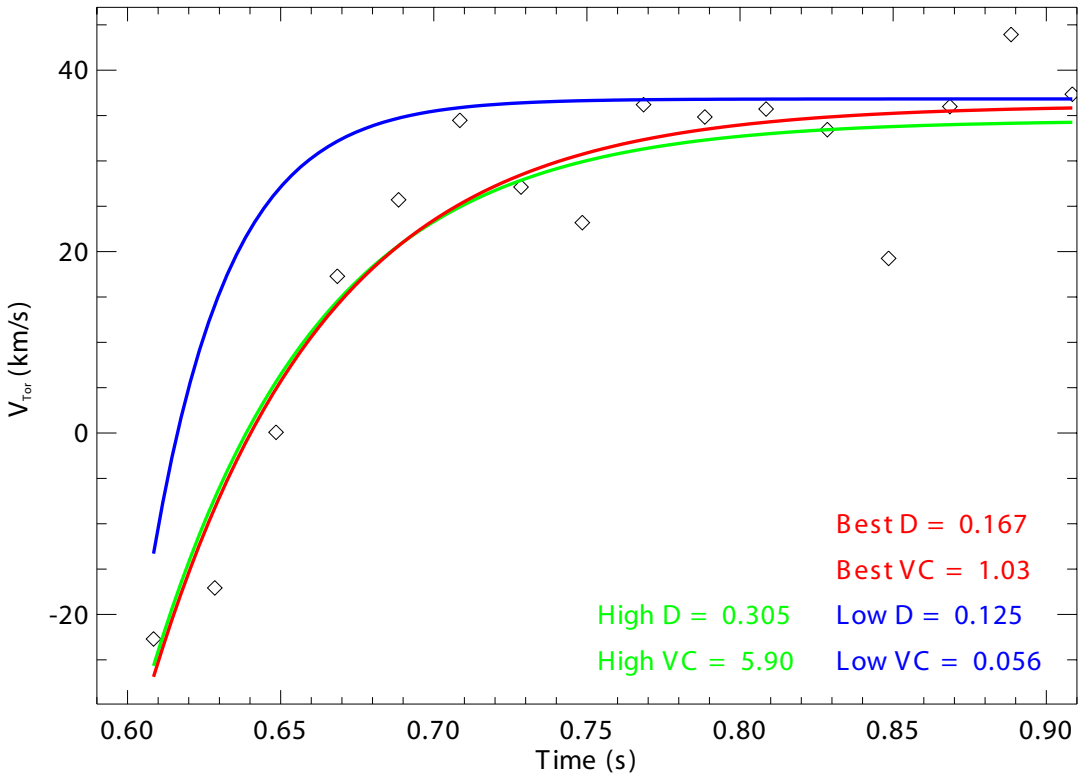

Figure 6-30: Example W.D. Lee diffusive and convective model fits to I-mode data. The red line is the best fit and the green and blue lines correspond to extrema in the reasonable fitting parameters: they are used to generate the errors on the diffusive and convective term. The high variation of the values in this fit exists because of the diffusive and convective numbers generating similar effects with the data.

transport, which has been seen with the changes in the residual stress observed in the plasma. These differences are not unexpected since the I-mode does not have an increased density behavior that is exhibited by H-modes. Overall, this comparison shows the differences between taking the "Toy Model" assumptions as given for an H-mode and I-mode and calculating the diffusive and convective momentum transport terms directly. There are significant differences in the calculation and in the simulations, which suggests that using both models is a valuable approach for understanding momentum transport.

6.4 Summary

Three cases of plasma transitions have been analyzed: SSEP sweeps, H-modes, and I-modes. All three transitions have some level of source profile appearing at mid-radii, which is generally where steep gradients are observed in the rotation profiles. The simple L-mode plasmas do not require convective profiles to explain the rotation profiles, and appear to be fairly well approximated by the Yoshida semi-empirical model of the source. H-modes and I-modes both have peaked rotation profiles, so they are improved by the convective pinch models. The Diamond form of the residual stress appears to be superior to the Yoshida form for H-modes, and it is seen that the calculation of the source profile in the plasma is correlated to the change in the temperature gradient from the L-mode to the H-mode regime. I-modes are matched fairly well by the simulations except at r/a=0.4 where a negative peak in the source profile is not able to be explained.

THIS PAGE INTENTIONALLY LEFT BLANK

Chapter 7

Conclusions and Future Work

The work here has provided a significant amount of new observations about the nature of plasma rotation in a tokamak plasma. In this chapter, a summary of the results and their implications will be listed. This section will also propose some new experiments and analyses that could be performed as extensions to this work.

7.1 Imaging x-ray Spectroscopy

The HiReX Sr spectrometer has undergone some major improvements as listed in Chapter 3. New diagnostic software was designed for HiReX allowing improved data analysis capabilities with superior uncertainty calculations, multiple analyses based on timing bins, and superior data quality control. These codes allow significantly more versatile use of the profiles for gyrokinetic simulations and transport analyses.

There has been a large scale effort to improve the physical aspects of the HiReX Sr device as well and, particularly, control of the thermal drift of the emission line position on the detectors. Thermal shields and temperature sensors have been installed on HiReX Sr, and the nature of the drift has been characterized. The thermal shielding is still imperfect, so calibration mechanisms have been attempted on HiReX Sr. These mechanisms are the same that have been proposed for the ITER core imaging x-ray spectrometer. None of them has, as of yet, proved to be effective due to either poor signal rates or incompatibility of the calibration method and standard operation

of the spectrometer.

Two successful calibration procedures were developed as well. Vignetting of the lines of sight in the spectrometer is measured using a laser alignment system, preventing spurious signal changes from causing confounding issues in the line integrated data. Furthermore, through the use of wide angle fluorescence, an in-situ calibration mechanism was created to allow recalibration of the HiReX Sr spectrometer at low X-ray energies and, thus, to quantify the error due to absolute sensitivity of the spectrometer.

7.1.1 Future work on HiReX Sr

HiReX Sr has always utilized a helium atmosphere inside of its housing, which simplified the construction of the device. The helium in the housing has uncertain purity and variations in density depending on temperature, time of day, humidity, etc. The ideal situation would be the use of a vacuum environment between the plasma and the detectors. The detectors are limited to operation with helium or air due to heating issues of the electronic parts, but they can be placed outside of a beryllium window. This arrangement would allow absolute intensity measurements of the argon in the plasma, since the X-ray transmission coefficients of beryllium are well known, while that of helium is dependent on a variety of external factors. A concern with this design would be additional support struts required for the beryllium windows that may cause vignetting. This concern will have to be weighed against the superior signal of the design.

Alternatively, the HiReX Sr system can be improved through a more tangentially viewing port. This will ease the difficulties in the measurement by giving a longer projection of the toroidal rotation along the HiReX Sr lines of sight. New diagnostics involving main ion charge exchange [103] have also been being developed and would allow comparing the main ion to argon impurity rotation behavior and thus testing the assertion that impurity rotation is identical to ion rotation.

Another improvement that should be implemented in a future system is the development of an intra-shot in-situ wavelength calibration system. HiReX Sr has been

successfully calibrated in a laboratory environment through the use of a cadmium anode x-ray tube: cadmium Lα X-rays appear on the helium-like system near the w line. This has been the most successful calibration technique, and implementing it as part of the HiReX Sr connection to Alcator would solve the drift and calibration issues. An alternate technique to placing an X-ray source inside the vacuum system would be using cadmium tiles placed in the C-Mod wall. An external radio frequency quadrupole accelerator [104] is being placed on Alcator C-Mod, and it can use the C-Mod toroidal and poloidal field magnets to steer its emitted proton beam to most position on the inner wall. The beam can excite cadmium X-rays at a known position, which will calibrate both the spectral drift of the HiReX Sr spectrometer and the angle of the spectrometer with respect to the C-Mod vacuum vessel.

7.2 Rotation Reversals

Spontaneous reversals of rotation in L-mode plasmas as a function of current, density, shape, and magnetic field have been identified on Alcator C-Mod. This rotation reversal is accompanied by density fluctuation changes and is correlated to the transition from the LOC to the SOC regime. This reversal provides the most powerful characterization of the LOC to SOC transition ever observed. The best fit equation for the rotation reversal is found to be approximately $n_e q = 3.5$ at $B_T = 5.4$T. It is commonly believed that the LOC to SOC transition is driven by the changeover from the TEM to ITG mode dominated regime.

Linear gyrokinetic simulations of the rotation reversal discharges have been performed to confirm that the plasmas are switching from a TEM to an ITG dominated regime. It was observed that in the counter-current rotation phase switch to the co-current rotation, the linear instability simulations place the experimental data closer to the TEM changeover from the ITG regime. It is found that at low density the dominant linear instabilities are density driven TEMs, while at higher density, the plasma is primarily in the ITG regime. It is unclear if the confinement and profile changes are directly coupled, but the dominant profile change has been identified as

the T_e/T_i change which drives the turbulent mode transition.

7.2.1 Future work on Rotation Reversal

It is possible that subdominant modes will play an important part in the total turbulence spectra in these near transition modes. In order to quantify the modes properly, it will require the use of nonlinear simulations to verify the subdominant modes in relation to the most unstable mode and account for non-linear upshift in the TEM/ITG change. Furthermore, separating the density scale length, electron to ion temperature, and the total density will improve the understanding of the reversal's relation to collisionality and the TEM/ITG drivers. These tests could be accomplished through the use of pellet injection or targeted ECH heating.

7.3 Lower Hybrid Current Drive induced Rotation

Lower Hybrid Current Drive has been observed to induce rotation in plasmas. In this work, it is seen that the Lower Hybrid Current Drive is capable of driving both co- and counter-current rotation depending on plasma parameters. There is an observation of a reversal in the LHCD rotation, which is reminiscent of the Ohmic rotation reversals, but it is much more gradual. The LHCD rotation changes are dependent on the plasma current and the magnetic geometry of the plasma. There are observed turbulence changes in the counter-current rotation from LHCD, which is asymmetric in wavenumber space. It was seen that the amount of power inputted by the LHCD affects the rotation behavior of the plasma. This may be due to either the q-profile modification or the electron temperature in the plasma. It appears likely that the LHCD is modifying the q-profile, which changes the intrinsic residual stress and causes the rotation changes in the plasma. Alternatively, LHCD also modifies the electron temperature and thus the ratio of the electron to the ion temperature, in a similar method to the Ohmic rotation reversal, and may be the dominant driver for the reversal in the LHCD rotation.

Linear gyrokinetic sensitivity studies have been performed on the LHCD dis-

charges, and it is seen that there is a strong dependence of the turbulence on the density scale length. The linear instability is mostly insensitive to the other parameters and scale lengths in the plasma. It is always seen that the turbulence is in the TEM regime, and the counter current driven cases are closer to the ITG regime changeover than the co-current driven cases, which is consistent with the Ohmic rotation reversal results.

7.3.1 Future work on Lower Hybrid Current Drive Induced Rotation

In the future, testing the density and magnetic field dependence of the LHCD rotation reversal will allow confirming if the LHCD rotation behavior is certainly part of the Ohmic rotation reversal dependence. It is expected that there will be a linear density relation as with the rotation reversal, with the extra complication that higher density lowers LHCD efficiency and higher magnetic field improves LHCD. A comprehensive scan of discharges with MSE data available would also allow confirming if the q-profile modification is the driver for the rotation reversal or if it is purely the direct momentum input and the T_e/T_i ratio. Non-linear gyrokinetic simulations of the LHCD results with models for the lower hybrid deposition effects would also be particularly valuable for explaining the turbulent modifications. While an approximation for the hot electron tail has been found not to affect the linear turbulence significantly, a better treatment of the effect of those electrons on the turbulence would be an improvement to this modeling.

7.4 Source Profiles in Plasma Transitions

The simplified model of rotation has been used previously to provide rotation transport coefficients during mode transitions. Based on the simplified model of rotation, the "Toy Model" of rotation was developed and implemented using the superior data available from the HiReX Sr spectrometer and TRANSP to calculate approximate

residual stress/source profiles in the plasma. The "Toy Model" has been applied to three scenarios in order to understand how the residual stress behaves. In the simple SSEP sweep, small source profiles were found and the convective pinches generally did not improve the fits to the data. In an H-mode, however, the convective pinch does decrease the calculated source profiles, implying that theoretical models of convection are applicable in that case. In the final case (I-modes), convective velocities improve the fits to the data slightly, but the shape of the profiles are not changing significantly due to the shape of the theoretical convective pinch. Overall, diffusive profiles can be used to explain the majority of the variation in a tokamak plasma, and convective profiles improve the fits only in a peaked profile such as an I-mode or H-mode.

Two models of the residual stress were compared against the calculations in this work. The Yoshida semi-empirical model agreed fairly well with the L-mode cases analyzed, but the magnitude of the residual stress agreed better with the Diamond form in H-modes. The Diamond form also reproduced the shape of the source profile better in the H-mode case than the Yoshida form.

7.4.1 Future of Source Profile Calculations

The "Toy Model" is naturally an approximation of the actual physics of rotation transport. Further application to plasma transitions should provide better benchmarking to this calculation. A particularly valuable application of the model would be on devices with neutral beams that provide a known torque in the plasma. Applying the "Toy Model" to a plasma that is dominated by a known torque would allow separating the intrinsic rotation from the source profile. Also, applying models for momentum sources from RF effects would be valuable as well, since it could further separate the ICRF wave physics from the purely intrinsic source. Since RF models are not always simple to solve directly, this may require better TRANSP to "Toy Model" linking.

One area that these results concern is experiments that utilize perturbative analysis of the plasma momentum. In these experiments, the plasma is changed on a fast

time scale at a supposedly known location (such as several fast SSEP or H-mode transitions) in order to infer momentum transport coefficients. Since the results from the "Toy Model" had core source profiles observed in all of these calculations, it makes it impossible to assume that the momentum perturbation is solely localized at the edge. The core changes may in fact be confounding the results found by those experiments.

THIS PAGE INTENTIONALLY LEFT BLANK

Appendix A

Alcator C-Mod

The observations discussed in this work were performed at the Alcator C-Mod device at the Massachusetts Institute of Technology's Plasma Science and Fusion Center (MIT PSFC). Alcator C-Mod is a small, high field tokamak operated for $\sim$2 seconds with deuterium fuel. While the temperatures in Alcator C-Mod are not reactor applicable, the electron densities and magnetic fields are of the same magnitude as those expected to exist on fusion reactors and at the ITER device [115]. Alcator C-Mod operational parameters are shown in Table A. A plot of the C-Mod vessel with characteristic flux profiles in an USN plasma is shown in Figure A-1.

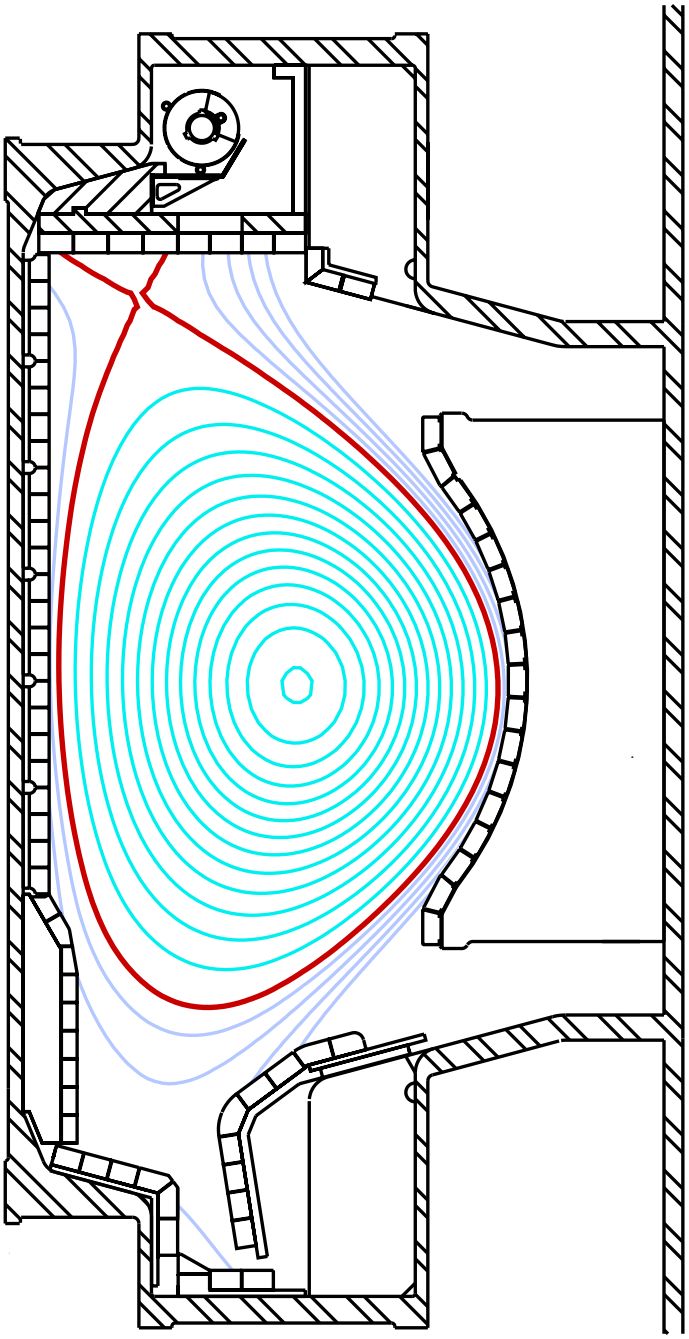

Figure A-1: Plot of the C-Mod vessel in a characteristic USN plasma. Blue lines represent EFIT reconstructions of the flux surfaces and red lines represent the last closed flux surface, which is the limit of the plasma.

Table A.1: Alcator C-Mod operational parameters and ranges.

Parameter	Range
Major radius	0.67 m
Minor radius	0.22 m
Magnetic Field	3-8 T
Plasma Current	<2 MA
Electron Temperature	<9 keV
Electron Density	0.2-10E20m^{-3}
Pulse Length	<2.5 s
Auxiliary Heating ICRF	<6 MW
Auxiliary Lower Hybrid Current Drive	<1 MW
Inner wall material	Molybdenum
Magnetic Geometry	Limited or Diverted

THIS PAGE INTENTIONALLY LEFT BLANK

Appendix B

GS2 High k Modeling

Modeling of both the high and the low current case with Lower Hybrid was performed using the GS2 gyrokinetic code at high k values. Both of these cases had $k_\theta \rho_i$ restricted to 10-40, with the most unstable mode generally appearing in the 25-35 range. The growth rates and frequencies are generally large, but due to the high k values, they will not produce significant transport (via $\Gamma \propto \gamma/k^2$). These modes are in the electron diamagnetic direction and, thus, are identified as Electron Thermal Gradient (ETG) modes. The high current case is shown in Figure B-1, and the low current case is shown in Figure B-2. The frequencies of these modes are in the megaradian/s range, and these are generally located outside of r/a=0.5.

It is seen that the ETG turbulence does have marked differences between the pre-LHCD phase and the LHCD phase in the high and the low current. The ETG turbulence is destabilized by LHCD in the high current case, and is, in fact stabilized in the low current. This effect is from the modification of the density and temperature profiles by the Lower Hybrid waves. It has been observed that the critical temperature gradient for the ETG threshold scales with shear, density gradient, T_e/T_i, collisionality, and plasma pressure [108]. As seen from Figures 5-14 and 5-13, the density gradients, T_e/T_i, and plasma pressure change differently in low and high current plasmas. These differences are changing the thresholds for the mode destabilization, specifically the T_e/T_i scales linearly with the critical R/L_{T_e}.

Overall, these high wavenumber space modes were not explored in detail. While

there are differences in the low wavelength mode changes from LHCD as a function of plasma current, they are located fairly outside of the reversal pinning, and the modes are not expected to cause significant transport. Furthermore, the turbulence destabilized by these modes is of significantly higher frequency that that observed by the PCI system.

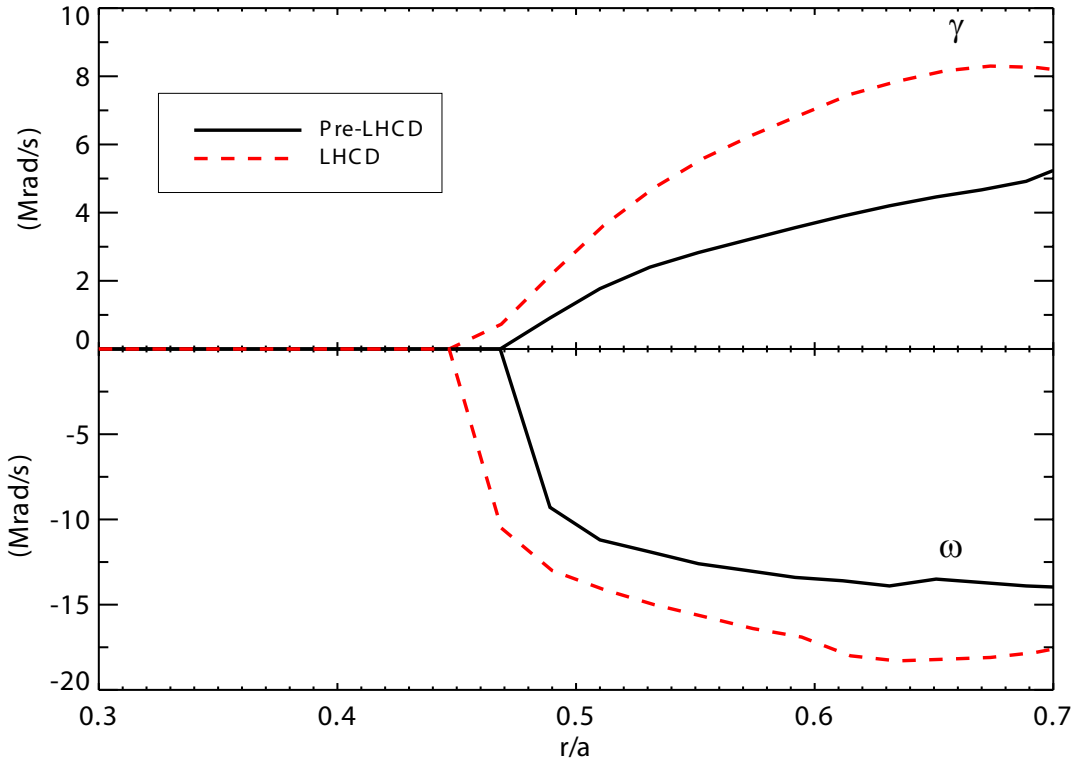

Figure B-1: Linear GS2 calculations of the most unstable mode versus radius in a 700 kA discharge with and without LHCD at high k values of turbulence.

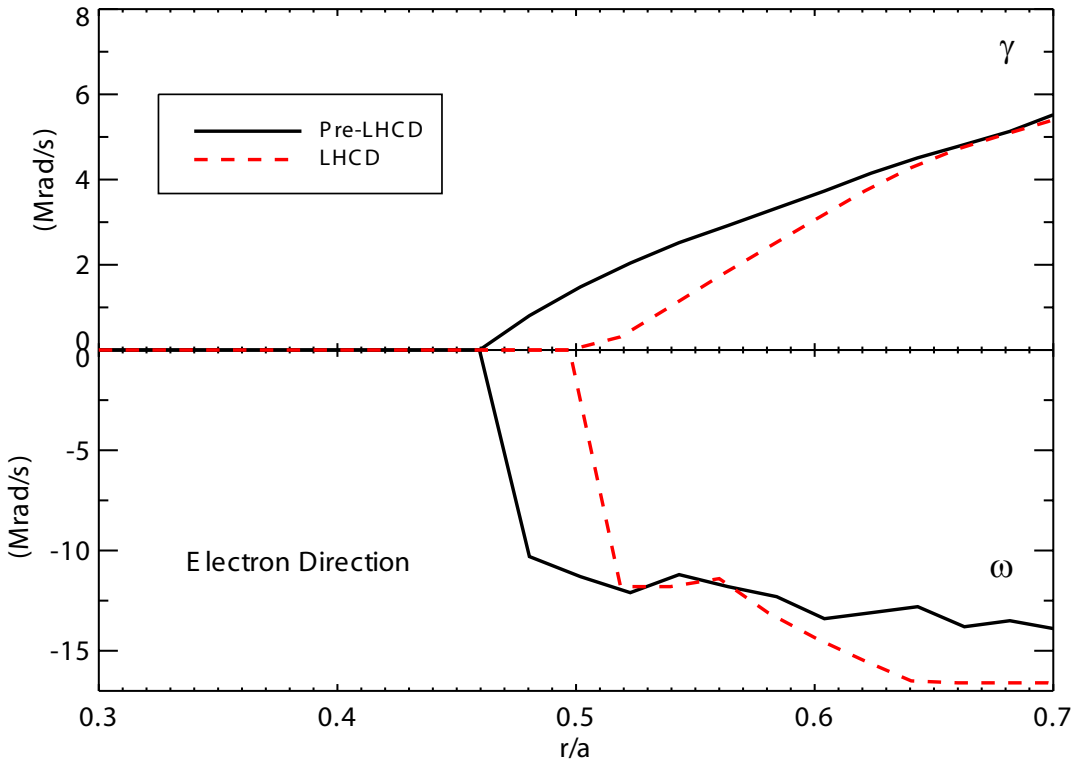

Figure B-2: Linear GS2 calculations of the most unstable mode versus radius in a 350 kA discharge with and without LHCD at high k values of turbulence.

THIS PAGE INTENTIONALLY LEFT BLANK

Appendix C

Correcting the HiReX Sr Rotation Drift

In the absence of a locked mode calibration as described in Chapter 3, the rotation profiles found by HiReX Sr need to be DC corrected for the drift of the device over time. This is accomplished through the use of the HiReX Jr spectrometer or an x-ray tomography system. HiReX Jr provides a measurement of the rotation on axis and the x-ray tomography system can identify the location of the $q = 1$ surface, and deduce its rotation frequency from the sawtooth precursor frequency. These measurements can then be used to pin the HiReX Sr rotation profile to that value at a given radial location.

There are open concerns with this method however. The primary concern is whether or not the rotation profile is modified by the drift, since this will not be corrected for by a DC shift. In order to test this effect, a single simple H-mode discharge was selected and the emissivity profile was artificially moved by a constant wavelength shift. The new profile was re-inverted with the exact same procedure as the original discharge.

The first issue to analyze is whether the DC shift should be applied in kHz or km/s. While kHz is more appropriate for the inversion routine in the plasma, the shift in 2d spacing of the crystal from temperature shifts may make velocity a more correct representation of the effect ongoing. Two lambda shifts were tested in both

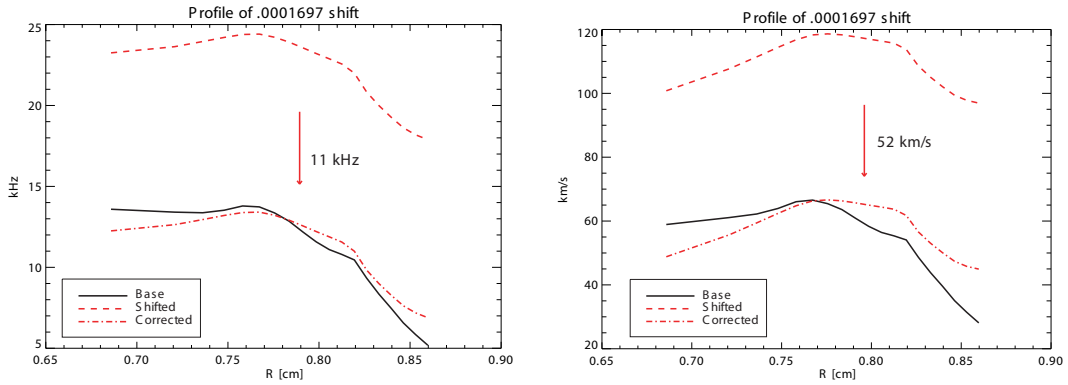

Figure C-1: Comparison of the inversion and correction of a single $\Delta\lambda = 0.0001697$ Åshift of the image during an H-mode. Correction in rotation frequency performed (left) and rotation velocity (right) shown.

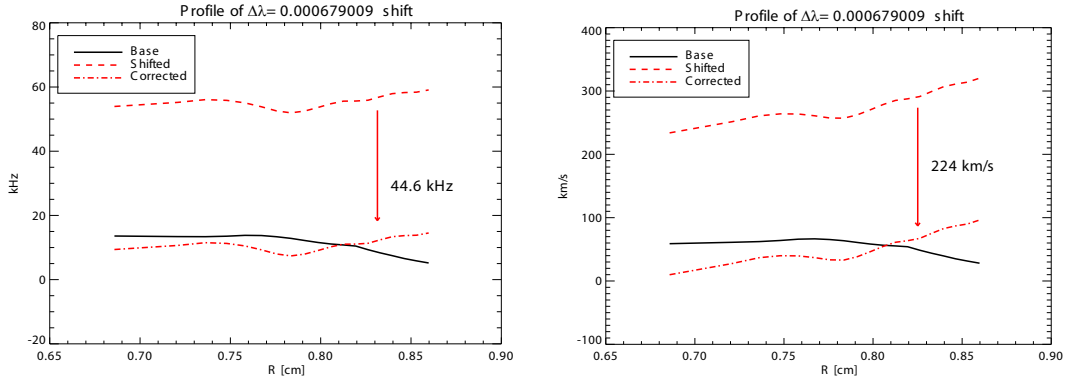

Figure C-2: Comparison of the inversion and correction of a single $\Delta\lambda = 0.000679009$ Åshift of the image during an H-mode. Correction in rotation frequency performed (left) and rotation velocity (right) shown.

kHz and km/s, and these are shown in Figures C-1 and C-2. It is seen that the rotation frequency correction is significantly better than the velocity shift, since it maintains the shape of the profile better. It is also noticed that as the shift becomes larger, the shape of the rotation profile changes. In the situation when the drift is of order 44 kHz, the rotation profile shape is completely shifted from the original case. If the drift is of order 11 kHz (52 km/s) or less, the shape of the profile is not greatly changed. This observation caused the implementation of a general rule that DC correcting was only used if the shift from the previous locked mode on-axis was below 50 km/s.

There is a natural increase in velocity during this discharge which is an H-mode

shot. One of the tests that was run was taking the average offset induced by the shift as a function of time. If the velocity of the plasma is a major factor of the profile shift, then the DC correction induced by the plasma transition in the shifted and unshifted wavelength cases would be different before and after the transition. A plot of this test is shown in Figure C-3. The average velocity offset does not change at all during the transition, so minor changes in the velocity of the plasma do not change the total profile significantly. Furthermore, changes in velocity are still reasonable to analyze if the drift is within the previously mentioned limit.

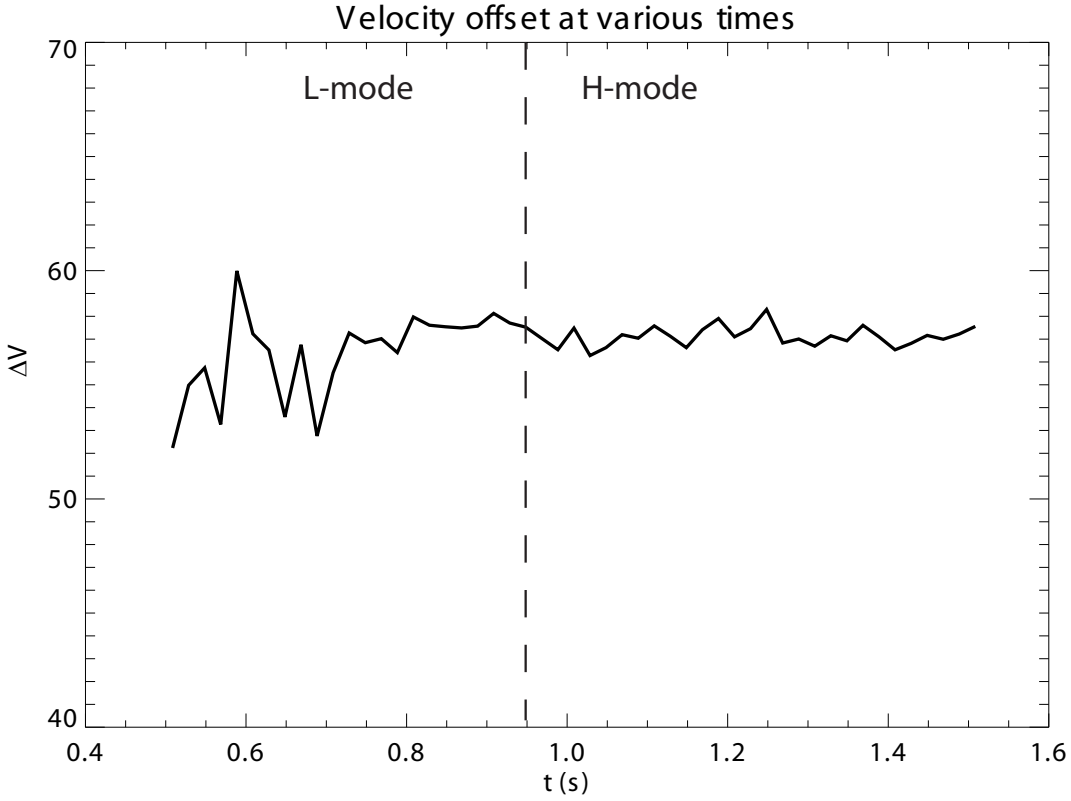

Figure C-3: Average offset from a shifted and unshifted wavelength discharge during an H-mode discharge. Transition from L- to H-mode is marked as a dashed line.

THIS PAGE INTENTIONALLY LEFT BLANK

Appendix D

Overview of ITG modes and TEMs

Microturbulence is a major topic discussed in this work, and it is the primary focus for much of the research in anomalous transport in plasmas. The two most commonly described forms of microturbulence are ion thermal gradient modes (ITGs) and trapped electron modes (TEMs). In this section, following the arguments in [111], a brief description of these modes will be presented.

Assuming that ions are in the fluid limit ($\omega_{Di}, k_{||} v_{thi} \ll \omega$), circulating electrons have adiabatic response ($\omega/k_{||} \ll v_{the}$), and trapped electrons have $v_{the||} \ll \omega/k_{||} \ll v_{the}$, yields three relations for the perturbed densities as a function of the fluctuating potential.

$$\frac{\delta n_i}{n} = -\frac{e\delta\phi}{T_i}\left[\frac{\omega_{*i}-\omega_{Di}}{\omega} + \frac{\omega_i(1+\eta_i)\omega_{Di}}{\omega^2} + \left(b_i - \frac{k_{||}^2 v_{the}^2}{\omega^2}\right)\left(1 - \frac{\omega_{*i}(1+\eta_i)}{\omega}\right)\right] \tag{D.1}$$

$$\frac{\delta n_{eC}}{n_{eC}} = \frac{e\delta\phi}{T_e} \tag{D.2}$$

$$\frac{\delta n_{eT}}{n_{eT}} = \frac{\omega_{*e}}{\omega - \omega_{De}}\frac{e\delta\phi}{T_e} \tag{D.3}$$

where n is the ion density, n_{eC} is the circulating electron density, n_{eT} is the trapped electron density, ω is the mode frequency, k is the mode wavenumber, $\eta_i = d\ln T/d\ln n$,

$\omega_D = k_\theta g/\Omega_c$, g=$v_{th}^2/R$, $b_i = k_\theta^2 \rho_i^2/2$, $\omega_* = k_\theta D_B/L_n$, $D_B = cT/ZeB$, $\mathrm{L}_n^{-1} = -d\ln n/dr$, $\tau = T_e/T_i$, and $\epsilon_n = L_n/R_0$. By assuming quasineutrality of the fluctuations, $\delta n = \delta n_{eC} + \delta n_{eT}$, a dispersion relation can be derived of the following form.

$$\frac{\omega_{*i} - \omega_{Di}}{\omega} + \frac{\omega_{*i}(1+\eta_i)\omega_{Di}}{\omega^2} + \left(b_i - \frac{k_\parallel^2 v_{thi}^2}{\omega^2}\right)\left(1 - \frac{\omega_{*i}(1+\eta_i)}{\omega}\right) + \frac{1}{\tau} - \frac{1}{\tau}\frac{n_{eT}}{n}\langle\frac{\omega - \omega_{*e}(1+\eta_e(E/T_e - 3/2))}{\omega - \omega_{De} + i\nu_{eff}}\rangle_E = 0 \tag{D.4}$$

Solving Equation D.4 for unstable modes yields four approximate growth rates that are commonly referred to as the CTEM (D.5), DTEM (D.6), TEM (D.7), and ITG (D.8) growth rates.

$$\gamma \simeq \omega_{*e}\left(\frac{2\pi r}{R}\right)^{1/2}\eta_e\left(\frac{R}{L_n}\right)^{3/2}\left(\frac{R}{L_n} - \frac{3}{2}\right)\exp(-R/L_n) \tag{D.5}$$

$$\gamma \propto \frac{\epsilon^{3/2}\omega_{*e}^2}{\nu_{ei}}\left(\frac{3}{2}\eta_e + b_s\right) \tag{D.6}$$

$$\gamma \sim (k_\theta \rho_i)\sqrt{(n_T/n)g_i/L_n} \tag{D.7}$$

$$\gamma \sim (k_\theta \rho_i)\sqrt{\eta_i g_i/L_n} \tag{D.8}$$

These rough estimations of the growth rates of the various modes provide guidance to which modes exist in the plasma. For instance, the CTEM mode is stabilized if $R/L_n < 3/2$, which turns the growth rate negative. These equations are approximations, and the actual mode structure and growth rate is studied in more detail in many references; see, for instance, [112, 113, 114].

Appendix E

"Toy Model" Sensitivity Studies

Since it is established that the SSEP sweep case is a simple rotation model, these cases can also be used to test the sensitivity of the "Toy Model" to various changes in the assumptions listed in the earlier sections.

1. **Momentum Diffusion Sensitivity**

   One of the major open questions is what effect variations in the Prandtl number (χ_ϕ/χ_i) have on the momentum transport. It has been characterized that the Prandtl number is generally of order unity, but variation has been seen in that number. For this reason, sensitivity studies to the diffusive profiles must be performed.

   The initial and simplest study is to set the diffusive value to a constant and then vary it with no convective term implemented. These variations are shown in Figure E-1. As the diffusive term increases, the source profiles are actually forced to increase. While at first glance this is counter-intuitive, the high diffusive values should flatten the profile, thus a higher source value is required in order to create a shaped profile.

   An alternate test of the diffusion sensitivity is varying the diffusion profile as calculated by the TRANSP code. In this situation, the sensitivity is directly varied to scan the Prandtl number. The results of this study are shown in Figure E-2. While the magnitude of the source profiles does change similarly

to that of the previous sensitivity study, the sensitivity to the diffusive term is overall fairly minor as seen by the small changes in the source profiles.

2. **Convective Velocity Sensitivity**

   Another possible sensitivity arises from minor changes in the convective profile from temperature and density errors from the fitting parameters. These sensitivities need to be analyzed using both the Peeters and the Yoon form of the convective profile. The Peeters form of the convective term sensitivity is shown in Figure E-3, and the Yoon form is shown in Figure E-4.

In summary, a 50% variation in the diffusive or convective values in the plasma does not affect the source profile significantly. Generally increasing diffusion and convection forces an increase in the momentum source value in order to explain properly the experimental profile. Since the rotation profiles within r/a=0.2 are often flat, the transport fitting parameter variations within that region are not expected to cause a significant change anyway. The sensitivity to diffusion and convection terms does not provide clear changes in the source profile.

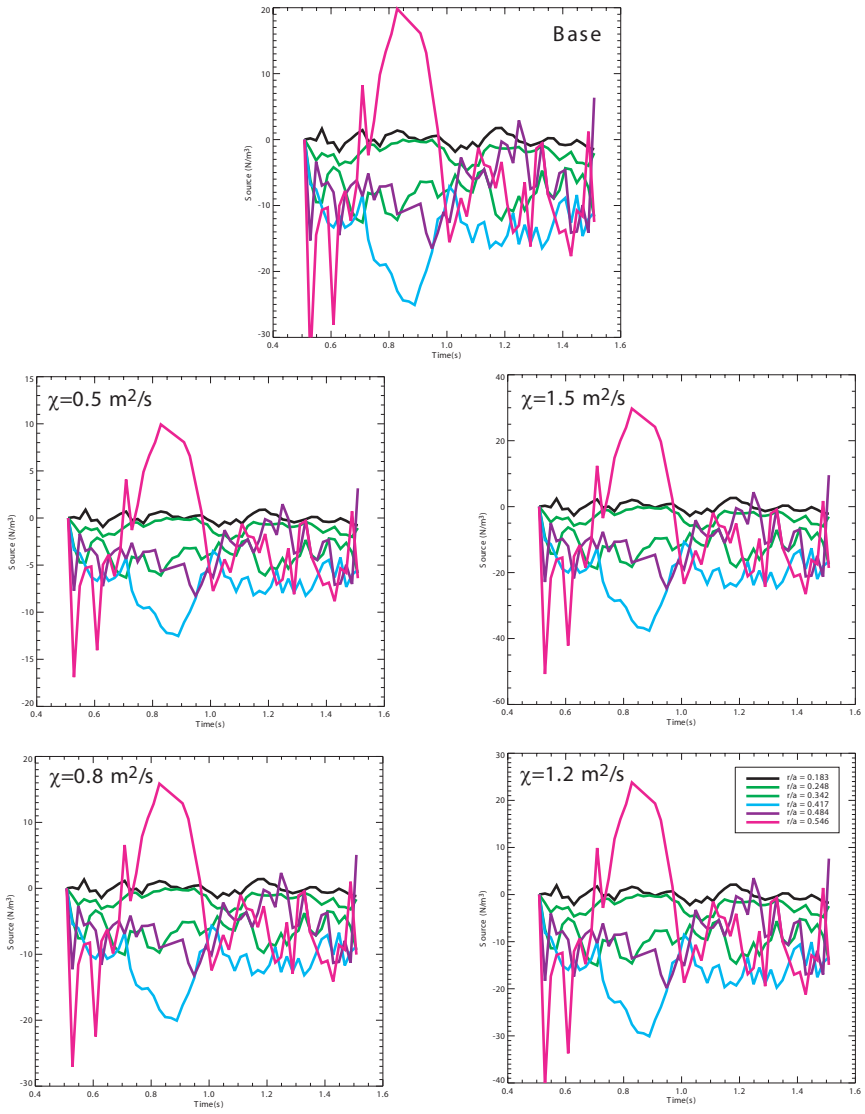

Figure E-1: Time traces of the rotation source at various radii with different values of the diffusive term. Note that there are no convective terms implemented in this case.

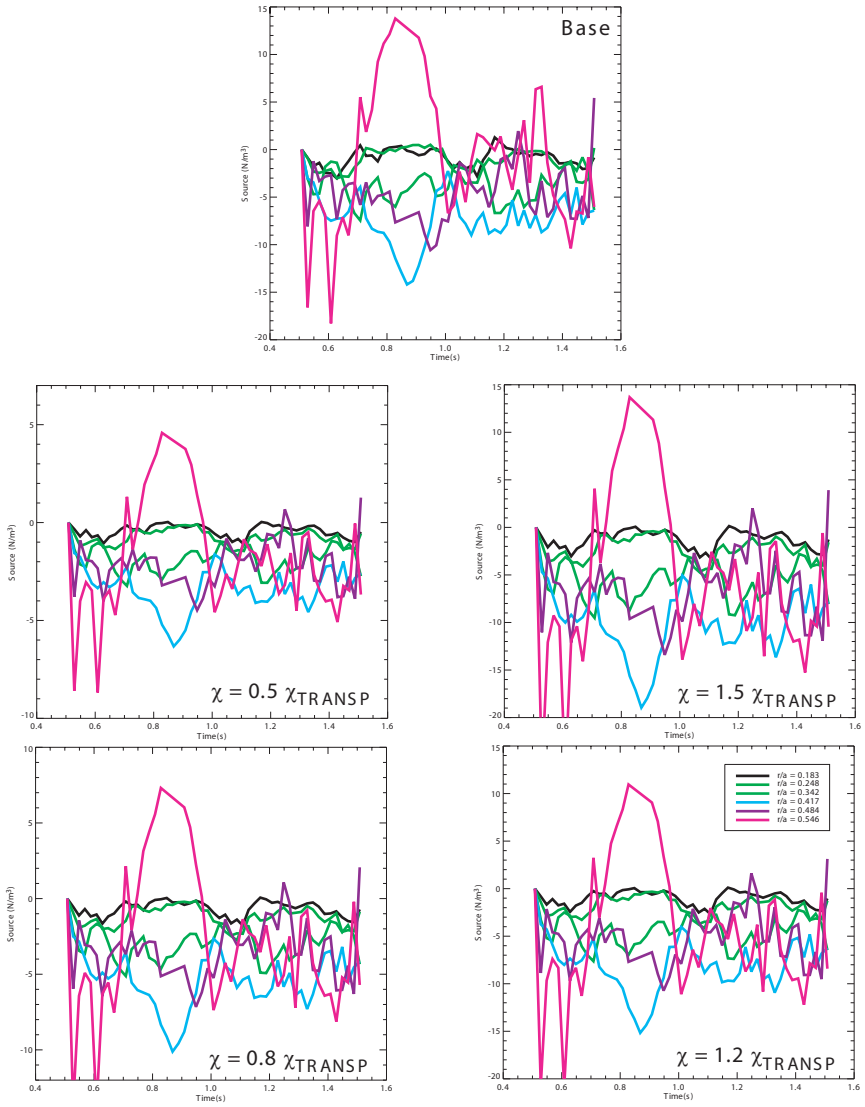

Figure E-2: Time traces of the rotation source at various radii with different scaling values of the TRANSP diffusive term. Note that there are no convective terms implemented in this case.

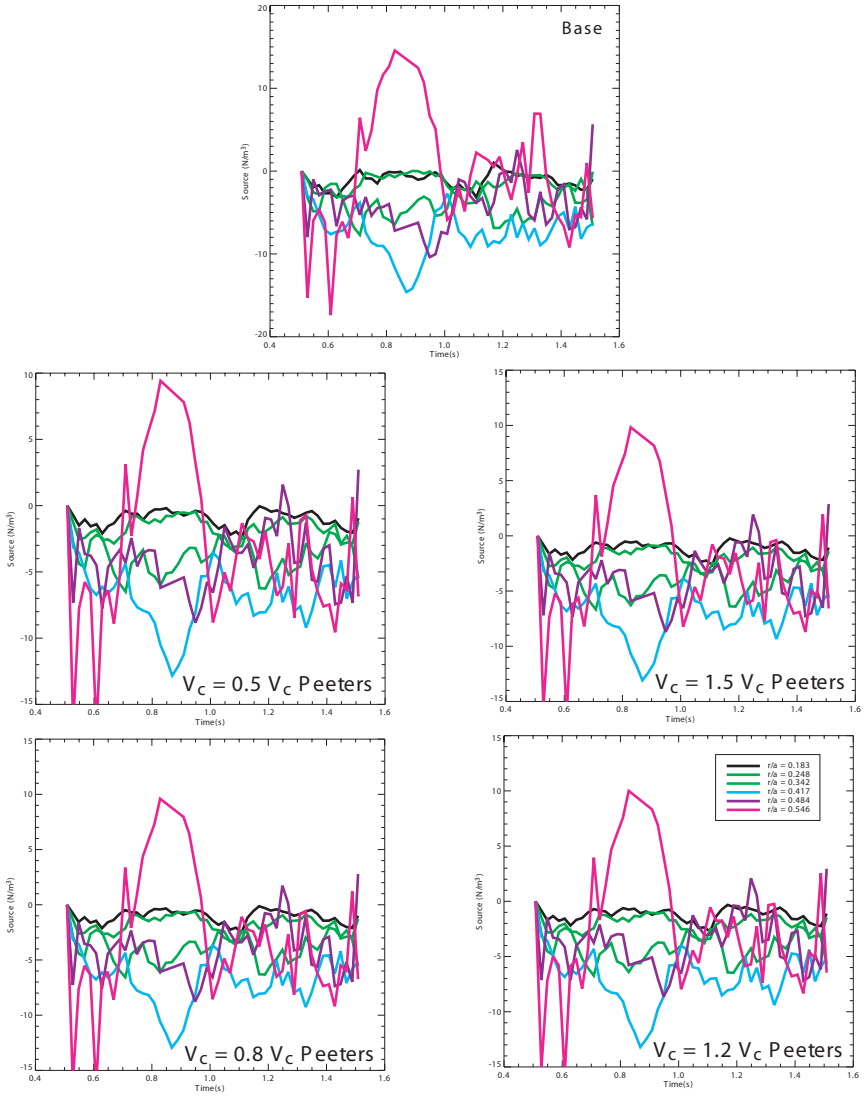

Figure E-3: Time traces of the rotation source at various radii with different scaling values of the Peeters convective term. TRANSP diffusion is used in this case.

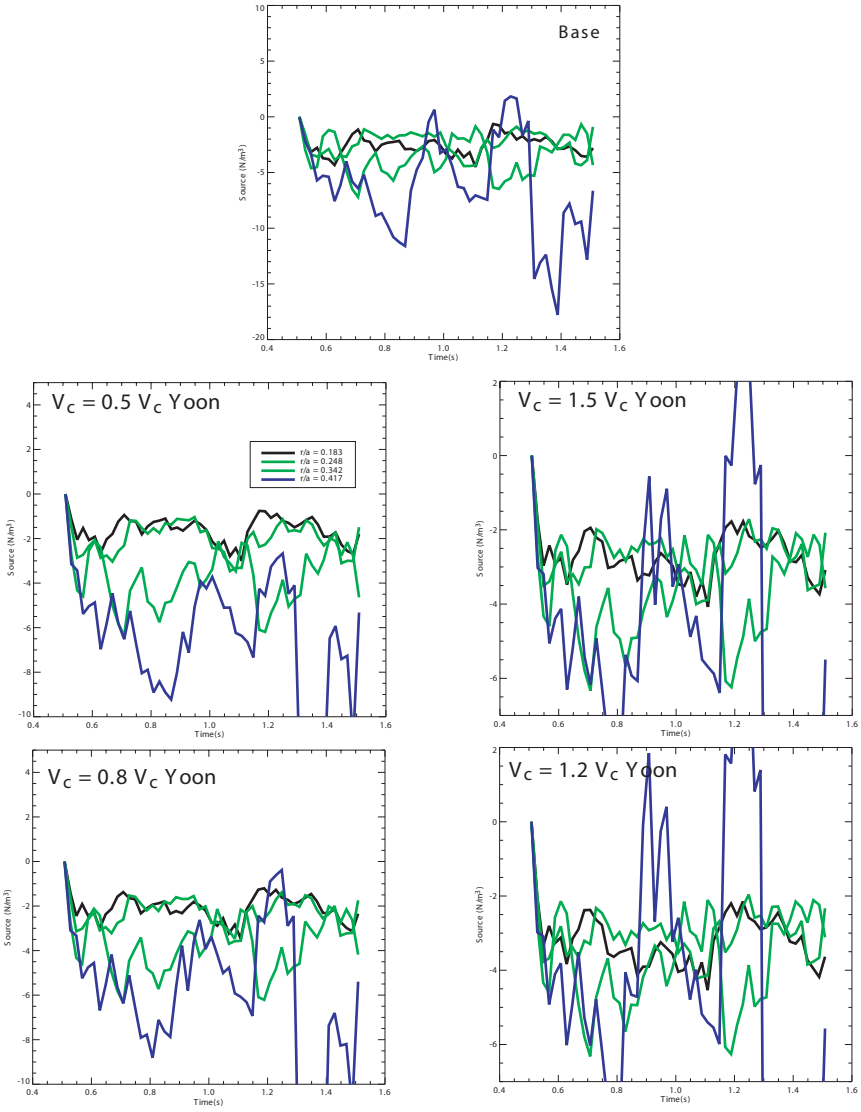

Figure E-4: Time traces of the rotation source at various radii with different scaling values of the Yoon convective term. TRANSP diffusion is used in this case.

Appendix F

Glossary

There are a wide variety of terms defined in this thesis. For simplicity, the majority of these terms will be listed here and shown in Table F.1. A complete set of definitions, formulas, and useful facts can be found in [10]. Some symbols have multiple definitions, but this is generally resolved by the context of the equations.

Table F.1: Commonly used terms for equations in this thesis.

Term	Description	Equation
a	Minor radius	
R	Major radius	
κ	Plasma Elongation	
L_n	Density gradient scale length	$-n/\nabla n$
L_T	Temperature gradient scale length	$-\mathrm{T}/\nabla\mathrm{T}$
L_s	Magnetic shear scale length	$R_0 q^2/r(\partial q/\partial r)$
η	Ratio of the temperature to density scale lengths	$d\ln T/d\ln n$
v_{T_i}	Ion thermal speed	$\sqrt{2T_i/m_i}$
c_s	Sound speed	$(\gamma Z T_e/m_i)^{1/2}$
v_A	Alfvén velocity	$(B^2/(4\pi n m))^{1/2}$
ρ_i	Larmor radius	$m_i v_T/Z_i e B$
ρ_*	Normalized Larmor radius	ρ_i/a
ρ_s	Sound Speed Normalized Larmor radius	$m_i c_s/Z_i e B a$
ϵ	Inverse aspect ratio	a/R
q	Safety factor	$\sim aB_t/(RB_p)$
Z_{eff}	Effective plasma charge	$\Sigma n_j Z_j^2/\Sigma n_j Z_j$
α	Effective impurity charge	$n_I Z_I^2/n_i Z_i$
χ_i	Ion thermal diffusivity	
χ_e	Electron thermal diffusivity	
χ_ϕ	Momentum diffusivity	
P_r	Prandtl number	χ_ϕ/χ_i
v_c	Momentum convection	
Π	Residual stress	
α	Momentum source and residual stress	$S-\nabla\cdot\Pi$
τ_i	Ion collision time	
τ_e	Electron collision time	
η	Plasma resistivity	
τ	Ratio of electron to ion temperature	T_e/T_i
Γ	Radial flux of momentum	

Bibliography

[1] M. Bitter, K. W. Hill, B. Stratton, A. L. Roquemore, D. Mastrovito, S. G. Lee, J. G. Bak, M. K. Moon, U. W. Nam, G. Smith, J. E. Rice, P. Beiersdorfer, and B. S. Fraenkel. Spatially resolved spectra from a new x-ray imaging crystal spectrometer for measurements of ion and electron temperature profiles (invited). *Review of Scientific Instruments*, 75(10):3660–3665, 2004.

[2] L.F. Delgado-Aparicio, M. Bitter, Y. Podpaly, J. Rice, W. Burke, M. Sanchez del Rio, K. Hill, N. Pablant, P. Beiersdorfer, R. Bell, R. Feder, C. Gao, D. Johnson, S.G. Lee, E. Marmar, M.L. Reinke, S. Scott, and R. Wilson. Effects of thermal expansion of crystal-lattice on x-ray imaging crystal spectrometer. *Review of Scientific Instruments*, Submitted, 2011.

[3] J.E. Rice, B.P. Duval, M.L. Reinke, Y.A. Podpaly, A. Bortolon, R.M. Churchill, I. Cziegler, P.H. Diamond, A. Dominguez, P.C. Ennever, C.L. Fiore, R.S. Granetz, M.J. Greenwald, A.E. Hubbard, J.W. Hughes, J.H. Irby, Y. Ma, E.S. Marmar, R.M. McDermott, M. Porkolab, N. Tsujii, and S.M. Wolfe. Observations of core toroidal rotation reversals in Alcator C-Mod ohmic L-mode plasmas. *Nuclear Fusion*, 51(8):083005, 2011.

[4] M. Yoshida, Y. Sakamoto, H. Takenaga, S. Ide, N. Oyama, T. Kobayashi, and Y. Kamada. Rotation Drive and Momentum Transport with Electron Cyclotron Heating in Tokamak Plasmas. *Phys. Rev. Lett.*, 103:065003, Aug 2009.

[5] J. E. Rice, E. S. Marmar, E. Källne, and J. Källne. Radial profiles of ground-state transitions of heliumlike argon from the Alcator-C tokamak. *Phys. Rev.*

A, 35:3033–3045, Apr 1987.

[6] E. S. Marmar, J. E. Rice, E. Källne, J. Källne, and R. E. LaVilla. Precision measurement of the $1s$ Lamb shift in hydrogenlike argon. *Phys. Rev. A*, 33:774–777, Jan 1986.

[7] J. Wesson. *Tokamaks*. Oxford University Press, 2004.

[8] A. Bondeson and D. J. Ward. Stabilization of external modes in tokamaks by resistive walls and plasma rotation. *Phys. Rev. Lett.*, 72:2709–2712, Apr 1994.

[9] M. Barnes, F. I. Parra, E. G. Highcock, A. A. Schekochihin, S. C. Cowley, and C. M. Roach. Turbulent Transport in Tokamak Plasmas with Rotational Shear. *Phys. Rev. Lett.*, 106:175004, Apr 2011.

[10] Z.S. Hartwig and Y.A. Podpaly. The magnetic fusion energy formulary. MIT, 2011.

[11] W.M. Solomon, K.H. Burrell, J.S. deGrassie, J.A. Boedo, A.M. Garofalo, R.A. Moyer, S.H. Muller, C.C. Petty, and H. Reimerdes. Characterization of intrinsic rotation drive on DIII-D. *Nuclear Fusion*, 51(7):073010, 2011.

[12] W.M. Solomon, K.H. Burrell, A.M. Garofalo, A.J. Cole, R.V. Budny, J.S. deGrassie, W.W. Heidbrink, G.L. Jackson, M.J. Lanctot, R. Nazikian, H. Reimerdes, E.J. Strait, M.A. Van Zeeland, and the DIII-D Rotation Physics Task Force. Advances in understanding the generation and evolution of the toroidal rotation profile on DIII-D. *Nuclear Fusion*, 49(8):085005, 2009.

[13] C.E. Kessel, G. Giruzzi, A.C.C. Sips, R.V. Budny, J.F. Artaud, V. Basiuk, F. Imbeaux, E. Joffrin, M. Schneider, M. Murakami, T. Luce, Holger St John, T. Oikawa, N. Hayashi, T. Takizuka, T. Ozeki, Y.-S. Na, J.M. Park, J. Garcia, and A.A. Tucillo. Simulation of the hybrid and steady state advanced operating modes in ITER. *Nuclear Fusion*, 47(9):1274, 2007.

[14] S.C. Jardin, C.E. Kessel, T.K. Mau, R.L. Miller, F. Najmabadi, V.S. Chan, M.S. Chu, R. LaHaye, L.L. Lao, T.W. Petrie, P. Politzer, H.E. St.John, P. Snyder, G.M. Staebler, A.D. Turnbull, and W.P. West. Physics basis for the advanced tokamak fusion power plant, ARIES-AT. *Fusion Engineering and Design*, 80(1-4):25 – 62, 2006. Aries - AT Special Issue.

[15] G.M. Olynyk, Z.S. Hartwig, D.G. Whyte, H.S. Barnard, P.T. Bonoli, L. Bromberg, M.L. Garrett, C.B. Haakonsen, R.T. Mumgaard, and Y.A. Podpaly. Vulcan: A steady-state tokamak for reactor-relevant plasma material interaction science. *Fusion Engineering and Design*, 87(3), 2012.

[16] R. J. Groebner, K. H. Burrell, and R. P. Seraydarian. Role of edge electric field and poloidal rotation in the *L-H* transition. *Phys. Rev. Lett.*, 64:3015–3018, Jun 1990.

[17] K. Ida, S. Hidekuma, Y. Miura, T. Fujita, M. Mori, K. Hoshino, N. Suzuki, T. Yamauchi, and JFT-2M Group. Edge electric-field profiles of *H*-mode plasmas in the JFT-2M tokamak. *Phys. Rev. Lett.*, 65:1364–1367, Sep 1990.

[18] G.R. McKee, P. Gohil, D.J. Schlossberg, J.A. Boedo, K.H. Burrell, J.S. deGrassie, R.J. Groebner, R.A. Moyer, C.C. Petty, T.L. Rhodes, L. Schmitz, M.W. Shafer, W.M. Solomon, M. Umansky, G. Wang, A.E. White, and X. Xu. Dependence of the L- to H-mode power threshold on toroidal rotation and the link to edge turbulence dynamics. *Nuclear Fusion*, 49(11):115016, 2009.

[19] J.E. Rice, A.E. Hubbard, J.W. Hughes, M.J. Greenwald, B. LaBombard, J.H. Irby, Y. Lin, E.S. Marmar, D. Mossessian, S.M. Wolfe, and S.J. Wukitch. The dependence of core rotation on magnetic configuration and the relation to the H-mode power threshold in Alcator C-Mod plasmas with no momentum input. *Nuclear Fusion*, 45(4):251, 2005.

[20] T. S. Hahm. Rotation shear induced fluctuation decorrelation in a toroidal plasma. *Physics of Plasmas*, 1(9):2940–2944, 1994.

[21] C. L. Fiore, P. T. Bonoli, D. R. Ernst, A. E. Hubbard, M. J. Greenwald, A. Lynn, E. S. Marmar, P. Phillips, M. H. Redi, J. E. Rice, S. M. Wolfe, S. J. Wukitch, and K. Zhurovich. Control of internal transport barriers on Alcator C-Mod. *Physics of Plasmas*, 11(5):2480–2487, 2004.

[22] C. L. Fiore, D. R. Ernst, Y. Podpaly, D. Mikkelsen, N. T. Howard, Jungpyo Lee, M.L. Reinke, J.E. Rice, J. W. Hughes, Y. Ma, W. L. Rowan, I. Bespamyatnov, and J. Candy. Production of internal transport barriers via self-generated mean flows in Alcator C-Mod. *Physics of Plasmas*, In Press, 2012.

[23] E. J. Strait, T. S. Taylor, A. D. Turnbull, J. R. Ferron, L. L. Lao, B. Rice, O. Sauter, S. J. Thompson, and D. Wróblewski. Wall Stabilization of High Beta Tokamak Discharges in DIII-D. *Phys. Rev. Lett.*, 74:2483–2486, Mar 1995.

[24] L.-J. Zheng, M. Kotschenreuther, and M. S. Chu. Rotational Stabilization of Resistive Wall Modes by the Shear Alfvén Resonance. *Phys. Rev. Lett.*, 95:255003, Dec 2005.

[25] F.I. Parra and P.J. Catto. Transport of momentum in full f gyrokinetics. *Physics of Plasmas*, 17:056106, 2010.

[26] S.P. Hirshman and D.J. Sigmar. Neoclassical transport of impurities in tokamak plasmas. *Nuclear Fusion*, 21(9):1079, 1981.

[27] Y. B. Kim, P. H. Diamond, and R. J. Groebner. Neoclassical poloidal and toroidal rotation in tokamaks. *Physics of Fluids B: Plasma Physics*, 3(8):2050–2060, 1991.

[28] W. A. Houlberg, K. C. Shaing, S. P. Hirshman, and M. C. Zarnstorff. Bootstrap current and neoclassical transport in tokamaks of arbitrary collisionality and aspect ratio. *Physics of Plasmas*, 4(9):3230–3242, 1997.

[29] W. M. Solomon, K. H. Burrell, R. Andre, L. R. Baylor, R. Budny, P. Gohil, R. J. Groebner, C. T. Holcomb, W. A. Houlberg, and M. R. Wade. Experimental test

of the neoclassical theory of impurity poloidal rotation in tokamaks. *Physics of Plasmas*, 13(5):056116, 2006.

[30] J. E. Rice, W. D. Lee, E. S. Marmar, N. P. Basse, P. T. Bonoli, M. J. Greenwald, A. E. Hubbard, J. W. Hughes, I. H. Hutchinson, A. Ince-Cushman, J. H. Irby, Y. Lin, D. Mossessian, J. A. Snipes, S. M. Wolfe, S. J. Wukitch, and K. Zhurovich. Toroidal rotation and momentum transport in Alcator C-Mod plasmas with no momentum input. *Physics of Plasmas*, 11(5):2427–2432, 2004.

[31] Andre L. Rogister. A unified theory of transport barriers and of subneoclassical transport. *Physics of Plasmas*, 6(1):200–213, 1999.

[32] A.L. Rogister, J.E. Rice, A. Nicolai, A. Ince-Cushman, S. Gangadhara, and Alcator C-Mod Group. Theoretical interpretation of the toroidal rotation velocity observed in Alcator C-Mod Ohmic H-mode discharges. *Nuclear Fusion*, 42(9):1144, 2002.

[33] K. C. Shaing. Theory for Toroidal Momentum Pinch and Flow Reversal in Tokamaks. *Phys. Rev. Lett.*, 86:640–643, Jan 2001.

[34] G. Penn and B. Coppi. *Bulletins of the American Physical Society*, 44:304, 1999.

[35] B. Coppi. Accretion theory of 'spontaneous' rotation in toroidal plasmas. *Nuclear Fusion*, 42(1), 2002.

[36] W. D. Lee, J. E. Rice, E. S. Marmar, M. J. Greenwald, I. H. Hutchinson, and J. A. Snipes. Observation of Anomalous Momentum Transport in Tokamak Plasmas with No Momentum Input. *Phys. Rev. Lett.*, 91:205003, Nov 2003.

[37] P.H. Diamond, C.J. McDevitt, Ö.D. Gürcan, T.S. Hahm, W. X. Wang, E.S. Yoon, I. Holod, Z. Lin, V. Naulin, and R. Singh. Physics of non-diffusive turbulent transport of momentum and the origins of spontaneous rotation in tokamaks. *Nuclear Fusion*, 49(4):045002, 2009.

[38] William Davis Lee. *Experimental Investigation of Toroidal Rotation Profiles in the Alcator C-Mod Tokamak*. PhD thesis, Massachusetts Institute of Technology, 2003.

[39] L.L. Lao, H. St. John, R.D. Stambaugh, A.G. Kellman, and W. Pfeiffer. Reconstruction of current profile parameters and plasma shapes in tokamaks. *Nuclear Fusion*, 25(11):1611, 1985.

[40] S. D. Scott, P. H. Diamond, R. J. Fonck, R. J. Goldston, R. B. Howell, K. P. Jaehnig, G. Schilling, E. J. Synakowski, M. C. Zarnstorff, C. E. Bush, E. Fredrickson, K. W. Hill, A. C. Janos, D. K. Mansfield, D. K. Owens, H. Park, G. Pautasso, A. T. Ramsey, J. Schivell, G. D. Tait, W. M. Tang, and G. Taylor. Local measurements of correlated momentum and heat transport in the tftr tokamak. *Phys. Rev. Lett.*, 64:531–534, Jan 1990.

[41] N. Mattor and P. H. Diamond. Momentum and thermal transport in neutral-beam-heated tokamaks. *Physics of Fluids*, 31(5):1180–1189, 1988.

[42] D. Strintzi, A. G. Peeters, and J. Weiland. The toroidal momentum diffusivity in a tokamak plasma: A comparison of fluid and kinetic calculations. *Physics of Plasmas*, 15(4):044502, 2008.

[43] I. H. Hutchinson. Heuristic Representations of Plasma Momentum Transport. *Arxiv*, 2009.

[44] A. G. Peeters, C. Angioni, Y. Camenen, F. J. Casson, W. A. Hornsby, A. P. Snodin, and D. Strintzi. The influence of the self-consistent mode structure on the Coriolis pinch effect. *Physics of Plasmas*, 16(6):062311, 2009.

[45] E.S. Yoon and T.S. Hahm. Transport of parallel momentum by toroidal ion temperature gradient instability near marginality. *Nuclear Fusion*, 50(6):064006, 2010.

[46] N. Kluy, C. Angioni, Y. Camenen, and A. G. Peeters. Linear gyrokinetic calculations of toroidal momentum transport in the presence of trapped electron modes in tokamak plasmas. *Physics of Plasmas*, 16(12):122302, 2009.

[47] Y. Kosuga, P. H. Diamond, and Ö. D. Gürcan. On the efficiency of intrinsic rotation generation in tokamaks. *Physics of Plasmas*, 17(10):102313, 2010.

[48] P. H. Diamond, C. J. McDevitt, O. D. Gurcan, T. S. Hahm, and V. Naulin. Transport of parallel momentum by collisionless drift wave turbulence. *Physics of Plasmas*, 15(1):012303, 2008.

[49] M. Yoshida, Y. Sakamoto, M. Honda, Y. Kamada, H. Takenaga, N. Oyama, H. Urano, and the JT-60 Team. Core and edge toroidal rotation study in JT-60U. *Nuclear Fusion*, 52(2):023024, 2012.

[50] M. Yoshida, Y. Kamada, H. Takenaga, Y. Sakamoto, N. Oyama, H. Urano, and the JT-60 Team. Characteristics of momentum transport in JT-60U H-mode plasmas. *Nuclear Fusion*, 49(11):115028, 2009.

[51] A. Ince-Cushman. *Rotation Studies in Fusion Plasmas via Imaging X-ray Crystal Spectroscopy*. PhD thesis, Massachusetts Institute of Technology, 2008.

[52] A. Ince-Cushman, J. E. Rice, M. Bitter, M. L. Reinke, K. W. Hill, M. F. Gu, E. Eikenberry, Ch. Broennimann, S. Scott, Y. Podpaly, S. G. Lee, and E. S. Marmar. Spatially resolved high resolution x-ray spectroscopy for magnetically confined fusion plasmas (invited). *Review of Scientific Instruments*, 79(10):10E302, 2008.

[53] M. Bitter, K. W. Hill, A. L. Roquemore, P. Beiersdorfer, S. M. Kahn, S. R. Elliott, and B. Fraenkel. Imaging x-ray crystal spectrometers for the National Spherical Torus Experiment. *Review of Scientific Instruments*, 70(1):292–295, 1999.

[54] N. Pablant, M. Bitter, L. Delgado-Aparicio, K. Hill, S. Lazerson, L. Roquemore, D. Gates, D. Monticello, H. Neilson, A. Reiman, M. Goto, S. Morita,

H. Yamada, M. Reinke, and J. Rice. First results from the high-resolution x-ray imaging crystal spectrometer on the Large Helical Device. http://meetings.aps.org/link/BAPS.2011.DPP.GP9.71, 2011.

[55] S. G. Lee, J. G. Bak, M. Bitter, K. Hill, U. W. Nam, Y. J. Kim, and M. K. Moon. Research and development of x-ray imaging crystal spectrometers for KSTAR. *Review of Scientific Instruments*, 75(10):3693–3695, 2004.

[56] A. H. Gabriel. Dielectronic Satellite Spectra for Highly Charged Helium-like Ion Lines. *Monthy Notices of the Royal Astrophysical Society*, 160:99–119, 1972.

[57] S. M. Wolfe, I. H. Hutchinson, R. S. Granetz, J. Rice, A. Hubbard, A. Lynn, P. Phillips, T. C. Hender, D. F. Howell, R. J. La Haye, and J. T. Scoville. Non-axisymmetric field effects on Alcator C-Mod. *Physics of Plasmas*, 12(5):056110, 2005.

[58] K. W. Hill, M. Bitter, L. Delgado-Aparicio, D. Johnson, R. Feder, P. Beiersdorfer, J. Dunn, K. Morris, E. Wang, M. Reinke, Y. Podpaly, J. E. Rice, R. Barnsley, M. O'Mullane, and S. G. Lee. Development of a spatially resolving x-ray crystal spectrometer for measurement of ion-temperature (T_i) and rotation-velocity (v) profiles in ITER. *Review of Scientific Instruments*, 81(10):10E322, 2010.

[59] Dectris Ltd. *USER Manual PILATUS Detector Systems*, 2008.

[60] A. Thompson, I. Lindau, D. Attwood, et al. X-Ray Data Booklet. Lawrence Berkeley National Laboratory, 2009.

[61] E Källne, J Källne, E S Marmar, and J E Rice. High Resolution X-Ray Spectroscopy Diagnostics of High Temperature Plasmas. *Physica Scripta*, 31(6):551, 1985.

[62] L. von Hamos. *Naturwissenschaften*, 20:705, 1932.

[63] William L. Rowan, Roger D. Bengtson, R. V. Bravenec, H. He, J. Jagger, D. M. Patterson, D. W. Ross, P. M. Valanju, A. J. Wootton, E. S. Marmar, J. H. Irby, J. A. Snipes, and J. L. Terry. Neutral beam diagnostics for Alcator C-Mod. *Rev. Sci. Instrum.*, 68(1):300–303, 1997.

[64] I. H. Hutchinson. *Principles of Plasma Diagnostics*. Cambridge University Press, 2002.

[65] R. M. McDermott, B. Lipschultz, J. W. Hughes, P. J. Catto, A. E. Hubbard, I. H. Hutchinson, R. S. Granetz, M. Greenwald, B. LaBombard, K. Marr, M. L. Reinke, J. E. Rice, D. Whyte, and Alcator C-Mod Team. Edge radial electric field structure and its connections to H-mode confinement in Alcator C-Mod plasmas. *Physics of Plasmas*, 16(5):056103, 2009.

[66] J. W. Hughes, D. Mossessian, K. Zhurovich, M. DeMaria, K. Jensen, and A. Hubbard. Thomson scattering upgrades on Alcator C-Mod. *Review of Scientific Instruments*, 74(3):1667–1670, 2003.

[67] R. L. Boivin, J. A. Goetz, E. S. Marmar, J. E. Rice, and J. L. Terry. High resolution bolometry on the Alcator C-Mod tokamak (invited). *Review of Scientific Instruments*, 70(1):260–264, 1999.

[68] R.J. Hawryluk. An Empirical Approach to Tokamak Transport. *Physics of Plasma Close to Thermonuclear Conditions*, 1:19–46, 1980.

[69] M.C. Zarnstoff, K. McGuire, and M.G. Bell. Parallel electric resistivity in the TFTR tokamak. *Physics of Fluids: B*, 2:1852, 1990.

[70] J. Ongena, M. Evrard, and D. McCune. Numerical Transport Codes. *Transaction of Fusion Technology*, 33(2T):181–191, 1998.

[71] R.V. Budny, M.G. Bell, H. Biglari, M. Bitter, C.E. Bush, C.Z. Cheng, E.D. Fredrickson, B. Grek, K.W. Hill, H. Hsuan, A.C. Janos, D.L. Jassby, D.W. Johnson, L.C. Johnson, B. LeBlanc, D.C. McCune, D.R. Mikkelsen, H.K. Park,

A.T. Ramsey, S.A. Sabbagh, S.D. Scott, J.F. Schivell, J.D. Strachan, B.C. Stratton, E.J. Synakowski, G. Taylor, M.C. Zarnstorff, and S.J. Zweben. Simulations of deuterium-tritium experiments in TFTR. *Nuclear Fusion*, 32(3):429, 1992.

[72] M. Kotschenreuther, G. Rewoldt, and W.M. Tang. Comparison of Initial Value and Eigenvalue Codes for Kinetic Toroidal Plasma Instabilities. *Computer Physics Communications*, 88:128, 1995.

[73] W. Dorland, F. Jenko, M. Kotschenreuther, and B.N. Rogers. Electron Temperature Gradient Turbulence. *Physics Review Letters*, 85:5579, 2000.

[74] J. Kinsey. The GYRO Nonlinear Gyrokinetic Simulation Database. http://fusion.gat.com/theory/gyro/, 2008.

[75] A Scarabosio, A Bortolon, B P Duval, A Karpushov, and A Pochelon. Toroidal plasma rotation in the TCV tokamak. *Plasma Physics and Controlled Fusion*, 48(5):663, 2006.

[76] A. Bortolon, B. P. Duval, A. Pochelon, and A. Scarabosio. Observation of Spontaneous Toroidal Rotation Inversion in Ohmically Heated Tokamak Plasmas. *Phys. Rev. Lett.*, 97(23):235003, Dec 2006.

[77] B P Duval, A Bortolon, A Karpushov, R A Pitts, A Pochelon, A Scarabosio, and the TCV Team. Bulk plasma rotation in the TCV tokamak in the absence of external momentum input. *Plasma Physics and Controlled Fusion*, 49(12B):B195, 2007.

[78] B. P. Duval, A. Bortolon, A. Karpushov, R. A. Pitts, A. Pochelon, O. Sauter, A. Scarabosio, G. Turri, and the TCV Team. Spontaneous L-mode plasma rotation scaling in the TCV tokamak. *Physics of Plasmas*, 15(5):056113, 2008.

[79] J. E. Rice, I. Cziegler, P. H. Diamond, B. P. Duval, Y. A. Podpaly, M. L. Reinke, P. C. Ennever, M. J. Greenwald, J. W. Hughes, Y. Ma, E. S. Marmar,

M. Porkolab, N. Tsujii, and S. M. Wolfe. Rotation Reversal Bifurcation and Energy Confinement Saturation in Tokamak Ohmic *l*-Mode Plasmas. *Phys. Rev. Lett.*, 107:265001, Dec 2011.

[80] ITER Physics Expert Group on Confinement Modelling Database ITER Physics Expert Group on Confinement, Transport and ITER Physics Basis Editors. Chapter2: Plasma confinement and transport. *Nuclear Fusion*, 39(12):2175, 1999.

[81] Nathaniel J. Fisch. Theory of current drive in plasmas. *Rev. Mod. Phys.*, 59:175–234, Jan 1987.

[82] V. L. Granatstein and P. L. Colestock, editors. *Wave Heating and Current Drive in Plasmas*. Gordon and Breach Science Publishers, 1985.

[83] J.P. Lee et al. Theoretical study on ion toroidal rotation induced by lower hybrid waves in Alcator C-Mod. PhD student seminar, 2010.

[84] A.E. Schmidt. *Measurements and Modeling of Lower Hybrid Driven Fast Electrons on Alcator C-Mod*. PhD thesis, Massachusetts Institute of Technology, 2010.

[85] A. Ince-Cushman, J. E. Rice, M. Reinke, M. Greenwald, G. Wallace, R. Parker, C. Fiore, J. W. Hughes, P. Bonoli, S. Shiraiwa, A. Hubbard, S. Wolfe, I. H. Hutchinson, E. Marmar, M. Bitter, J. Wilson, and K. Hill. Observation of Self-Generated Flows in Tokamak Plasmas with Lower-Hybrid-Driven Current. *Phys. Rev. Lett.*, 102(3):035002, Jan 2009.

[86] J.E. Rice, A.C. Ince-Cushman, P.T. Bonoli, M.J. Greenwald, J.W. Hughes, R.R. Parker, M.L. Reinke, G.M. Wallace, C.L. Fiore, R.S. Granetz, A.E. Hubbard, J.H. Irby, E.S. Marmar, S. Shiraiwa, S.M. Wolfe, S.J. Wukitch, M. Bitter, K. Hill, and J.R. Wilson. Observations of counter-current toroidal rotation in Alcator C-Mod LHCD plasmas. *Nuclear Fusion*, 49(2):025004, 2009.

[87] Y. Koide, T. Tuda, K. Ushigusa, N. Asakura, A. Sakasai, S. Ide, S. Ishida, M. Kikuchi, M. Azumi, A. Funahashi, and the JT-60 Team. Spontaneous Plasma Rotation of Near-Perpendicular Beam Injection and Lower Hybrid Current Drive Plasmas in JT-60U. *Proc. 14th Int. Conf. on Plasma Physics and Controlled Nuclear Fusion Research*, 1:777, 1993.

[88] P. Platz, V. Basiuk, B. Saoutic, R. Arslabenkov, and J. Carrasco. Toroidal velocity and ripple losses in Tore Supra with LH, ICRF, and combined additional heating. *22nd European Physical Society Conf. on Plasma Physics and Controlled Fusion*, 19C, 1995.

[89] L-G Eriksson, T Hellsten, M F F Nave, J Brzozowski, K Holmström, T Johnson, J Ongena, K-D Zastrow, and JET-EFDA Contributors. Toroidal rotation in RF heated JET plasmas. *Plasma Physics and Controlled Fusion*, 51(4):044008, 2009.

[90] Yuejiang Shi, Guosheng Xu, Fudi Wang, Mao Wang, Jia Fu, Yingying Li, Wei Zhang, Wei Zhang, Jiafeng Chang, Bo Lv, Jinping Qian, Jiafang Shan, Fukun Liu, Siye Ding, Baonian Wan, Sang-Gon Lee, Manfred Bitter, and Kenneth Hill. Observation of Cocurrent Toroidal Rotation in the EAST Tokamak with Lower-Hybrid Current Drive. *Phys. Rev. Lett.*, 106(23):235001, Jun 2011.

[91] J. Irby, D. Gwinn, W. Beck, B. LaBombard, R. Granetz, and R. Viera. ALCATOR C-MOD DESIGN, ENGINEERING AND DISRUPTION RESEARCH. *Fusion Science and Technology*, 51, April 2007.

[92] Yves Peysson, Robert Arslanbekov, Vincent Basiuk, Joel Carrasco, Xavier Litaudon, Didier Moreau, and Joao P. Bizarro. Magnetic ripple and the modeling of lower-hybrid current drive in tokamaks. *Physics of Plasmas*, 3(10):3668–3688, 1996.

[93] Y. Camenen, Y. Idomura, S. Jolliet, and A.G. Peeters. Consequences of profile shearing on toroidal momentum transport. *Nuclear Fusion*, 51(7):073039, 2011.

[94] A.P. Smirnov, R.W. Harvey, and K. Kupfer. A general ray tracing code GENRAY. *Bull Amer. Phys. Soc.*, 39(7):1626, 1994.

[95] S. Shiraiwa, R. Mumgaard, and S. Scott. personal communication, 2012.

[96] J. S. deGrassie, K. H. Burrell, L. R. Baylor, W. Houlberg, and J. Lohr. Toroidal rotation in DIII-D in electron cyclotron heating and Ohmic H-mode discharges. *Physics of Plasmas*, 11(9):4323–4331, 2004.

[97] B. LaBombard, J.E. Rice, A.E. Hubbard, J.W. Hughes, M. Greenwald, J. Irby, Y. Lin, B. Lipschultz, E.S. Marmar, C.S. Pitcher, N. Smick, S.M. Wolfe, S.J. Wukitch, and the Alcator Group. Transport-driven Scrape-Off-Layer flows and the boundary conditions imposed at the magnetic separatrix in a tokamak plasma. *Nuclear Fusion*, 44(10):1047, 2004.

[98] J E Rice, A C Ince-Cushman, M L Reinke, Y Podpaly, M J Greenwald, B LaBombard, and E S Marmar. Spontaneous core toroidal rotation in Alcator C-Mod L-mode, H-mode and ITB plasmas. *Plasma Physics and Controlled Fusion*, 50(12):124042, 2008.

[99] J.E. Rice, P.T. Bonoli, C.L. Fiore, W.D. Lee, E.S. Marmar, S.J. Wukitch, R.S. Granetz, A.E. Hubbard, J.W. Hughes, J.H. Irby, Y. Lin, D. Mossessian, S.M. Wolfe, K. Zhurovich, M.J. Greenwald, I.H. Hutchinson, M. Porkolab, and J.A. Snipes. Pressure profile modification of internal transport barrier plasmas in Alcator C-Mod. *Nuclear Fusion*, 43(8):781, 2003.

[100] C.L. Fiore, J.E. Rice, Y. Podpaly, I.O. Bespamyatnov, W.L. Rowan, J.W. Hughes, and M. Reinke. Rotation and transport in Alcator C-mod ITB plasmas. *Nuclear Fusion*, 50(6):064008, 2010.

[101] D.G. Whyte, A.E. Hubbard, J.W. Hughes, B. Lipschultz, J.E. Rice, E.S. Marmar, M. Greenwald, I. Cziegler, A. Dominguez, T. Golfinopoulos, N. Howard, L. Lin, R.M. McDermott, M. Porkolab, M.L. Reinke, J. Terry, N. Tsujii, S. Wolfe, S. Wukitch, Y. Lin, and the Alcator C-Mod Team. I-mode: an

H-mode energy confinement regime with L-mode particle transport in Alcator C-Mod. *Nuclear Fusion*, 50(10):105005, 2010.

[102] J. E. Rice, J. W. Hughes, P. H. Diamond, Y. Kosuga, Y. A. Podpaly, M. L. Reinke, M. J. Greenwald, Ö. D. Gürcan, T. S. Hahm, A. E. Hubbard, E. S. Marmar, C. J. McDevitt, and D. G. Whyte. Edge temperature gradient as intrinsic rotation drive in alcator *c*-mod tokamak plasmas. *Phys. Rev. Lett.*, 106(21):215001, May 2011.

[103] B. A. Grierson, K. H. Burrell, W. M. Solomon, and N. A. Pablant. Deuterium velocity and temperature measurements on the DIII-D tokamak. *Review of Scientific Instruments*, 81(10):10D735, 2010.

[104] Z. S. Hartwig and D. G. Whyte. Simulated plasma facing component measurements for an in situ surface diagnostic on Alcator C-Mod. *Review of Scientific Instruments*, 81(10):10E106, 2010.

[105] Alcator C-Mod Team. Special Issue on Alcator C-Mod. *Fus. Sci. Tech.*, 51(3), 2007.

[106] J. P. Lee, J. C. Wright, P. T. Bonoli, R. R. Parker, P. J. Catto, Y. A. Podpaly, J. E. Rice, and M. L. Reinke. Estimation of the ion toroidal rotation source due to momentum transfer from Lower Hybrid waves in Alcator C-Mod. *Power in Plasmas*, Proceedings of the 19th Topical Conf. on RF, 2011.

[107] J. Decker, Y. Peysson, J. Hillairet, J.-F. Artaud, V. Basiuk, A. Becoulet, A. Ekedahl, M. Goniche, G.T. Hoang, F. Imbeaux, A.K. Ram, and M. Schneider. Calculations of lower hybrid current drive in ITER. *Nuclear Fusion*, 51(7):073025, 2011.

[108] F. Jenko, W. Dorland, and G. W. Hammett. Critical gradient formula for toroidal electron temperature gradient modes. *Physics of Plasmas*, 8(9):4096–4104, 2001.

[109] W. Horton, G. T. Hoang, C. Bourdelle, X. Garbet, M. Ottaviani, and L. Colas. Electron transport and the critical temperature gradient. *Physics of Plasmas*, 11(5):2600–2606, 2004.

[110] W. M. Stacey and J. Mandrekas. Comparision of neoclassical rotation theory with experiment under a variety of conditions in DIII-D. *Physics of Plasmas*, 9(5):1622–1628, 2002.

[111] D. Ernst. Anatomy of toroidal drift modes. GS2 Workshop, PPPL, 2003.

[112] Bruno Coppi and Gregory Rewoldt. New Trapped-Electron Instability. *Phys. Rev. Lett.*, 33:1329–1332, Nov 1974.

[113] B. Coppi and F. Pegoraro. Theory of the ubiquitous mode. *Nuclear Fusion*, 17(5):969, 1977.

[114] W. M. Tang, G. Rewoldt, and Liu Chen. Microinstabilities in weak density gradient tokamak systems. *Physics of Fluids*, 29(11):3715–3718, 1986.

[115] M. Shimada, D.J. Campbell, V. Mukhovatov, M. Fujiwara, N. Kirneva, K. Lackner, M. Nagami, V.D. Pustovitov, N. Uckan, J. Wesley, N. Asakura, A.E. Costley, A.J.H. Donn, E.J. Doyle, A. Fasoli, C. Gormezano, Y. Gribov, O. Gruber, T.C. Hender, W. Houlberg, S. Ide, Y. Kamada, A. Leonard, B. Lipschultz, A. Loarte, K. Miyamoto, V. Mukhovatov, T.H. Osborne, A. Polevoi, and A.C.C. Sips. Chapter 1: Overview and summary. *Nuclear Fusion*, 47(6):S1, 2007.